

PREDICTING SHEAR TRANSMISSION ACROSS GRAIN BOUNDARY IN ALPHA  
TITANIUM

By

Yang Su

A DISSERTATION

Submitted to  
Michigan State University  
in partial fulfillment of the requirements  
for the degree of

Materials Science and Engineering – Doctor of Philosophy

2021

## **ABSTRACT**

### **PREDICTING SHEAR TRANSMISSION ACROSS GRAIN BOUNDARY IN ALPHA TITANIUM**

By

Yang Su

The capability to evaluate and model how metal deforms has benefited the manufacture and processing of the metals industry for decades. A predictive model that can be used to assess the evolution of stress/strain in a polycrystalline metals is desired as it will enable more accurate predictions of stress concentrations, damage nucleation, and material life spans. One of the major challenges in the development of such a model is understanding how plastic deformation flows through grain boundaries (such phenomenon is called slip transfer) and how the stress and strain fields are altered by slip transfer in the vicinity of the boundary. We attempted to overcome this challenge. In the current study carefully designed experiments and calibrated simulations are used to address this challenge.

A novel approach is used to study the interaction between slip and grain boundaries using bi-crystal nanoindentation. By placing nanoindents at varying distances from grain boundaries and measuring the resulting indent surface topographies using atomic force microscopy (AFM), the influence of grain boundaries on the development of indent surface topographies is assessed and related to a variety of slip transfer metrics. To further analyze the stress, strain, and shear of individual slip system in the bi-crystal nanoindentation, a crystal plasticity finite element (CPFE) models was built to simulate indentation near a grain boundary. The model was calibrated using experimentally measured parameters and successfully captured most of the features in the experiments. Nonetheless, strict point-to-point comparisons between experimentally measured

and simulated indent topographies revealed some discrepancies, in that the model is less accurate in the vicinity of grain boundaries than in the grain interiors.

To evaluate slip transfer and the local stress evolution in a fully quantitative manner, a predictive model was developed that is capable of resolving slip accommodation of multiple systems involved in the process. Slip trace analysis was combined with AFM and electron backscattered diffraction (EBSD) to analyze the slip accommodation observed at multiple grain boundaries. Based on all the experimentally observed slip transfer cases, a new iterative stress relief (ISR) model was developed. The ISR model, validated by experimental observations, features the ability to predicting multiple accommodating slip systems in a slip transfer and assessing the evolution of local stress state. In addition, a set of critical resolved shear stress (CRSS) ratios were obtained by minimizing the discrepancies between observations and model predictions.

This work has furthered the understanding of slip transfer/accommodations and the influence of local stress evolution on the slip transfer in the community. The ISR model has been proved to be very successful in the studied material system, but has yet to be tested under different conditions.

Copyright by  
YANG SU  
2021

## ACKNOWLEDGEMENTS

This work was carried out at the department of chemical engineering and material science at Michigan State University in East Lansing. I would like to thank my advisor Dr. Martin Crimp for his continuous support both in academia and personal life during my whole Ph.D. career. All those invaluable discussions with him and a high amount of scientific freedom have made this dissertation possible. I would like to thank Dr. Philip Eisenlohr for those countless inspiring discussions and his consistent mentoring of how to be a consistent and organized researcher. Dr. Thomas Bieler is acknowledged for sharing his many original ideas both in the experimental design and simulation methods. I would also like to thank the two other professors in my committees. Dr. Richard Lunt for his tutoring in the X-ray diffraction class and some suggestions on my nanoindentation experiments during that time. Dr. Ronald Averill is thanked for bringing the commercial software Marc Mentat, which is frequently used in the dissertation, to the engineering school. Dr. Askeland is acknowledged for his assistance with the use of SEM and FIB. Dr. Drown is thanked for fixing the nanoindenter. Dr. Baokang Bi is acknowledged for his assistance with the AFM work. To my present and former graduate colleagues in the metal's group, many thanks for creating a friendly and stimulating environment.

I am indebted to many colleagues in Max-Planck-Institut für Eisenforschung GmbH. Dr. Zambaldi is thanked for his help on the modeling of nanoindentation and many insightful ideas. Dr. Mercier is thanked for teaching me how to use Stabix to build a finite element indentation model. Dr. Raabe is thanked for hosting us at the MPIE and providing all the resources to complete our plans. I am also thankful to technicians at MPIE that provided useful suggestions on polishing titanium and helped me with many instruments.

Last but not least, I owe my deepest gratitude to my parents for always believing in me. Their support helped me get through many frustrations and setbacks through the Ph.D. and made this dissertation possible.

# TABLE OF CONTENTS

<b>LIST OF TABLES .....</b>	<b>x</b>
<b>LIST OF FIGURES .....</b>	<b>xi</b>
<b>KEY TO SYMBOLS AND ABBREVIATIONS .....</b>	<b>xvii</b>
<b>CHAPTER 1 INTRODUCTION AND LITERATURE REVIEW .....</b>	<b>1</b>
<b>1.1 Understanding heterogeneous plastic deformation near grain boundaries .....</b>	<b>1</b>
<b>1.2 Study of heterogeneous deformation at grain boundaries using slip transfer criteria. 2</b>	<b>2</b>
1.2.1 Slip transfer criterion involving only one outgoing slip system .....	2
1.2.2 Multiple outgoing slip system accommodation predicted using tangential continuity theory .....	7
<b>1.3 State of the art experimental techniques and simulation methodology used in slip transfer study .....</b>	<b>8</b>
1.3.1 Bi-crystal/quasi bi-crystal nanoindentation .....	9
1.3.2 Quantitative slip trace analysis .....	20
1.3.3 Other experimental technique .....	35
1.3.4 Coupling experimental results with CPFEM simulations .....	39
<b>1.4 Motivations of this study .....</b>	<b>44</b>
<b>1.5 Overview of this thesis .....</b>	<b>46</b>
<b>CHAPTER 2 MATERIALS, EXPERIMENTAL DETAILS, AND THE CONSTITUTIVE LAW OF CPFEM .....</b>	<b>49</b>
<b>2.1 Description of material .....</b>	<b>49</b>
2.1.1 Material A .....	49
2.1.2 Material B .....	49
<b>2.2 Sample preparation .....</b>	<b>52</b>
2.2.1 Sample A .....	52
2.2.2 Sample B .....	52
<b>2.3 Experimental details .....</b>	<b>52</b>
2.3.1 Scanning electron microscopy .....	52
2.3.2 Focused Ion Beam (FIB) cross sectioning .....	55
2.3.3 Atomic Force microscopy (AFM) .....	57
2.3.4 Nanoindentation .....	57
2.3.5 Four-point bending .....	60
<b>2.4 Slip trace analysis .....</b>	<b>62</b>
<b>2.5 Constitutive law in Crystal Plasticity Finite Element Method (CPFEM) .....</b>	<b>64</b>
<b>CHAPTER 3 STUDY OF SLIP TRANSFER USING NANOINDENTATION AND CRYSTAL PLASTICITY MODELING .....</b>	<b>66</b>
<b>3.1 Overview of the locations of nanoindentations .....</b>	<b>67</b>

<b>3.2 Nanoindentation load-displacement curves.....</b>	<b>69</b>
<b>3.3 Differences of the topographies formed in single and bi-crystal nanoindentations....</b>	<b>71</b>
3.3.1 Quantifying the volume difference of two indent topographies .....	71
3.3.2 Reproducibility of nanoindentation topographies.....	72
3.3.3 Comparing single crystal indent topographies with the corresponding bi-crystal indent topographies .....	75
<b>3.4 Simulations of single and bi-crystal nanoindentations using CPFEM.....</b>	<b>83</b>
3.4.1 Computer-assisted processing of experimental data and automatic conversion into simulation files.....	83
3.4.2. Formulation of a constitutive model for $\alpha$ -Ti .....	86
3.4.3. Three dimensional finite element simulation of indentation process .....	87
<b>3.5. Comparing of experimental and simulated indent topographies .....</b>	<b>89</b>
3.5.1 Single crystal indent topography comparison between experiment and simulation. ...	89
3.5.2 Bi-crystal indent topography comparison between experiment and simulation. ....	91
<b>3.6. Discussion.....</b>	<b>94</b>
3.6.1 Quantifying the quality of single crystal and bi-crystal simulation using $\Delta V_{sim}$ . exp .....	94
3.6.2 Correlating experiment and simulation results with slip transfer criterion $m'$ and $M$ (LRB criterion).....	96
3.6.3 Grain boundary sensitive CPFE model for bi-crystal nanoindentation .....	101
<b>3.7 Conclusions.....</b>	<b>108</b>
<b>CHAPTER 4 PREDICTING SLIP TRANSFER ACROSS GRAIN BOUNDARIES WITH AN ITERATIVE STRESS RELIEF MODEL .....</b>	<b>110</b>
<b>4.1 Observations of slip accommodation in <math>\alpha</math>-Ti.....</b>	<b>111</b>
<b>4.2 Determining the active slip systems, relative shears, and slip geometries of experimentally observed slip accommodations .....</b>	<b>113</b>
<b>4.3 Assessment of the tangential continuity theory based on slip transfer observations</b>	<b>117</b>
4.3.1 Tangential continuity theory .....	117
4.3.2 Predicting accommodating slip systems using tangential continuity theory .....	118
<b>4.4. A new iterative stress relief (ISR) model based on slip accommodation observations .....</b>	<b>128</b>
4.4.1 Algorithm of the iterative stress relief model .....	128
4.4.2 Predicting accommodating deformation systems using the iterative stress relief model .....	131
<b>4.5 Discussion.....</b>	<b>134</b>
4.5.1 Optimizing the variables in the iterative stress relief model.....	134
4.5.2 Limitations of the iterative stress relief model .....	139
4.5.3 Application of the ISR model to other materials and loading conditions .....	142
<b>4.6 Conclusions.....</b>	<b>143</b>
<b>CHAPTER 5 CONCLUSIONS.....</b>	<b>145</b>
<b>CHAPTER 6 OUTLOOK .....</b>	<b>148</b>

<b>APPENDICES.....</b>	<b>150</b>
<b>APPENDIX A: AFM DATA OF INDENT TOPOGRAPHIES IN 3D.....</b>	<b>151</b>
<b>APPENDIX B: SEM AND AFM MEASUREMENTS OF ALL SLIP     ACCOMMODATION CASES .....</b>	<b>152</b>
<b>BIBLIOGRAPHY.....</b>	<b>159</b>

## LIST OF TABLES

Table 1.1: Column 2-6: Slip geometry of all grain boundaries including disorientations (column 5) measured using the patterns in fig. 3 and $m'$ (column 4) which is the multiplication of column 2 and 3. Column 7 is the deformation behavior at grain boundaries where the type B, I, and T suggests slip band blocking, intermediate slip transmission, and slip transmission, respectively. [23] .....	13
Table 3.1: Material parameters used for simulating the $\alpha$ -Ti.[133] .....	86
Table 4.1: Slip systems types and geometrics, and number of dislocations in the slip bands for all 22 (16 single plus 6 double) slip accommodation observations. ....	116
Table 4.2: Indices, shear direction $d$ , and plane normal $n$ of deformation systems considered for shear accommodation in the study. ....	119
Table 4.3: The center point of the search range used in the parameter optimization of the iterative stress relief model. The six parameters correspond to the six dimensions of the optimization. ....	135

## LIST OF FIGURES

Figure 1.1: Slip transfer geometry at a grain boundary. ....	6
Figure 1.2: Nanohardness as a function of the distance between each indentation and the grain boundary. Each data point represents one indentation measurement. [22] .....	10
Figure 1.3: SEM images of nanoindentations at three types of grain boundaries and the corresponding EBSD patterns in the indented and neighboring grain. (a): Slip band caused by nanoindentations were blocked by the grain boundary (noted as type B). (b): Intermediate slip band development in the neighboring grain (noted as type I). (c): Full slip transmission across the grain boundary (noted as type T). [23] .....	12
Figure 1.4: Load-displacement curves of nanoindentations near two grain boundaries showing displacement jumps at different indentation depths and loads. [24] .....	15
Figure 1.5: Fe-14%Si boundary yielding events shown in a Hall-Petch type plot with the horizontal axis being the inverse square root of the distance between indent and boundary and vertical axis being the applied shear stress. [25].....	17
Figure 1.6: (a) Crystallographic details of the two grain boundaries including location of the indents and the orientation of the four indented grains. (b) The yielding stress calculated for each nanoindentations. [27] .....	19
Figure 1.7: An optical image of the primary {011} slip bands and secondary {101} slip bands in the grain boundary vicinity in a compressed bi-crystal sample. [34] .....	22
Figure 1.8: (a) A $m'$ vs grain boundary misorientation plot showing every of slip transfer and slip blockage events as a data point, where dots and crosses means slip transfer and slip blockage, respectively. (b) $m'$ times Schmid factor vs grain boundary misorientation plot showing the same data set. [37] .....	24
Figure 1.9. Crystal orientation map of the two aluminum samples with dramatic different microstructures, where the left being near-cube and right being rotated cube microstructure. [38] .....	26
Figure 1.10: A $\left(\frac{m'}{\Delta b}\right)$ vs grain boundary misorientation plot showing every of slip transfer and slip blockage events as a data point, where blue and brown means slip transfer and slip blockage, respectively. [38] .....	27
Figure 1.11: Plot of new slip transfer metric $M_b$ as a function of Schmid factor. The three zones (1,2,3) indicate the direct slip transfer, slip band blockage with stress concentration, and blockage without stress concentration, respectively. [39] .....	30

Figure 1.12: Schematic showing how the quantities in equation Eq. 1.9 are correlated with an AFM measurement. [44] .....	32
Figure 1.13: A Backscattered image showing the impinging twin initiated micro-cracks at a grain boundary. [45] .....	34
Figure 1.14: a) The four TEM images acquired at different tilt angles (marked at the top left corner) that were used to construct the tomograph shown in (b). b) The 3-D tomograph revealing the relative locations of each dislocations observed in the TEM image series in (a). [51] .....	37
Figure 1.15: a-c): CPFEM modeling of the Von Mises stress (a) and shear distribution (b,c) in the area of interest. d): Evolution of the simulated shear on two slip systems as a function of time. [49] .....	41
Figure 1.16: Left image: Quasi-3D CPFE model shows the columnar microstructure of all the grains. Right image: 3D model with grain structure information obtained from DAXM. [120] .....	43
Figure 2.1: An EBSD inverse pole figure (IPF) map of the area of interest in material A is presented. The texture of the material A shows a moderately strong texture with the c-axes lying predominantly in the plane of the image [40]. The array of black dots in the IPF map is a grid of nanoindentations to mark the area of interest. ....	50
Figure 2.2: An EBSD inverse pole figure map of a random area in material B is presented. The texture of the material B is almost random. ....	51
Figure 2.3: A schematic showing the setup of EBSD inside of an SEM (left image) and a typical diffraction pattern (Kikuchi pattern in right image) acquired in the EBSD scan that can be used for determining the crystalline orientation of the diffracted region. (Revised based on the image on <a href="https://www.mpie.de/3077954/EBSD">https://www.mpie.de/3077954/EBSD</a> ) .....	54
Figure 2.4: Backscattered electron image showing a FIB cross-section cut used to determine the grain boundary inclination below the surface, where $\theta$ is inclination angle measured from image and is used for the calculation of real grain boundary inclination using Eq. 2.1. ....	56
Figure 2.5: An SEM image of the region that contains the grid of nanoindentations (shown as black dots) in material A. ....	58
Figure 2.6: An SEM image of bi-crystal nanoindentations near a selected grain boundary with varying distances from the boundary in material A. The investigated grain boundary is colored in red dash line. ....	59
Figure 2.7: The picture of the four point stage with the sample. ....	61

Figure 2.8: The AFM measured surface profile of a slip trace (blue suggests lower height) overlaid with a unit cell of the corresponding grain orientation shown in top view (a) and side view (b, c). The assumed active slip plane in the slip trace analysis is colored in grey in the unit cell. .... 63

Figure 3.1: SEM images of bi-crystal nanoindents near the six selected grain boundaries and the corresponding single crystal indents in the two adjacent grains. .... 68

Figure 3.2: Load-displacement curve of a bi-crystal indent (shown as the grey dotted line) and the corresponding single crystal indent in the originating grain (shown as the black solid line). A magnified inset is used to show the displacement jump occurred in the bi-crystal indentation. .... 70

Figure 3.3: a,b): Example of two single crystal nanoindents from the same grain used for establishing the reproducibility and surface roughness of nominally identical nanoindentations, where  $r_{in}$  and  $r_{out}$  are the inner and outer radius of a ring centered on the indent and isolating the major indent topography features. c): Correlation between  $\Delta V$  (short for  $\Delta V_{SX,SX}^{ring}$  or  $\Delta V_{BX,BX}^{ring}$ , calculated based on Eq. 3.1) and ring area  $A$ . d): Cumulative probability of the surface roughness levels (dotted), established from the slope of the dotted line in (c), and reproducibility (solid) of single and bi-crystal indentation, as determined by the difference between slopes of the solid and dotted lines in (c). A reproducibility better than 3 nm corresponds to negligibly small perceived differences, as demonstrated by shifting one part of the color bar by that amount (e). [126] ..... 74

Figure 3.4: Nanoindent topographies developed when the indents impression falls across grain boundaries (center column), in comparison to corresponding single crystal indent topographies from both sides of the grain boundaries (second and fourth columns). The differences between the single and bi-crystal indents are mapped for the left grain and the right grain (first and last column) ..... 76

Figure 3.5: Nine bi-crystal indents (center column) collected near six different grain boundaries (blue lines) compared with corresponding single crystal indents in both the originating grains (second column) and receiving grains (fourth column). Both single and bi-crystal indentation impression depths ( $h$ ) are labeled near the indents, and the  $m'$  of the six grain boundaries are listed in the image of bi-crystal indent in decreasing order. Indent topography differences caused by the grain boundary are mapped in the outermost columns as the difference between grain boundary indent and single crystal indent. The central indent valleys have been removed in order to enhance visualization of the indent pile-ups around the valleys. [126] ..... 81

Figure 3.6: The GUI of stabix used for generating simulation input files by using grain orientation data from EBSD. Left image: EBSD crystallographic orientation data was first processed using the left GUI to determine the maximum  $m'$  parameter and to color the associated grain boundary. The hexagonal cells represent the orientations of each of the grains. Although the simulations include basal  $\langle a \rangle$ , prismatic  $\langle a \rangle$ ,

and pyramidal  $\langle c + a \rangle$ , the GUI only includes basal  $\langle a \rangle$  and prismatic  $\langle a \rangle$  for  $m'$  calculation. Middle image: The second GUI was used to display the crystallographic and slip system relationships. In the upper part of the figure, grain boundary information, such as Euler angles, the orientation of the grain boundary line, the inclination of the grain boundary plane, and the active slip systems, can be entered to study the slip transfer of a desired grain boundary. Specific  $m'$  (or  $M$ ) associated with each pair of slip systems are tabulated in lower part of the figure. Right image: Using the grain boundary information entered in the second GUI, the third GUI builds finite element meshes for bi-crystal indentation simulations. Sample dimensions, mesh resolution, indentation depth, and indenter tip geometry are required as input. [126] ..... 84

Figure 3.7: The finite element model used for a bi-crystal indentation tests where the black dotted line indicates the location of the grain boundary. The red color region indicates that the formation of surface topographies after the nanoindentation. [126] ..... 88

Figure 3.8: Experimentally measured (first column) and simulated (second column) topographies of two single crystal indent and the corresponding point-wise differences between experiment and simulation shown in the third column. [126] ..... 90

Figure 3.9: Comparisons between experimentally measured and simulated indent topographies near six grain boundaries. a) Indents that are located near the grain boundary. b) Indents that are right on the grain boundary. [126] ..... 93

Figure 3.10: Cumulative probability distributions of the differences between simulated and experimentally measured indent topographies for single crystal and bi-crystal case are shown as dotted blue line and solid blue line, respectively. As a comparison, noise level in experimental measurements from Fig. 3.3 are plotted for single crystal (dotted red line) and bi-crystal case (solid red line). [126] ..... 95

Figure 3.11: a): Schematic single and bi-crystal indents with gray areas representing  $V_{SX}^{receiving}$  (top) and  $V_{BX}^{receiving}$  (bottom). The grain boundary in the bi-crystal case is marked by a vertical solid line and continued as an imaginary 'grain boundary' for the single crystal case. b):  $m'$  vs. volume ratio (markers for experiment  $\times$  and simulation  $\circ$ ) between bi-crystal and originating single crystal indents evaluated within the originating grain (red) and the receiving grain (black). c):  $m'$  vs. normalized volume difference (markers for experiment  $\times$  and simulation  $\circ$ ) between bi-crystal and originating single crystal indents evaluated within the originating grain (red) and the receiving grain (black). d): Volume ratio between simulated and measured bi-crystal indents evaluated within the originating grain (red circles) and the receiving grain (black circles). e):  $M$  vs. normalized volume difference (both sim and exp) between bi-crystal and originating single crystal indents evaluated within the originating grain (red) and the receiving grain (black). [126] ..... 98

Figure 3.12: The grain boundary sensitive model proposed as a revision to the original model by inserting two layers of elements (Grain 1 boundary layer and grain 2 boundary layer) between the two adjacent grain 1 and 2. .... 103

Figure 3.13: The physical meaning of the four slip parameters in the model is shown in a stress-strain curve in the left figure. The values of the  $\tau_0$  and  $\tau_{\text{sat}}$  used in the original model are presented in the right graph. .... 104

Figure 3.14: Figure (a-c) show how the accuracy of the new model ( $V_{\text{sim}}^{\text{receiving}}/V_{\text{exp}}^{\text{receiving}}$ ) alters as a function of the change in each slip parameters ( $h_0$ ,  $a$ , and  $\tau_{\text{sat}(0)}$ ). The red dotted line indicates the optimal value of  $\tau_{\text{sat}(0)}$  (in the ratio form of  $\tau_{\text{sat}(0)}^{\text{revised}}/\tau_{\text{sat}(0)}^{\text{original}}$ ) that generates the most accurate simulation compared to experiment. Figure d presents all the optimal values of  $\tau_{\text{sat}(0)}$  acquired at four grain boundaries as a function of the four  $m'$ . .... 107

Figure 4.1: Secondary electron images of the three categories of slip accommodation: non-correlated (left), one-to-one correlated slip (center), one-to-two correlated slip (right), and corresponding topography maps measured by AFM (second row). .... 112

Figure 4.2: An example/key of a polar bar plot that presents all of the details of a shear transfer event and serves as key for Fig. 4.3, Fig. 4.4 and Fig. 4.5. A total of 30 (=3+3+6+12+6) potential deformation systems, color coded by type, are represented on the outside of the figure, with the numbers indicating the specific deformation system, as listed in Table 4.2. Each bar represents an incoming or outgoing slip system, with white indicating the incoming system, black indicating outgoing systems, and red denoting accommodating systems in the incoming grain. The direction each bar points to reflects its slip system type and the length of each bar represents its relative shear. .... 122

Figure 4.3: Radar bar plots showing tangential continuity predictions compared to observations of single shear accommodation cases. The left column indicates that the predictions are identical (and never match the observations) when at least two self-accommodating systems are allowed. The center two columns show the response changing for less than two self-accommodating systems. “0+5” predictions are most accurate, with about half agreeing with observations. .... 125

Figure 4.4: Similar plot as Fig. 4.3 but for double shear accommodation cases. Tangential continuity model predictions are shown in columns 2-4 and observations are presented in column 5. Across all six cases, none of the three distinct self-accommodation conditions result in predictions that agree with the observed accommodating shear systems. .... 127

Figure 4.5: The new (ISR) model predictions compared to observations for 16 single and 6 double accommodation cases. .... 133

Figure 4.6: Figure 4.6: Heat map showing the variation in the accuracy of the iterative stress relief model as a function of both $\alpha$ and $\beta$ . The accuracy of the model, shown in grey scale, is quantified using the fraction of correct predictions compared to observations. Lighter gray suggests higher accuracy of the model. ....	135
Figure 4.7: Heat map showing the accuracy variation of the iterative stress relief model as a function of CRSS ratios prism $\langle a \rangle$ and pyramidal $\langle a \rangle$ . The accuracy of the model is quantified using the fraction of correct predictions compared to observations. Lighter gray suggests higher accuracy of the model at that point. ....	137
Figure 4.8: Plots of the model accuracy as a function of four parameters, $\alpha$ and CRSS ratios of prism $\langle a \rangle$ , pyramidal $\langle a \rangle$ , and pyramidal $\langle c+a \rangle$ in the model. The model accuracy is quantified using the fraction of correct predictions. ....	138
Figure A1: The AFM data of indent topographies a and b in 3D. a) Topography of indent a. b) Topography of indent b. c) The differences in topographies of a and b. ....	151
Figure B1: SEM images of single slip accommodation cases 1-4. ....	152
Figure B2: SEM images of single slip accommodation cases 5-8. ....	153
Figure B3: SEM images of single slip accommodation cases 9-12. ....	154
Figure B4: SEM images of single slip accommodation cases 13-16. ....	155
Figure B5: SEM images of double slip accommodation cases 1-4. ....	156
Figure B6: SEM images of double slip accommodation cases 5 and 6 (Note that there is a twinning involved shown as yellow dotted line in the EBSD map inset, in the accommodating deformation system in case 6). ....	157
Figure B7: AFM measurements of double slip accommodation cases 1-6. ....	158

## KEY TO SYMBOLS AND ABBREVIATIONS

AFM	atomic force microscopy
$A$	area of an nanoindentation
$a$	hardening exponent
BFGS	Broyden-Fletcher-Goldfarb-Shanno minimization routine
BSE	backscattered electron
BX	bi-crystal
$\mathbf{b}$	Burgers vector
$\Delta\mathbf{b}$	residual Burgers vector in the grain boundary
CPFEM	crystal plasticity finite element model
CRSS	critical resolved shear stress
$\mathbb{C}$	fourth-order stiffness tensor
$c_{i=1,2,3}$	relative activity of primary, secondary, and tertiary slip system
DAXM	differential aperture X-ray microscopy
$\mathbf{d}$	unit vector of slip direction in current work
EBSD	electron backscattered diffraction
EXP	experiment
$\mathbf{e}$	slip plane normal in Livingston and Chalmers' notation
$E_e$	elastic Green's Lagrangian strain
FIB	focused ion beam
$\mathbf{F}$	deformation gradient
$\mathbf{F}_e$	elastic deformation gradient

$\mathbf{F}_p$	plastic deformation gradient
$F_{gb}$	a grain boundary fracture metric
GND	geometric necessary dislocation
GUI	graphical user interfaces
$\mathbf{g}$	slip direction in Livingston and Chalmers' notation
$\mathbf{g}_{TEM}$	g vector in a TEM image
$h^\beta$	self-hardening matrix
$h^{\alpha\beta}$	hardening matrix
$h_0^\beta$	initial hardening slope of slip system $\beta$
$h_0$	initial hardening slope for all slip systems
$h_a(r, \theta)$	height of an indent topography at a point $(r, \theta)$ in a polar coordinate system
$h_a(x, y)$	height of an indent topography at a point $(x, y)$ in Cartesian coordinate system
HR-EBSD	high resolution electron backscattered diffraction
ISR	iterative stress relief
$\mathbf{I}$	second order Identity tensor
IPF	inverse pole figure
$k_y$	Hall-Petch slope
$l$	direction of the slip plane trace on the grain boundary.
$\mathbf{L}_p$	plastic velocity gradient
$M$	LRB' geometric slip transfer parameter
MPIE	Max-Planck-Institut für Eisenforschung
$m'$	Luster and Morris' geometric slip transfer parameter
$m_{tw}$	Schmid factor for a specific deformation twinning system

$M_b$	Guo <i>et al.</i> 's geometric slip transfer parameter
$M_s$	Shen <i>et al.</i> 's geometric slip transfer parameter
$n$	stress exponent in the CPFEE model
$\mathbf{n}$	unit vector of slip plane normal in current work
$\mathbf{n}^{\text{surface}}$	unit vector of specimen surface normal
$\mathbf{n}_{\text{gb}}$	unit vector normal to a grain boundary
$N$	number of dislocations in a slip band
$N_{\text{LC}}$	Livingston and Chalmers' geometric slip transfer parameter
orig	originating (incoming grain in slip transfer)
$q^{\alpha\beta}$	cross-hardening matrix
recv	receiving (outgoing grain in slip transfer)
RSS	resolved shear stress
$r_{\text{in}}$	the approximate indentation impression radius
SE	secondary electron
SEM	scanning electron microscopy
SiC	silicon carbide
SIM	simulation
SX	single crystal
$S$	second Piola-Kirchhoff stress
TEM	transmission electron microscopy
$t$	unit normal of the habit plane of the twins
$\mathbf{U}_{p,t}$	tangential part of the plastic distortion tensor
$\dot{\mathbf{U}}_{\text{pl}}^A/\dot{\mathbf{U}}_{\text{pl}}^B$	plastic distortion rate in grain A/B

$V_{SX}^{\text{receiving}}$	volume of single crystal indent topography in the receiving grain
$V_{\text{sim}}^{\text{receiving}}$	volume of simulated indent topography in the receiving grain
$\Delta V_{a,b}^{(A)}$	volume difference between two indentation topographies $a$ and $b$ over the area $A$
$X_{mn}$	estimated width of each slip/twin band
$\alpha$	weighting factor in the iterative stress relief model
$\beta$	threshold of relative activity in the iterative stress relief model
$\xi$	the angle between direction of the FIB cut and the grain boundary normal
$\psi$	angle between the slip plane traces on the grain boundary
$\kappa$	angles between Burgers vectors in incoming and outgoing grains
$\phi$	angle between slip plane normals of incoming and outgoing systems
$\theta$	grain boundary inclination
$\sigma_0$	normalized global stress tensor
$\sigma_{\text{global}}$	global stress tensor
$\sigma_{i=1,2,3}$	local stress tensor
$\tau$	resolved shear stress tensor
$\tau_0$	initial slip resistance
$\tau_{\text{sat}}$	saturation slip resistance
$\tau_{\text{cr}}^{\alpha}$	critical resolved shear stress of slip system $\alpha$
$\tau_s^{\beta}$	saturation stress of slip system $\beta$
$\dot{\gamma}_0$	shear rate
$\dot{\gamma}_i^A/\dot{\gamma}_i^B$	shear rate of slip system $i$ in grain A
$\dot{\gamma}_i^{\text{in}}$	shear rate of slip system $i$ in the incoming grain

$\pi$

the ratio of the circumference of a circle to the diameter

## CHAPTER 1 INTRODUCTION AND LITERATURE REVIEW

Materials are believed to define the limit of what modern engineering can achieve. Breakthroughs in material science or discovery of new materials is the foundation of many new emerging technologies. This is especially true in the development of new metals and alloys. Despite the over 2000 years of study of metals/alloys in history, there is still a strong need for metals with higher strength, ductility, and resistance to cracking, as well as other superior physical properties. The traditional approach to developing new alloys or improving existing alloys has always been rather straightforward and constant: through a careful examination of the microstructure and an involved study of the deformation mechanism, an informed decision was made on how to adjust the material composition or develop new material processing conditions. Therefore, it is very beneficial to learn the material microstructure and understand the governing rules of deformation in that material. Furthermore, with the rapid growth of computing power, the ability to model material deformation in any industrial processing has become more crucial than ever. This can only be realized efficiently if deformation of metals and alloys in both macro- and micro-scale can be precisely characterized.

### **1.1 Understanding heterogeneous plastic deformation near grain boundaries**

The study of deformation mechanisms in metals is usually based on the dislocation theory proposed by G.I. Taylor [1]. The theory revealed that plastic deformation of metals is always realized by the movement of a fundamental line structure called a dislocation. Thus, the study of deformation mechanisms in metals can be achieved by learning the behavior of dislocations. The dislocation theory has been validated and proven to be sufficient to explain deformation in

metals in most circumstances [1-3]. While current dislocation theory is sufficient to describe movement of dislocations under homogenous stress and strain field, there are still gaps in understanding how dislocations interact with grain boundaries where heterogenous stress/strain fields dominate [4]. A lack of knowledge of how dislocations behave in the vicinity of grain boundaries will lead to inaccurate estimation of how and where the stress concentrates and the cracks initiate on the grain boundary. As a result, it is crucial that more effort is devoted into the study of how metal deforms near a grain boundary in a quantitative manner.

## **1.2 Study of heterogeneous deformation at grain boundaries using slip transfer criteria**

As the dislocation theory explains, when dislocations move towards a grain boundary, the stress field of the dislocation will be repelled by the stress field of the grain boundary (in common cases), creating a pile-up of dislocations towards the grain boundary. When the stress reaches a certain threshold as the number of dislocations in the pile-up increases, the piling dislocation will then pass through the grain boundary. This explanation pictures a very sensible scenario of dislocation passing through grain boundary in a rather qualitative way. However, to quantitatively describe this dislocation slip transfer process, it is desirable to find the answer to these two questions: Do dislocations experience the same magnitude of repelling stress at different types of grain boundaries, and if a dislocation slipped across a grain boundary, how will adjacent grain respond.

### **1.2.1 Slip transfer criterion involving only one outgoing slip system**

Efforts to resolve these two questions have led to the establishment of various slip transfer criterion. The majority of these slip transfer criterion are based on the assumption that one

incoming slip system triggers a unique outgoing slip system, despite the fact that a secondary outgoing slip system or even a tertiary outgoing slip system are often required to fully accommodate the shear of the incoming slip system. Such simplification of the slip transfer problem is mainly due to the fact that in most scenarios the primary outgoing slip system can already relieve the majority of the incoming shear, hence in those scenarios it is reasonable to approximate the slip transfer by assuming only one outgoing slip system is activated. Another reason for considering only one outgoing slip system is the increasingly complexity of the problem as secondary and tertiary outgoing slip systems are considered. As a result, theories of slip transfer that concerns only one outgoing slip systems are firstly reviewed.

The first major breakthrough was made by Livingston and Chalmers in 1957 [5]. In their experiment, they conducted aluminum bi-crystal compression test and analyzed the dislocation activities near the grain boundary using the slip traces on the sample surface. Livingston and Chalmers found that the primary slip system, which is prominent both inside the grain and at the grain boundary, can activate multiple (up to three) slip systems in the vicinity of grain boundary, due to requirement of strain continuity at the grain boundary. In addition, Livingston and Chalmers proposed a geometric parameter  $N_{LC}$  that uses the information of primary slip system to predict the type of outgoing slip system(s).

$$N_{LC} = (\mathbf{e}_{in} \cdot \mathbf{e}_{out})(\mathbf{g}_{in} \cdot \mathbf{g}_{out}) + (\mathbf{e}_{in} \cdot \mathbf{g}_{out})(\mathbf{g}_{in} \cdot \mathbf{e}_{out}) \quad \text{Eq. 1.1}$$

where  $\mathbf{e}$  and  $\mathbf{g}$  are the slip plane normal and slip direction respectively, and the subscripts 'in' and 'out' indicate incoming and outgoing slip systems. In their theory, the slip transfer usually occurs between the incoming and outgoing slip systems that maximize the magnitude of  $N_{LC}$ .

A more general consideration of slip transfer criterion was proposed by Shen *et al.* [6, 7]. Based on the observation of dislocation transfer across grain boundaries in 304 stainless steel via

TEM, Shen *et al.* used four different criteria to predict the outgoing slip system. (1) The first criterion is identical to the geometric parameter  $N_{LC}$  used by Livingston and Chalmers. (2) Shen *et al.* developed a new metric  $M_s$  based on the assumption that the rotation of the dislocation line from the incoming to the outgoing slip plane is the rate limiting step in dislocation transmission.  $M_s$  can be expressed as follows:

$$M_s = (\mathbf{L}_{in} \cdot \mathbf{L}_{out}) \times (\mathbf{g}_{in} \cdot \mathbf{g}_{out}) \quad \text{Eq. 1.2}$$

where the  $\mathbf{L}_{in}$  and  $\mathbf{L}_{out}$  are the lines of intersection between grain boundary and the slip planes of incoming and outgoing slip systems, respectively, and  $\mathbf{g}_{in}$  and  $\mathbf{g}_{out}$  are the slip directions of the incoming and outgoing slip systems. (3) The force acting on an emitted dislocation across from the pile-up should be maximized for the slip propagation to take place. (4) This criterion combines the geometric and stress field contributions in that it used criterion 2 to predict the outgoing slip plane and criterion 3 to predict the outgoing slip directions. By testing all four models at five different grain boundaries, criterion 4 proves to be the most accurate. Shen *et al.*'s work revealed that a precise slip transfer model cannot solely rely on the geometric relationship between incoming and outgoing slip systems, because the revolved shear stress on outgoing slip system is another component that strongly influence which outgoing slip system will be activated.

In the light of the previous effort, Clark *et al.* [8] proposed a set of three conditions for determining the outgoing slip system:

1) the slip plane on which the dislocation will be emitted is chosen as that for which the angle between slip traces is a minimum.

2) the slip direction within the plane selected in 1) is chosen as that on which the resolved shear stress, on the emission side of the interface, is a maximum near the intersection of the slip plane and the boundary.

3) if the resolved shear stresses calculated in 2) are close for two or more slip directions, the activated system is that which minimizes the residual grain boundary dislocation energy left in the interface.

In Clark *et al.*'s criterion, the influence of residual Burgers vector was accounted for in the slip transfer for the first time. Lee, Robertson, and Birnbaum also independently proposed a similar slip transfer criterion [9, 10] similar to Clark's theory, and this theory was proved to be the most comprehensive and accurate slip transfer criterion to date. The theory was named LRB criterion and can be expressed as follow:

1) The angle between the traces of the slip planes on the grain boundary plane should be a minimum. This is generally expressed using the LRB parameter:

$$M = \cos\psi\cos\kappa \quad \text{Eq. 1.3}$$

where  $\psi$  is the angle between traces of slip planes in the grain boundary and  $\kappa$  is the angle between Burgers vectors of the incoming and outgoing slip system. An illustration of the two angles was shown in Fig. 1.1.

2) The resolved shear stress on the outgoing slip system:

$$\tau = \boldsymbol{\sigma} : (\mathbf{d}_{\text{out}} \otimes \mathbf{n}_{\text{out}}) \quad \text{Eq.1.4}$$

should be maximized, where the  $\tau$  stands for the resolved shear stress on a slip system,  $\boldsymbol{\sigma}$  is the local stress state in the vicinity of the slip transfer location, and  $\mathbf{d}_{\text{out}}$  and  $\mathbf{n}_{\text{out}}$  are the slip directions and slip plane normal of outgoing slip systems, respectively.

3) The magnitude of the Burgers vector in the grain boundary should be minimized.

In addition to the criterion proposed above, a simple geometric criterion was introduced by Luster and Morris [11] as  $m' = \cos\phi \cos\kappa$ , where  $\phi$  and  $\kappa$  are the angles between slip plane normal and Burgers vectors, respectively.  $m'$  is advantageous due to its reasonable accuracy for describing most slip transfer events given its easy accessibility without the laborious effort of finding out the grain boundary inclination below surface.

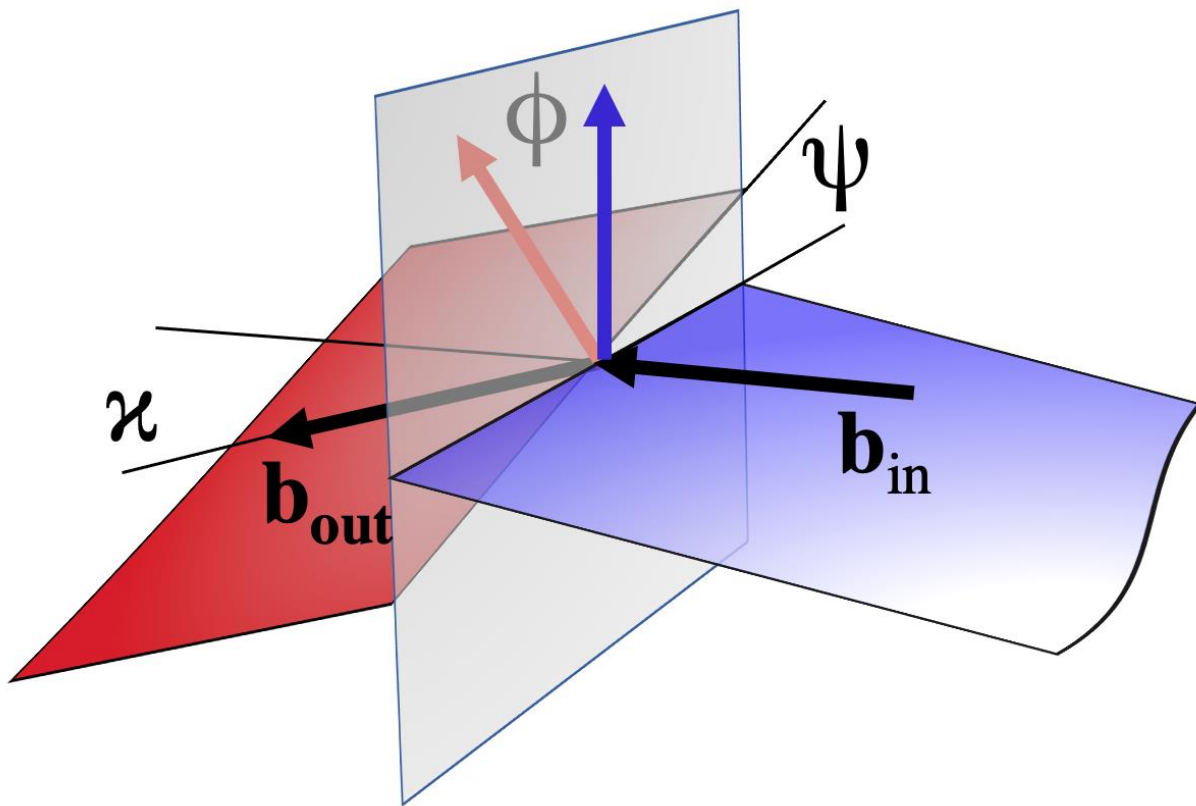


Figure 1.1: Slip transfer geometry at a grain boundary.

## 1.2.2 Multiple outgoing slip system accommodation predicted using tangential continuity theory

A common theme amongst the simple slip accommodation criteria outlined above is the explicit assumption that slip from a single system in one grain is accommodated by a single system in its neighboring grain, despite the fact that it is quite possible, or even likely, that strain accommodation can occur on multiple slip systems. Livingston and Chalmers have attempted to determine what slip systems are involved in the accommodation by requiring continuity of the resulting grain boundary deformation [5]. This approach, often termed “tangential continuity” has been studied and improved by several studies [12-19]. Nonetheless, the overall underlying physics remains unchanged and can be compactly expressed by stating that the plastic distortion rates on either side of the grain boundary ( $\dot{U}_{pl}^A$  and  $\dot{U}_{pl}^B$ ) must affect the grain boundary plane in the same way, i.e.

$$\begin{aligned} (\dot{U}_{pl}^A - \dot{U}_{pl}^B)\mathbf{v} &= 0 \text{ or} \\ (\dot{U}_{pl}^A - \dot{U}_{pl}^B)(\mathbf{I} - \mathbf{n}_{gb} \otimes \mathbf{n}_{gb}) &= 0, \end{aligned} \quad \text{Eq. 1.5}$$

where  $\mathbf{v}$  is an arbitrary vector in the grain boundary plane (i.e. normal to the grain boundary normal  $\mathbf{n}$ ) and  $\mathbf{I}$  is the second rank identity tensor. Considering that the plastic distortion rates are superpositions of individual slip system activity in grain *A* and grain *B* (Indexed by *i* and *j*), the overall activity in the vicinity of a grain boundary needs to be fulfilled:

$$(\sum \dot{\gamma}_i^A \mathbf{d}_i^A \otimes \mathbf{n}_i^A - \sum \dot{\gamma}_j^B \mathbf{d}_j^B \otimes \mathbf{n}_j^B)(\mathbf{I} - \mathbf{n}_{gb} \otimes \mathbf{n}_{gb}) = 0 \quad \text{Eq. 1.6}$$

While perfect tangential continuity may not be realistic because slip transfer generally leaves residual Burgers vector content in the grain boundary, one can nevertheless use Eq. 1.6 to identify such slip activity that minimizes discontinuity for given incoming slip, i.e.

$$\min (\sum \dot{\gamma}^{in} \mathbf{d}^{in} \otimes \mathbf{n}^{in} + \sum \dot{\gamma}_i^A \mathbf{d}_i^A \otimes \mathbf{n}_i^A - \sum \dot{\gamma}_j^B \mathbf{d}_j^B \otimes \mathbf{n}_j^B)(\mathbf{I} - \mathbf{n}_{gb} \otimes \mathbf{n}_{gb}) \quad \text{Eq. 1.7}$$

While the tangential continuity model has the potential to predict which deformation systems associated with shear transfer will be activated, its pure kinematic nature suggests that it disregards the effect of an imposed state of stress as well as the influence of the residual Burgers vector left in the grain boundary<sup>1</sup>. Therefore, it is still desirable to further study the physics of slip transfer across grain boundaries of varying nature and develop a new model that can account for multiple outgoing slip systems with the consideration of local stress state and residual Burgers vector.

### **1.3 State of the art experimental techniques and simulation methodology used in slip transfer study**

To determine which slip transfer/accommodation criterion most accurately describes the interaction between dislocation and grain boundary, experimental methods that are dedicated to the study of the heterogenous deformation in the vicinity of the grain boundary needs to be established. Past research has applied several experimental procedures to achieve this goal, which includes bi-crystal nanoindentations, micro-pillar compression/indentation, and orientation informed surface slip trace analysis. Each technique has its own limitations and advantages. Nonetheless all of them have gained us insights into the mechanisms of slip-grain boundary interplay from different length scales and aspects.

---

<sup>1</sup> C. Fressengeas *et al.* has attempted in their latest work [12] to implement tangential continuity into a crystal plasticity finite element framework. In their methodology, the tangential continuity serves as a fitness function to modify the local stress tensor.

### 1.3.1 Bi-crystal/quasi bi-crystal nanoindentation

Bi-crystal nanoindentation, compared to the in-situ TEM, micro-pillar compression, and slip trace analysis, is faster and less laborious in studying slip transfer. It only requires accurate measurement of the indentation location in the grain boundary vicinity and the real-time load-displacement curves during the indenting (This can be achieved by the instrumented nanoindentation [20, 21]). Nevertheless, due to the complex stress state caused by the indentation, the data analysis of bi-crystal nanoindentation is always complicated and convoluted. Much effort has been dedicated to deconvoluting the influence of grain boundaries on slip transfer from bi-crystal nanoindentation.

Ya. M. Soifer *et al.* [22] studied the nano-hardness of copper in the vicinity of the grain boundaries using instrumented nanoindentations and found that the nano-hardness is influenced by the distance between the indent location and the grain boundary. As shown in figure. 1.2 the influence of the grain boundary on the nano-hardness in the right grain can be felt when the distance between the indent and grain boundary falls within 1.4  $\mu\text{m}$ . In addition, the influence of the grain boundaries on the nano-hardness in the left (negative part of the horizontal axis) and right (positive part of the horizontal axis) grains are significantly different. While the nano-hardness remains steady as the distance between indent and grain boundary reduces in the left grain, a dramatic rise of the nano-hardness in the right grain is observed as the indent approaches the grain boundary. This indicates that there is no significant resistance to plastic deformation during the indentation in the left grain, but a high resistance to plastic deformation in the right grain causes the increase of the nano-hardness. The different behaviors of the grain boundary in response to the plastic deformation caused by nanoindentation provides a unique way to study the role of grain boundaries using nano-hardness.

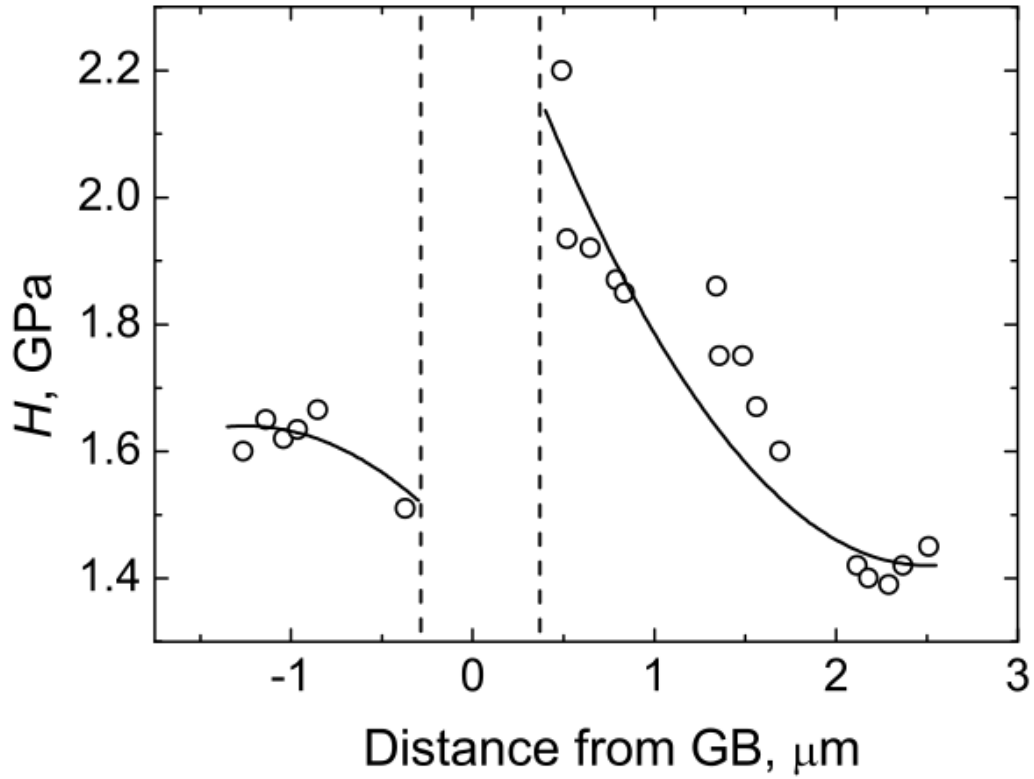


Figure 1.2: Nanohardness as a function of the distance between each indentation and the grain boundary. Each data point represents one indentation measurement. [22]

In the light of Soifer *et al*'s study on indentations near grain boundaries, P.C. Wo *et al.* [23] studied the influence of various grain boundaries on plastic deformation in Ni<sub>3</sub>Al using nanoindentations carried out in the vicinity of those grain boundaries. Instead of characterizing each indentation with nano-hardness, they categorized all grain boundary indents into three groups and examples of each group are shown in Fig. 1.3 in three separate rows. The first row (Fig. 1.3a) gives an example of grain boundary blocking the plastic deformation generated by the indentation, which are manifested by absence of slip traces on the neighboring side of the grain boundary in the SEM backscattered image. In contrast in the Fig. 1.3b, limited slip lines developed across the grain boundary, suggesting a smaller grain boundary resistance to plastic strain compared to the first scenario. In the Fig. 1.3c, abundant slip traces are observed in the neighboring grain and the presence of the grain boundary does appear to influence the development of those slip traces, indicating minimal grain boundary resistance to slip transfer in this case. Furthermore, they found a correlation between the three types of grain boundary indents and a slip transfer parameter  $m'$ , which are summarized in the table 1.1. They concluded from table 1.1 that the ease of slip transmission in Ni<sub>3</sub>Al seems to correlate with the value of  $m'$ . At grain boundaries with low  $m'$  values (row 1-4), the slip trace of the indentation was blocked by the grain boundary (shown as type B). With higher values of  $m'$ , the slip trace of the indentation is able to travel across the grain boundary (shown as type I) even without much change of the direction of the slip trace (shown as type T). This study suggests that more insights can be gained by correlating the slip traces developed in bi-crystal indentation to slip transfer geometry.

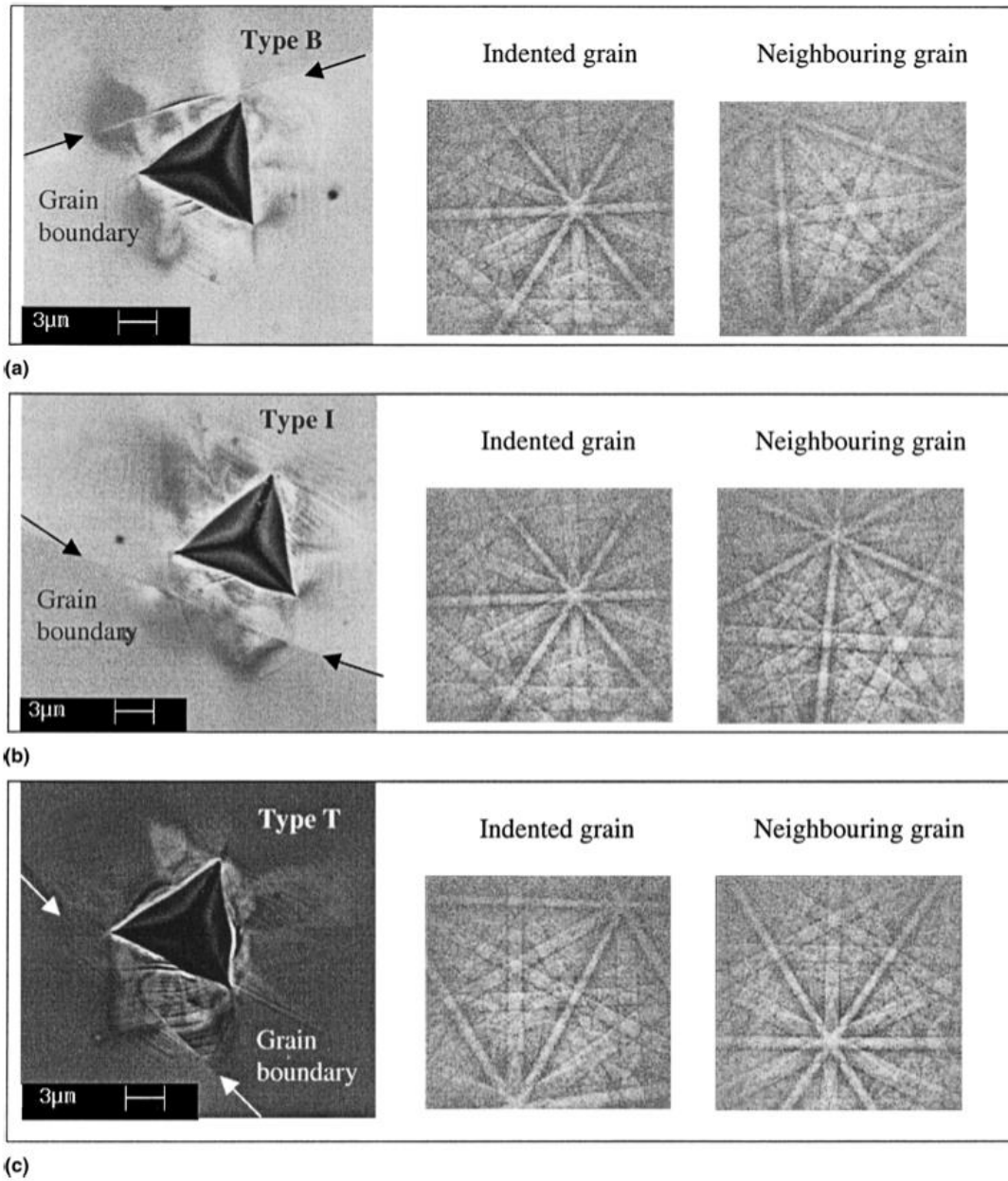


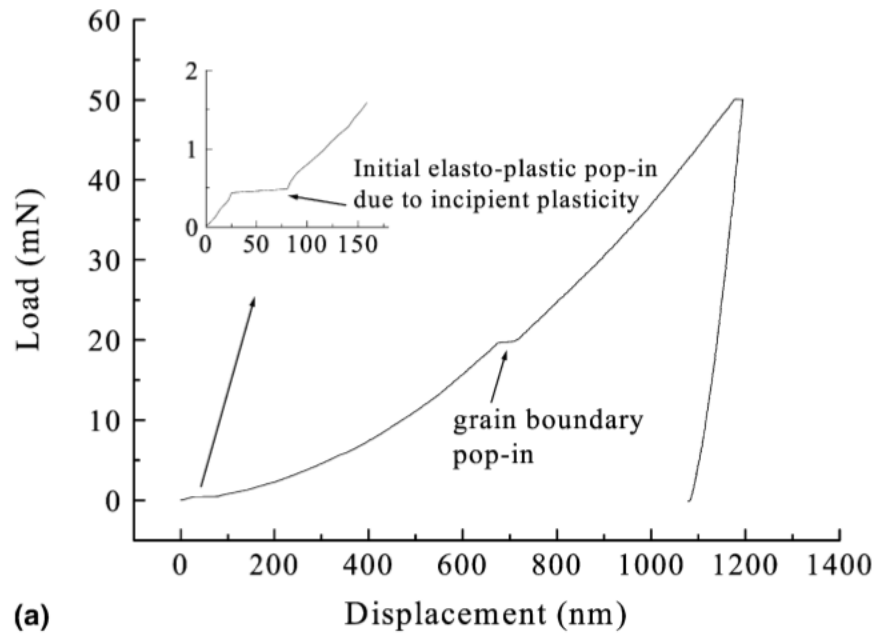
Figure 1.3: SEM images of nanoindentations at three types of grain boundaries and the corresponding EBSD patterns in the indented and neighboring grain. (a): Slip band caused by nanoindentations were blocked by the grain boundary (noted as type B). (b): Intermediate slip band development in the neighboring grain (noted as type I). (c): Full slip transmission across the grain boundary (noted as type T). [23]

Table 1.1: Column 2-6: Slip geometry of all grain boundaries including disorientations (column 5) measured using the patterns in fig. 3 and  $m'$  (column 4) which is the multiplication of column 2 and 3. Column 7 is the deformation behavior at grain boundaries where the type B, I, and T suggests slip band blocking, intermediate slip transmission, and slip transmission, respectively.

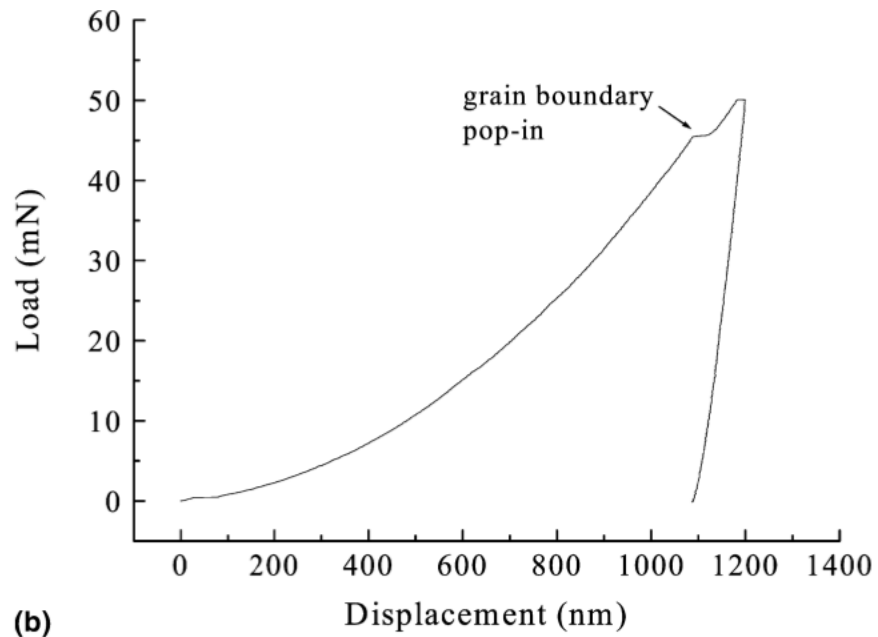
[23]

Related grains	$\cos(\theta_A)$	$\cos(\theta_B)$	$m'$	Disorientation $\theta/UVW$	Coincident size lattice	Deformation behavior at grain boundary (Fig. 7)
GB <sub>A</sub>	0.9102845	0.8860473	0.81	44.2°/1-1-4	...	Type B
GB <sub>B</sub>	0.8941368	0.8775367	0.78	38.7°/1-40	...	Type B
GB <sub>C</sub>	0.8498666	0.8879597	0.75	40.4°/100	Near $\Sigma 5$ and $\Sigma 29b$	Type B
GB <sub>D</sub>	0.8958527	0.8517548	0.76	40.5°/100	Near $\Sigma 5$ and $\Sigma 29b$	Type B
GB <sub>E</sub>	0.9556497	0.9327741	0.89	33.6°/1-4-1	...	Type I
GB <sub>F</sub>	0.9918736	0.9667900	0.96	17.1°/4-41	...	Type I
GB <sub>G</sub>	0.9970575	0.9907858	0.99	17.0°/-12-1	...	Type T
GB <sub>H</sub>	0.9960494	0.9922302	0.99	30.4°/-14-2	...	Type T

In addition to the study of the influence of grain boundaries on nano-hardness and slip trace development in bi-crystal nanoindentation, Wang *et al.* [24] studied the load-displacement curves in a bi-crystal nanoindentation experiment and used displacement jumps on the load-displacement curves to characterize the plastic deformation near the grain boundary. They discovered that the yielding of a grain boundary can be observed in a load-displacement curve during a load controlled bi-crystal nanoindentation (Load controlled mode means the indentation load was maintained constant throughout the process). When the nano-indenter presses the dislocations through a grain boundary, the yielding of the grain boundary releases the excess energy that is stored in the dislocation pile-ups in the origin grain. This process leads to a displacement jump on a load-displacement curve. In theory, the size of the displacement jump is correlated with the energy of the dislocations pile-ups. However, this correlation was not revealed in Wang *et al.*'s work and the grain boundary yielding was not observed near every grain boundary. Two examples of the displacement jumps are shown in Fig. 1.4, where the two nanoindenters were placed at different distances to the grain boundary and as a result the displacement jumps occurred at different load. With more detailed analysis, it was found out that displacement jumps tend to occur at grain boundaries with higher  $m'$  values, especially above 0.9. They argued that the displacement jumps were caused by slip transmission across those grain boundaries, and the absence of the displacement jumps at grain boundaries with low  $m'$  values were attributed to the blockage of slip band by grain boundaries.



(a)



(b)

Figure 1.4: Load-displacement curves of nanoindentations near two grain boundaries showing displacement jumps at different indentation depths and loads. [24]

More generalized analysis of displacement jumps observed on the load-displacement curves of grain boundary nanoindentations were conducted by W. A. Soer *et al.* [25]. In their study, two types of material, including commercially pure Mo bi-crystal with symmetric tile boundary and Fe-14%Si alloy with general grain boundary, were used for bi-crystal nanoindentations. The displacement jumps, which is an indication of grain boundary yielding, were observed only in Fe-14%Si alloy and none was observed in commercially pure Mo. The absence of grain boundary yielding in Mo bi-crystal was attributed to yield stress of a symmetric tile boundary being too low, in which case dislocation pile-ups cannot maintained against the boundary. Furthermore, the grain boundary resistance to slip transmission was quantitatively related to the displacement jumps using a Hall-Petch type calculation using the equation:

$$\tau_a = \tau_0 + \frac{k_y}{\sqrt{d}} \quad \text{Eq. 1.8}$$

where the  $\tau_a$  and  $\tau_0$  indicate the yielding stress of a single crystal nanoindentation and the yielding stress of a bi-crystal nanoindentation, respectively. The distance between the indent and the grain boundary is represented by  $d$ . The Hall-Petch slope is indicated by  $k_y$ .

The Fe-14%Si grain boundary yielding events are summarized in Fig. 1.5. The Hall-Petch slope  $k_y$  was determined to be 0.58, which agrees well with the macroscopically measured value, by measuring the slope of dotted line in Fig. 1.5. Using this methodology, it was concluded that the grain boundary slip resistance can be obtained for various materials.

T. B. Britton *et al.* [26] used similar approach to research the slip resistance of Fe-0.01 wt% C polycrystal and pure copper. They concluded that the grain boundary yielding events in bi-crystal nanoindentations are likely related to interstitials atoms pinning dislocations in the vicinity of the grain boundary. Furthermore, the measured  $k_y$  values agrees well with macroscopic Hall-Petch effect observations.

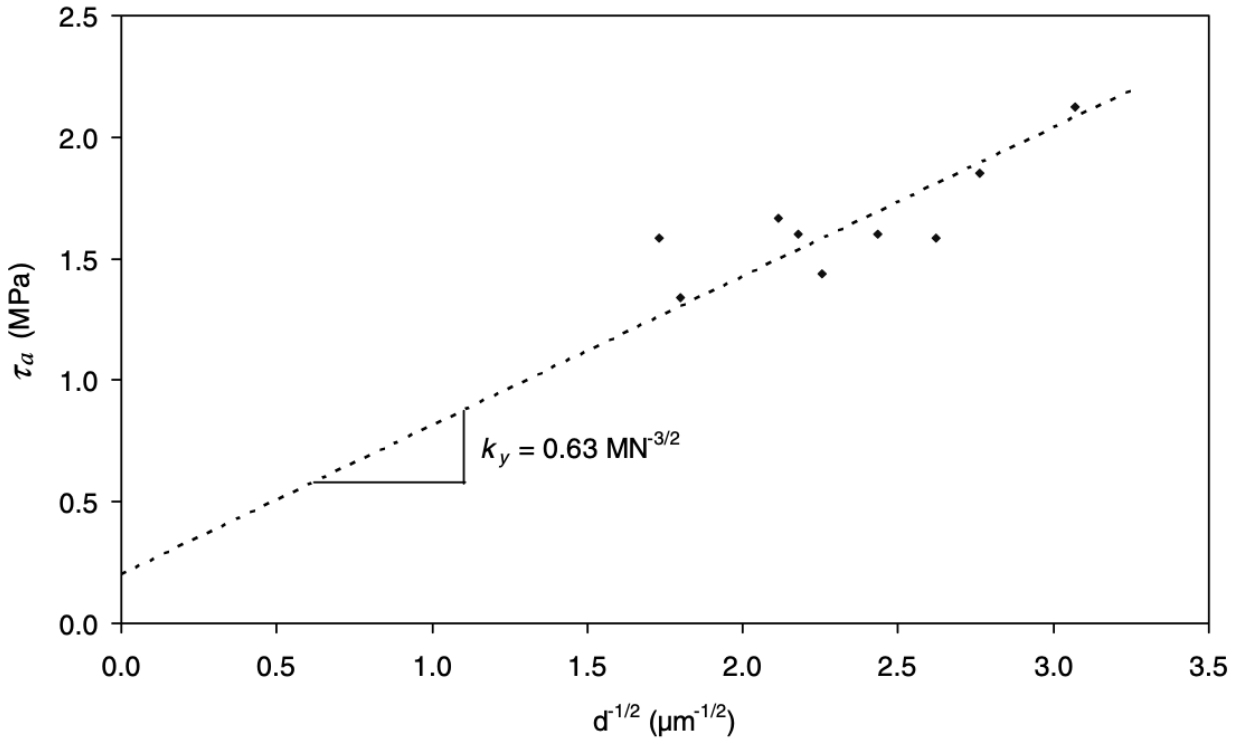


Figure 1.5: Fe-14%Si boundary yielding events shown in a Hall-Petch type plot with the horizontal axis being the inverse square root of the distance between indent and boundary and vertical axis being the applied shear stress. [25]

Most recent research on bi-crystal nanoindentations by Kalidindi *et al.* [27] and Vachhani *et al.* [28, 29] were dedicated to accurately determining the grain boundary yielding stress by converting nanoindentation load-displacement curves into a standard stress-strain curves. In both of these studies, a matrix of nanoindentations located at different distances to the grain boundaries were carried out near eight grain boundaries in high purity polycrystalline aluminum (99.999%). The acquired load-displacement curve of each grain boundary indent was converted into stress-strain curve using the procedures outlined by Kalidindi *et al.* [30-33]. The yield stress of the grain boundary was, then, quantified for each indentation. Figure 1.6 shows the yielding stresses of two grain boundaries, where in the left case the misorientation across the grain boundary is 12.1 degrees and in the right case the misorientation reaches 42.7. It can be observed that the grain boundary on the left side does not affect the yielding stress of all nanoindentations, as the yielding stress remains the same in both grain interior and near grain boundary. This is due to the low misorientation angle across the left grain boundary, which leads to a negligible grain boundary resistance to slip transfer. Nonetheless for the case on the right side, the yielding stress increases significantly when the indent location approaches the grain boundary. The large difference in yielding stress between the grain interior and grain boundary vicinity was caused by the poor misalignment of slip systems on both sides, which is a result of the high misorientation angle between two grains.

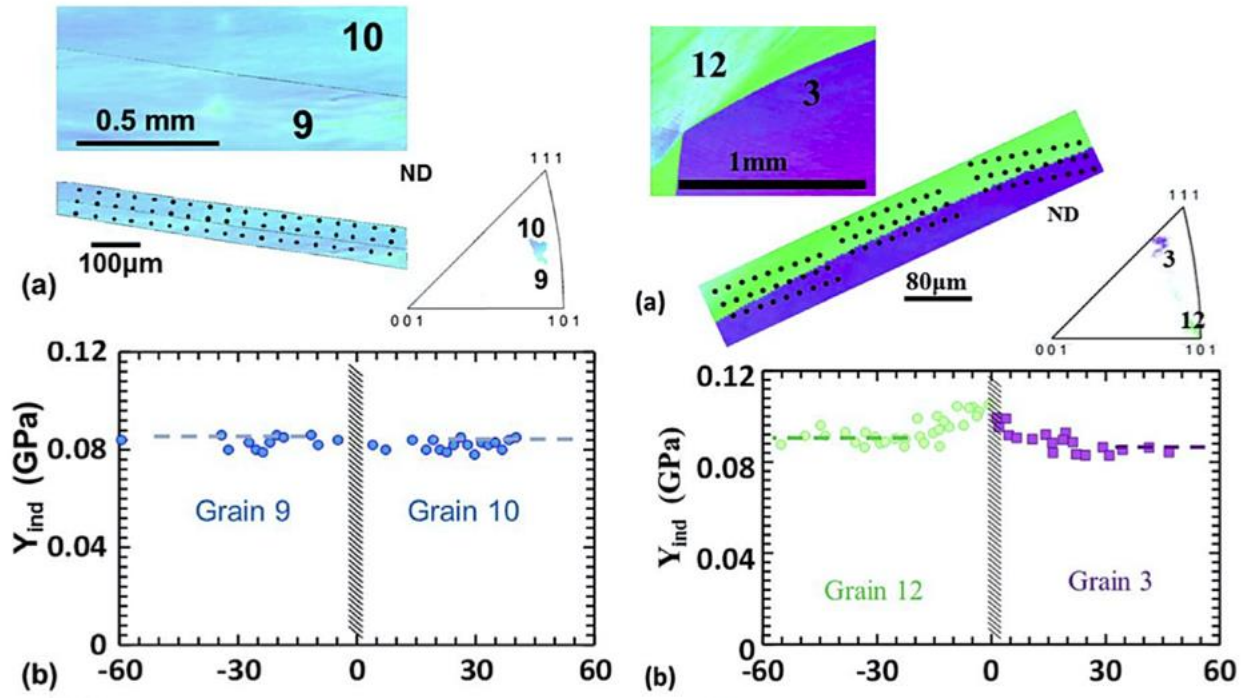


Figure 1.6: (a) Crystallographic details of the two grain boundaries including location of the indents and the orientation of the four indented grains. (b) The yielding stress calculated for each nanoindentations. [27]

Although previous research has proved that the study of grain boundary resistance to slip transfer can be achieved using bi-crystal nanoindentations, there are a few disadvantages to this approach. The complicated stress and strain field in the deformed material in a nanoindentation process is usually very difficult to quantify without powerful simulation tools. As a result, the determination of the active slip systems and their relative shear is impossible using bi-crystal nanoindentation method.

### **1.3.2 Quantitative slip trace analysis**

Many studies have taken a different route to investigate the role of grain boundary in plastic deformation using uniaxial tensile or four point bending test with polycrystalline samples. In these studies, a relatively small amount of uniaxial strain was applied to the sample, then the slip bands/traces that developed at grain boundaries on the surface of those polycrystalline samples can be captured using SEM in a post-mortem examination. With the crystalline orientation of each grain informed, the slip systems and their related Burgers vectors of each observed slip trace can be identified. The most obvious advantage of this methodology, compared to the bi-crystal nanoindentation, is the stress state near a grain boundary can usually be approximated with the global uniaxial tension stress state. This simple stress state facilitates the calculation of the resolved shear stress on each slip system, determining the relative magnitude of driving force on each slip system. This quantified knowledge of slip systems and the resolved shear stress is critical in understanding how heterogenous stress/strain evolves in the boundary vicinity, and can eventually enable one to build models that predict slip activities near all types of grain boundaries.

Highlights of the early studies of slip bands development and evolution near a grain boundary includes in the early work by R. E. Hook and J. P. Hirth [34], who used a bi-crystal of high purity Fe-3%Si alloy to study the influence of grain boundaries on small plastic deformation. The sample was compressed along the grain boundary plane until significant amount of slip band were visible. The slip system that is correlated with each slip band formed near grain boundaries were determined using stereographic projections. Figure 1.7 shows an example of the several types of slip bands developed in the grain boundary vicinity. Those slip bands were examined in terms of the compatibility requirements imposed at the grain boundary plane. It was concluded that while the primary slip band is operated by the global uniaxial compression stress, the secondary slip systems are driven by the local stress state that is the result of the elastic incompatibility at the grain boundary plane. Such activation of secondary slip systems is not normally expected in single crystal deformation. Similar studies regarding the slip bands development near a bi-crystal grain boundary were conducted by R. E. Hook and J. P. Hirth [35] and C. Rey and A. Zaoui [36]. All of these early researches offer insightful arguments on the slip transfer and strain compatibility near a grain boundary under plastic deformation.

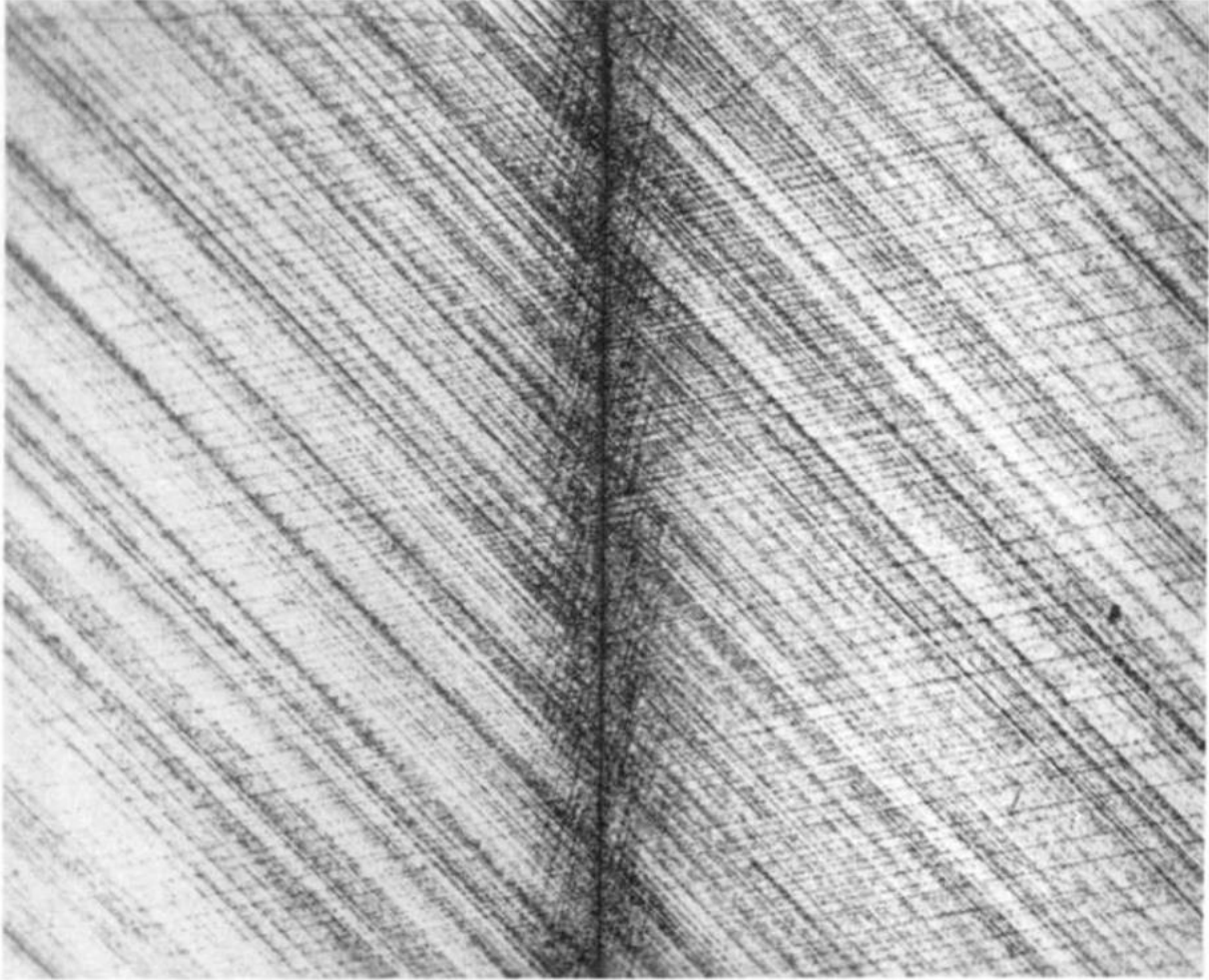


Figure 1.7: An optical image of the primary  $\{011\}$  slip bands and secondary  $\{101\}$  slip bands in the grain boundary vicinity in a compressed bi-crystal sample. [34]

Recent research of slip transfer studied by slip trace analysis in Bieler *et al.* [37] and Alizadeh *et al.* [38] are based on a higher volume of slip transfer data compared to the early work from last century. This is mainly a result of the faster crystal orientation identification using EBSD and the higher resolution and magnification imaging of SEM.

Bieler *et al.* [37] conducted slip trace analysis in an annealed polycrystalline Al with a near-cube microstructure deformed in uniaxial tension. One feature of the near-cube microstructure is that there are usually many active slip systems present at the grain boundary due to the high Schmid factors. With 128 observations of either slip transfer or blockage by grain boundary, obvious slip transfer with correlated slip lines on the grain boundary was rarely observed, instead independent activation of slip was observed in each grain near the boundary. As a result, they concluded that within a near-cube microstructure the slip transfer is more difficult to activate than self-accommodation when there are plenty slip systems with high Schmid factors available in each grain. Both  $m'$  and the product of  $m'$  and global Schmid factor were used to evaluate the likelihood of slip transfer. The results in Fig. 1.8a suggests that the slip transfer only occurs when the slip systems in the incoming and outgoing grains are highly aligned, e.g.  $m' > 0.97$ , which almost certainly corresponds to a low angle grain boundary with misorientation less than  $15^\circ$ . It was also concluded in the study from Fig. 1.8b that a product of Schmid factor and  $m'$  can be used as a threshold for slip transfer below which slip will be blocked by the grain boundary. This study revealed the importance of combining multiple slip transfer metric to more accurately assess the likelihood of slip transfer. However, a near-cube texture is to some extent unique that multiple slip systems in each grain will be active due to the high Schmid factor. As a result, Alizadeh *et al.* [38] carried out similar experiments in both a near-cube and rotate-cube textures.

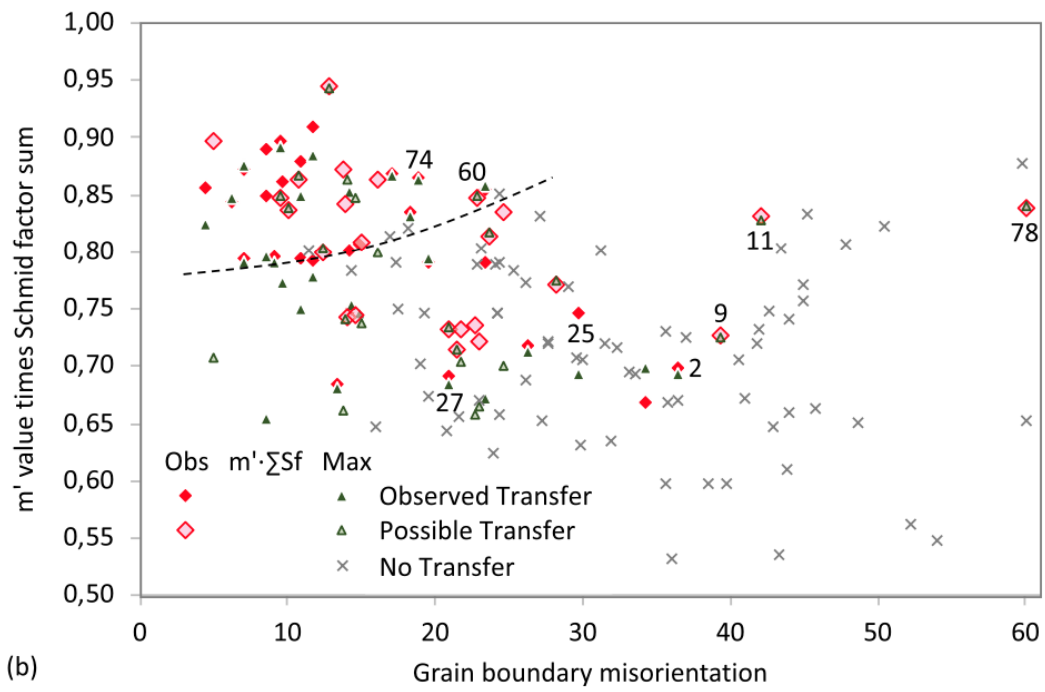
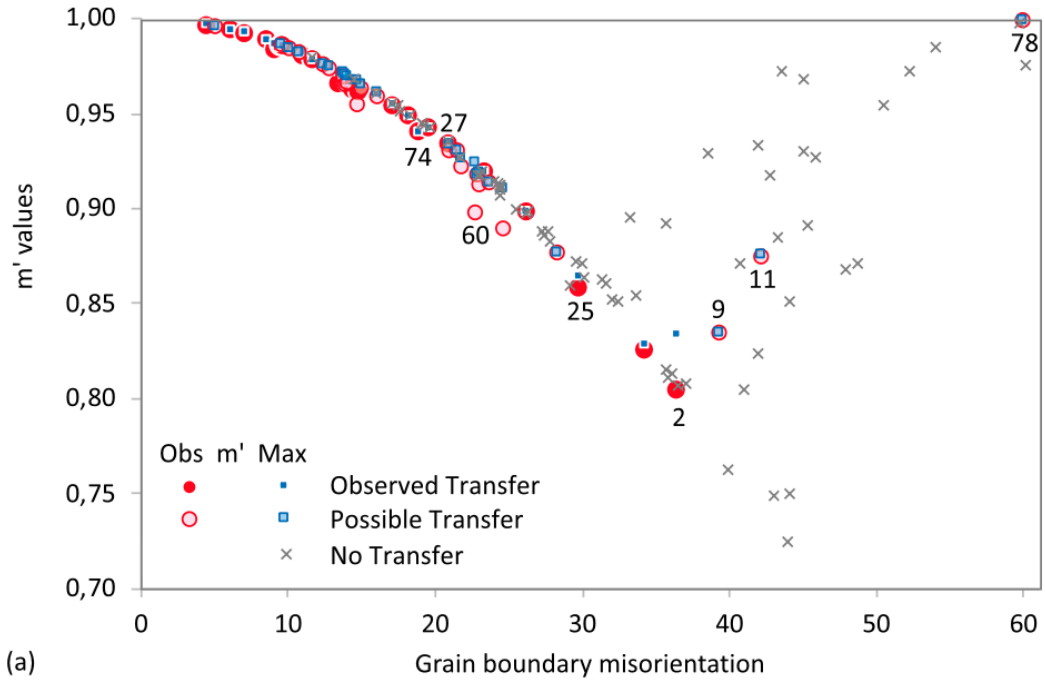


Figure 1.8: (a) A  $m'$  vs grain boundary misorientation plot showing every of slip transfer and slip blockage events as a data point, where dots and crosses means slip transfer and slip blockage, respectively. (b)  $m'$  times Schmid factor vs grain boundary misorientation plot showing the same data set. [37]

In R. Alizadeh *et al.*'s work [38], the slip transfer in high purity polycrystalline aluminum with near-cube and rotated-cube microstructure (examples of the two microstructures are shown in Fig. 1.9) were studied near ~250 grain boundaries, including both successful slip transfer and blockage of slip by grain boundary. The slip systems involved in each slip transfer were identified using the slip trace analysis. Due to the high symmetry of Al, the observed slip trace can always be correlated to multiple slip systems. Under such condition, the one that has the highest Schmid factor was selected to be the active slip system. Three metrics were used to assess the likelihood of slip transfer at the grain boundary, the first two being the  $m'$  and the residual Burgers vector left in the grain boundary  $\Delta b = |\mathbf{b}_{\text{incoming}} - \mathbf{b}_{\text{outgoing}}|$  (where the  $\mathbf{b}_{\text{incoming}}$  and  $\mathbf{b}_{\text{outgoing}}$  is the Burgers vector of the active slip system in the incoming and outgoing grain, respectively) and the third metric was defined by  $m'/\Delta b$ . By applying the three metrics to all 250 observations, they found out that the slip transfer tends to occur when  $m'$  is greater than 0.9 and  $\Delta b$  is smaller than  $0.35b$  ( $b$  is the unit Burgers vector in aluminum). This study suggests that the residual Burgers vector plays a significant role in the slip transfer in aluminum. Furthermore, the third metric  $m'/\Delta b$  seems to be the most useful, where slip transfer usually occurs when the values of  $m'/\Delta b$  exceed a threshold. This conclusion on  $m'/\Delta b$  can be generalized from Fig. 1.10, where the two groups of points indicated by blue and brown (slip transfer and slip blockage) can be separated by a threshold of  $m'/\Delta b$ , where above the threshold the data points are mostly consisted of blue.

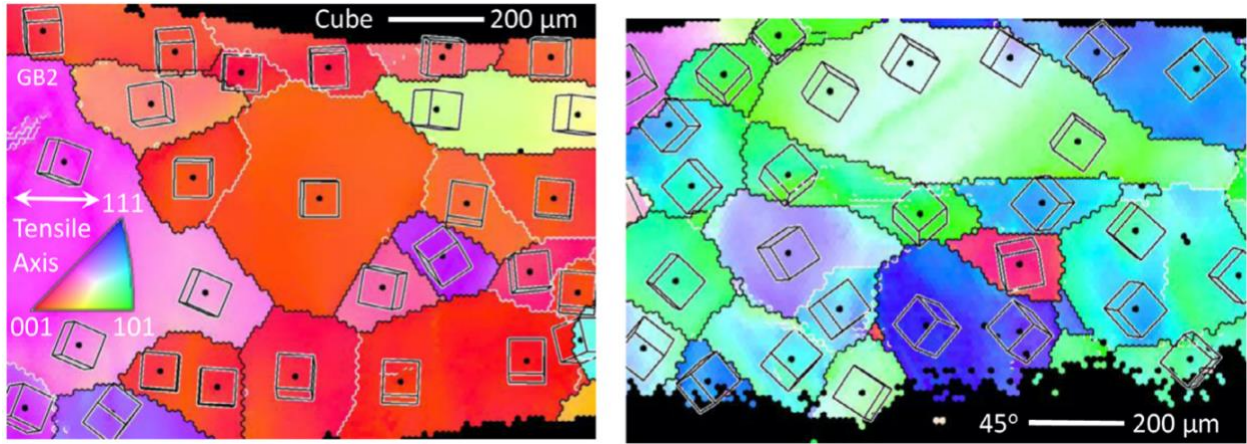


Figure 1.9: Crystal orientation map of the two aluminum samples with dramatic different microstructures, where the left being near-cube and right being rotated cube microstructure. [38]

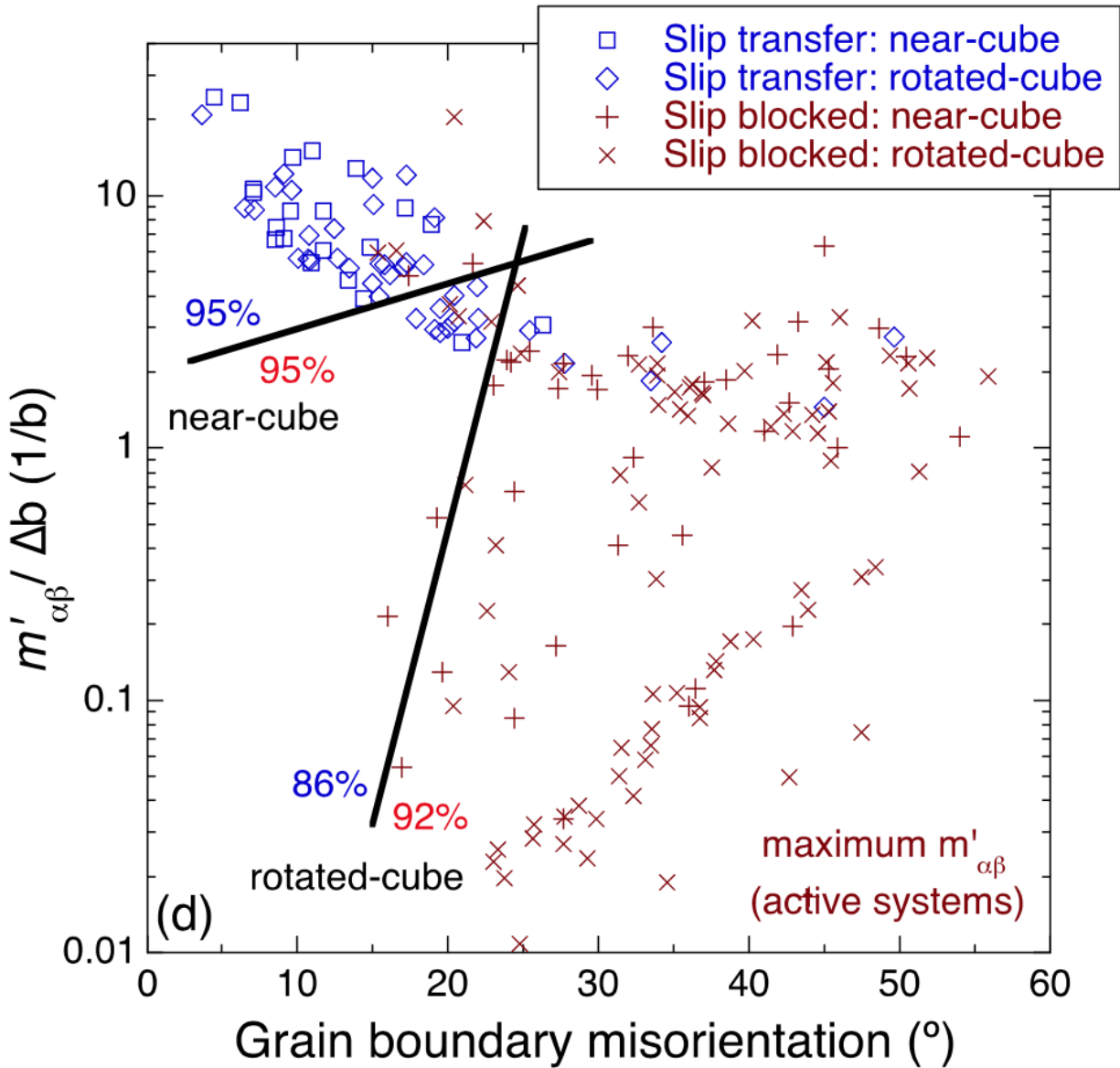


Figure 1.10: A  $\left(\frac{m'}{\Delta b}\right)$  vs grain boundary misorientation plot showing every of slip transfer and slip blockage events as a data point, where blue and brown means slip transfer and slip blockage, respectively. [38]

Another significant contribution to the study of slip transfer by characterizing surface slip trace is made by Guo *et al.* [39], where the slip band-grain boundary interaction was studied in commercially pure titanium using trace analysis and high resolution EBSD (HR-EBSD). The focus of the study was not limited to the slip transfer event, but the stress field development near a slip band blockage by grain boundary was also characterized using HR-EBSD. To predict the possibility of a full slip transfer, they proposed a metric  $M_b$  that incorporates the geometric alignment and the residual Burgers vector and is defined by:

$$M_b = \frac{(\mathbf{n}_i \cdot \mathbf{n}_j)(\mathbf{b}_i \cdot \mathbf{b}_j)}{|\mathbf{b}_i| \cdot |\mathbf{b}_j|} \quad \text{Eq. 1.8}$$

where the  $\mathbf{n}$  and  $\mathbf{b}$  are the slip plane normals and Burgers vectors, respectively. Using the metric  $M_b$ , they concluded that direct slip transfer usually requires good alignment of slip systems, e.g.  $M_b > 0.7$ , with high resolved shear stress on both the incoming and outgoing slip systems.

Between the geometric alignment and resolved shear stress, the study claims that the former plays a more critical role. Poor geometric alignment, e.g.  $M_b < 0.7$ , leads to blocked slip bands. Stress concentration characterized by HR-EBSD was observed only in some of the blocked slip bands vicinity. At the grain boundaries that were blocked, the slip band did not cause obvious stress concentration and GND densities were found to increase in a diffuse distribution along the grain boundary. As a summary of the study, they attempted to correlate both slip transfer and slip band blockage with Schmid factor and slip transfer metric  $M_b$  in Fig. 1.11. All observations were classified into three groups (zone1, 2, 3), which corresponds to slip transfer, blockage with stress concentration, and blockage without stress concentration. Such plots can be used for predicting the type of slip transfer with the knowledge of Schmid factor and metric  $M_b$ .

Nonetheless, the groups in Fig. 1.11 were not clearly divided, with almost 20% outliers and a significant amount of data points located in the vicinity of the division lines. As a result, more

studies are necessary to better quantify the differences of the conditions, under which the slip transfer or the slip band blockage would occur.

In addition to the studies outlined above, there are also plenty of studies that concern the slip transfer and heterogenous deformation near grain boundaries. L. Wang *et al.* [40] examined the slip stimulated twinning in  $\alpha$  Ti using crystal orientation informed slip trace analysis and concluded that this type of slip transfer was possible at  $m'$  greater than 0.9. J. R. Seal *et al.* [41] studied the slip transfer across the  $\alpha/\beta$  interface in a titanium alloy Ti-5Al-2.5Sn (wt.%) using slip trace analysis. It was discovered that the high Schmid factor in both incoming and outgoing grains usually leads to slip transfer alignment, while the alignment of Burgers vector in the  $\alpha$  and  $\beta$  phase was not well correlated with slip transfer. T. R. Bieler *et al.* [42] studied the heterogenous deformation near grain boundaries in tantalum polycrystal.  $m'$  was shown to be a reasonable metric to assess the likelihood of slip transfer in this case.

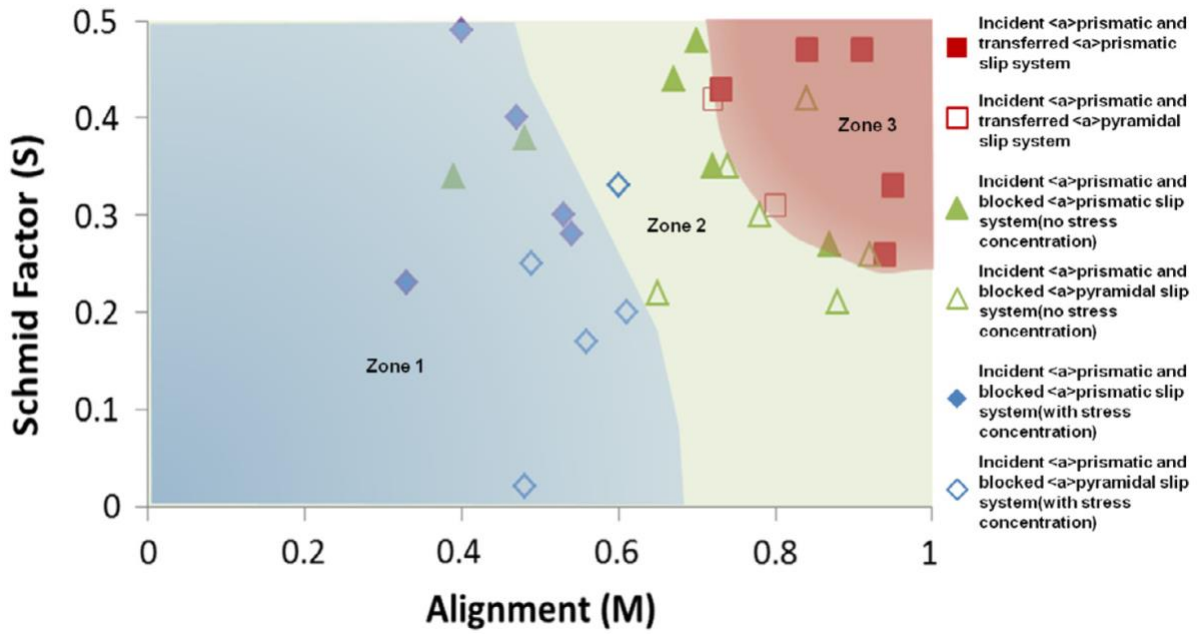


Figure 1.11: Plot of new slip transfer metric  $M_b$  as a function of Schmid factor. The three zones (1,2,3) indicate the direct slip transfer, slip band blockage with stress concentration, and blockage without stress concentration, respectively. [39]

Some slip trace analysis reported in the literature was applied to obtain the slip plane and Burgers vector of the active slip system, Y. Yang *et al.* [43, 44] developed a new methodology that incorporates AFM measurement into the slip trace analysis to quantify the shear involved in each deformation (slip or twin) band. In their study, slip/twin bands in a deformed commercially pure titanium were investigated using AFM, SEM, and EBSD. The slip planes and Burgers vectors were identified using slip trace analysis, while the average shear of each slip band is calculated based on the equation:

$$\gamma = \frac{\mathbf{b}N}{X_{mn} \cdot \mathbf{n}} = \frac{\mathbf{b} \left( \frac{h}{\mathbf{b} \cdot \mathbf{e}_z} \right)}{X_{mn} \cdot \mathbf{n}} \quad \text{Eq. 1.9}$$

where  $\mathbf{b}$  and  $\mathbf{n}$  stand for the Burgers vector and slip plane normal of the slip/twin band,  $h$  is the height of the slip/twin band measured by AFM (shown in Fig. 1.12),  $\mathbf{e}_z$  is the sample surface normal, and  $X_{mn}$  is the estimated width of each slip/twin band. A detailed illustration of how these quantities in the equation is related to AFM measurement is presented in Fig. 1.12. With the shear quantified for each slip/twin band, the shear distribution both in the grain interior and near grain boundary were determined and used for comparison with the results from a CPFE simulations. In their conclusions, it was stated that the magnitude of the measured shear agrees reasonably well with the simulation, while the spatial distribution of the shear is sometimes different. Although the study did not involve any analysis of the correlation between slip transfer and measured shear in each slip band, it provides a useful and convenient way to quantify the shear of slip band. This methodology proved to be very useful in the present study.

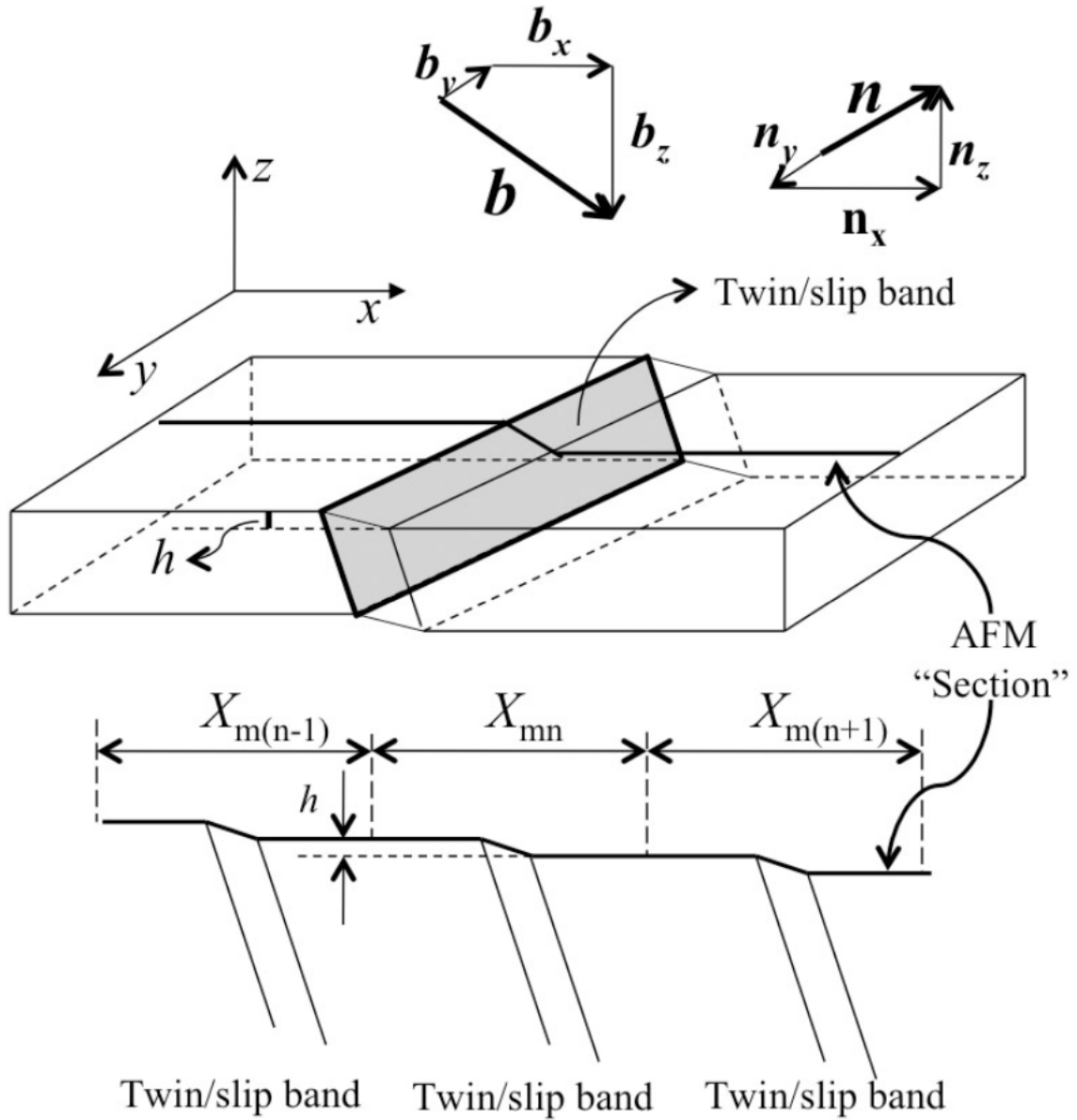


Figure 1.12: Schematic showing how the quantities in equation Eq. 1.9 are correlated with an AFM measurement. [44]

In addition to the application of slip trace analysis to slip band-grain boundary interaction, twin-grain boundary interaction can also be studied in similar approach, some research [45-49] focused on the study of the interaction between impinging deformation twins and  $\gamma$ - $\gamma$  grain boundaries in a  $\gamma$ -TiAl alloy. In their studies, observations suggest that micro-cracks formed at a grain boundary are related to the impinging twins, an example is shown in Fig. 1.13. With the slip plane and Burgers vector identified by slip trace analysis, a grain boundary fracture metric,  $F_{gb}$  that was used for predicting micro-crack formation at grain boundaries was proposed:

$$F_{gb} = m_{tw} |\mathbf{b}_{tw} \cdot \mathbf{t}| \sum_{ord} |\mathbf{b}_{tw} \cdot \mathbf{b}_{ord}|$$

where the  $m_{tw}$  is the Schmid factor for a specific deformation twinning system,  $\mathbf{b}_{tw}$  and  $\mathbf{b}_{ord}$  are the unit Burgers vector of the impinging twin and ordinary dislocation systems in each grain, respectively.  $\mathbf{t}$  is the unit normal of the habit plane of the twins. Further statistical analysis of the magnitudes of  $F_{gb}$  at each grain boundaries suggested that micro-cracks tend to form at grain boundaries with larger magnitude of  $F_{gb}$ .

L. Wang *et al.* [40, 50] conducted related studies regarding the interactions between twins and grain boundaries in  $\alpha$ -Ti. They observed coincident twins at multiple grain boundaries that developed from the same boundary into each grain. With the analysis of slip transfer geometry metric  $m'$ , Schmid factor, and c-axis misorientation between two adjacent grains, they listed three conditions that are necessary for the formation of coincident twinning at a grain boundary: (1) the two grains have a pair of well-aligned twinning systems ( $m' > 0.8$ ) and at least one the system has a high Schmid factor. (2) The c-axis misorientation between the two grains should be less than  $\sim 25^\circ$ . (3) The two adjacent grains should be relatively large in size.

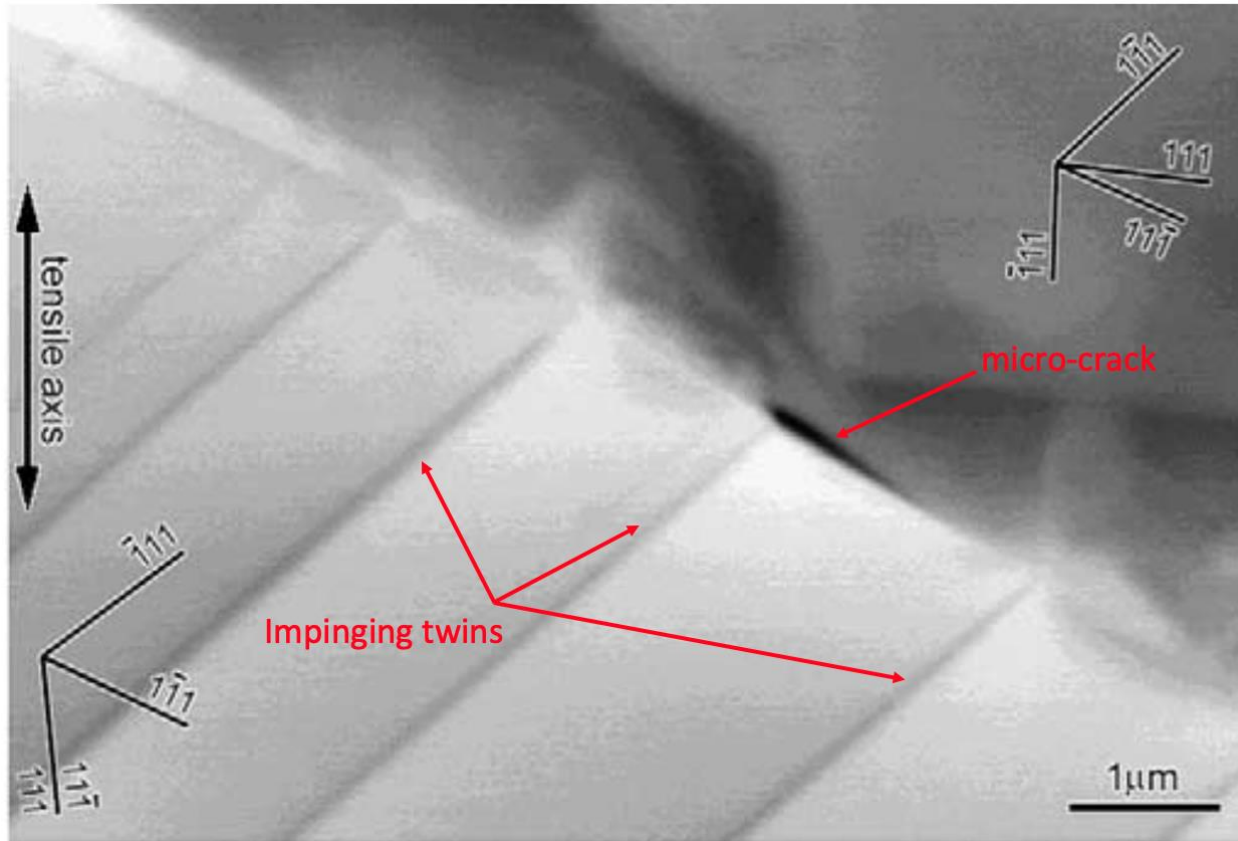


Figure 1.13: A Backscattered image showing the impinging twin initiated a micro-crack at a grain boundary. [45]

### 1.3.3 Other experimental technique

Besides the bi-crystal nanoindentation and slip trace analyses reviewed above, there are also other alternative methodologies that have been used in the research of the interplay between dislocations and grain boundary. A few examples are the study of individual dislocations in a *in/ex-situ* tensile test using TEM, analyzing the slip traces on a compressed micro-pillar that contains a grain boundary (a bi-crystalline micro-pillar), and the estimation of the heterogenous strain/stress fields near grain boundary in a deformed sample using high resolution EBSD. All of these techniques have provided insightful knowledge into the details of individual dislocation interaction with grain boundary on the nano-scale.

J. Kacher *et al.* intensively studied slip transfer in 304 stainless steel [51-55] and  $\alpha$  titanium [56, 57] using both *in-situ* and *ex-situ* straining in the TEM. By identifying the Burgers vector and the slip plane of individual dislocation that has participated in the slip transfer using TEM, the residual Burgers vector in the grain boundary and the resolved shear stress (RSS)  $\tau_{RSS}$  on the potential outgoing slip systems was estimated using  $\mathbf{g}_{TEM} \cdot \mathbf{b}$  analysis and the equation  $\tau_{RSS} = \boldsymbol{\sigma} \cdot \hat{\mathbf{b}} \otimes \hat{\mathbf{n}}$  respectively, for each slip transfer event (the  $\mathbf{b}$  and  $\mathbf{n}$  is the Burgers vector and the slip plane normal respectively, and the  $\boldsymbol{\sigma}$  is the approximated local stress state at the slip transfer location). It was concluded that in both materials the slip transmission across a grain boundary was governed mainly by the reduction of the residual Burgers vector, while the magnitude of the resolved shear stress on the outgoing slip system plays a minor role. In addition to the studies of slip transfer, a novel approach for visualization of grain boundary/dislocation interactions was proposed using tomographic reconstruction. More specifically, a tomograph was constructed using a series of TEM images captured by continuously adjusting the tilt angles. An example of the construction of a tomograph from TEM images is shown in Fig. 1.14, where TEM images

acquired at tilt angles ranging from  $-40^\circ$  to  $40^\circ$  at  $2^\circ$  intervals. In general, this reconstructed tomograph might be helpful in correlating the spatial correlations between the incoming and outgoing bands of dislocations during the slip transfer process.

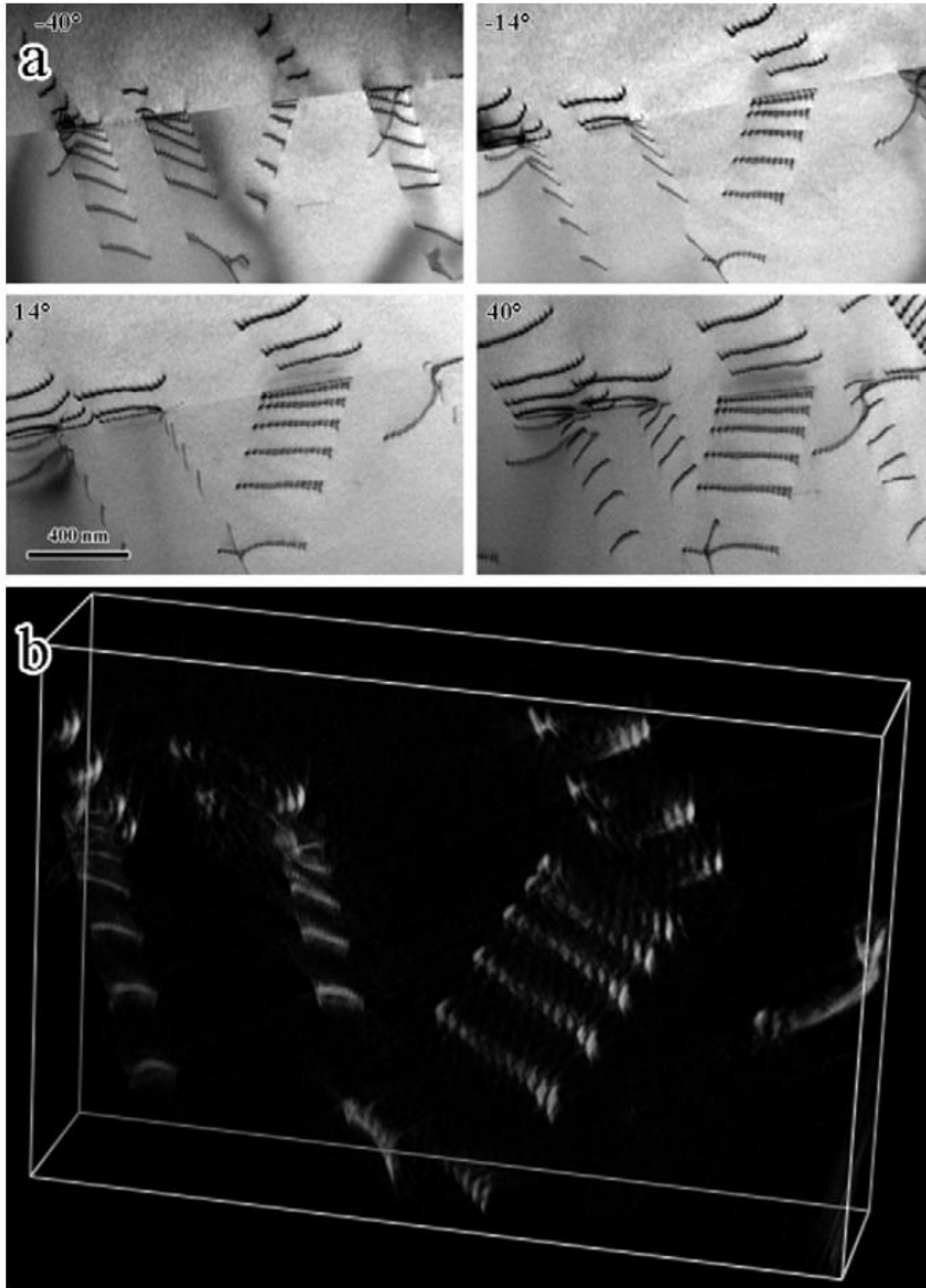


Figure. 1.14: a) The four TEM images acquired at different tilt angles (marked at the top left corner) that were used to construct the tomograph shown in (b). b) The 3-D tomograph revealing the relative locations of each dislocations observed in the TEM image series in (a). [51]

Using *in-situ* TEM, grain boundary/dislocation interactions have also been investigated by several other groups in various materials [58-65]. In general, the unique advantage of *in-situ* TEM is its capability to identify the Burgers vector and the slip plane of individual dislocation, which allows analysis of interaction between a single(few) dislocation(s) and a grain boundary. Nonetheless, such analysis of slip transfer that is based on a rather small number of dislocations and may not be universally applicable, as the governing rules of slip transfer may be different when a large number of dislocations transmitted across the grain boundary.

Compression test of micro-pillars/micro-cantilevers is another approach to deform nano-scale samples. There are quite a few elegant experimental works using this approach to probe the interactions between grain boundaries and dislocations [66-81]. Nonetheless, due to the difficulty of determining the stress state near the grain boundary in a deformed micro-pillar and the strong influence of the size effect of the sample on the material mechanical behavior, the conclusions of those studies on the slip transfer are generally quantitative and sometimes not applicable to larger/bulk specimens and polycrystals.

High resolution EBSD (HR-EBSD) is a relatively new methodology for estimating the strain/stress fields at a sample surface using the Kikuchi patterns from an EBSD scan. Several studies have exploited the advantage of knowing the full strain/stress fields and used them to analyze the heterogenous strain fields in the vicinity of the grain boundary [82-87]. It was, in general, found that grain boundaries with high  $m'$  ( $> 0.9$ ) did not develop any stress concentrations, while those boundaries with  $m'$  ( $< 0.9$ ) developed much higher magnitudes of strain/stress in the boundary vicinity relative to the grain interiors.

### 1.3.4 Coupling experimental results with CPFEM simulations

A general trend in the study of metals and alloys is the increasing used of modeling techniques, such as crystal plasticity finite element modeling (CPFEM), dislocation dynamics simulations (DD), and atomistic simulations. These simulation methods are advantageous to most experimental approaches, due to their capability of acquiring physical quantities that are almost impossible to measure directly in the experiment. In the study of dislocation/grain boundary interactions, simulation tools can be very useful as they allow the assessment of the reactions between dislocations and a boundary at the atomistic level (atomistic simulations) [88-97], the force on any individual dislocation using DD simulations [98-105], and the stress/shear of any slip system using CPFEM [106-117].

With the help of simulation tools, one can couple experimental observations with properly built models to further understand the fundamental physics that governs the experimental observations. Such knowledge, in return, can help improve and develop new experimental and simulation techniques. Latest developments of coupling the experiment and simulation have been summarized in a number of reviews [117-119]. As only CPFEM is used in the present study of slip transfer, the review in this chapter will focus on the research that utilized CPFEM to study the heterogenous deformation near grain boundary.

D. Kumar *et al.* [49] modeled the heterogenous deformation in a duplex near  $\gamma$ -TiAl alloy near a grain boundary where micro-crack nucleation was observed experimentally. The cause of the micro-crack nucleation was experimentally determined to be the result of interactions of deformation twinning with grain boundary. In order to understand how heterogenous stress and strain developed near the site of crack nucleation, CPFEM was used to model the deformation of the two adjacent grains that shared the cracked grain boundary. The microstructure of the

simulated region is shown in Fig. 1.15a where the white circle highlights where the micro-crack was observed in the experiment. Further analysis of the simulated shear is presented in Fig. 1.15(b-d), where the distribution of the shear on the two active twin systems in grain 14 is visualized and plotted as a function of time. The evolution of the shear in Fig. 1.15d suggests that the major twin system near the micro-crack site switched from the  $(-111)[-11-2]$  system to the  $(1-11)[1-1-2]$  system. While the shear on the former system (primary system) was dominant in the early stages of the deformation due to the high global Schmid factor ( $\sim 0.5$ ), the shear on the latter system (secondary system) with a lower global Schmid factor accelerated, presumably caused by the need to maintain grain boundary continuity. As a result, the secondary system, though activated later, contributed more strain to the formation the micro-cracks. This study suggests that the CPFEM can significantly increase the ability to understand the evolution of shear on individual slip system and can potentially be a tool for predicting potential sites for micro-crack nucleation.

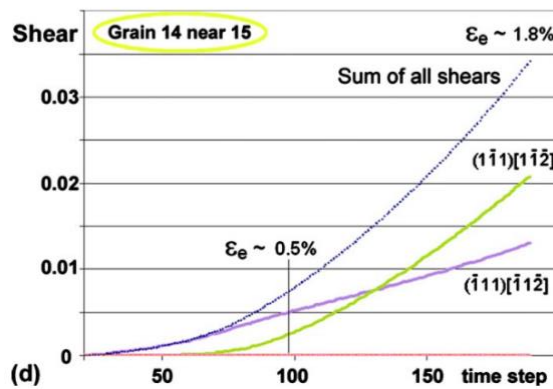
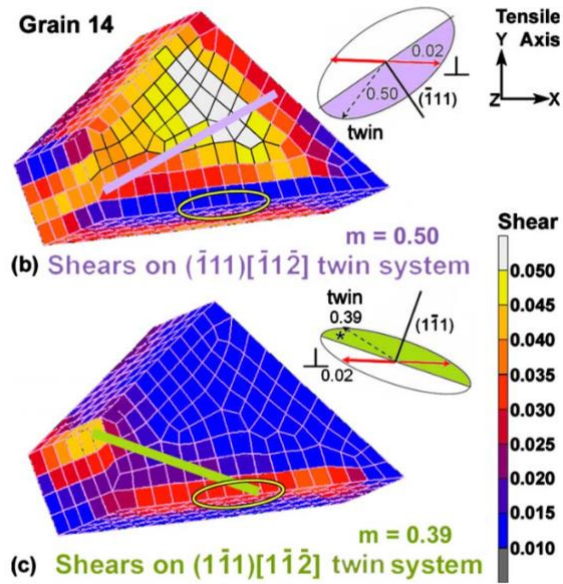
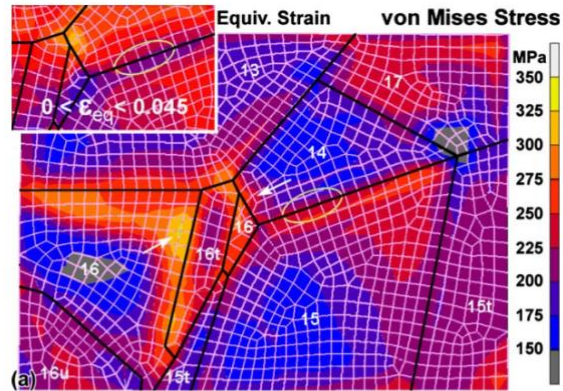


Figure 1.15: a-c): CPFEM modeling of the Von Mises stress (a) and shear distribution (b,c) in the area of interest. d): Evolution of the simulated shear on two slip systems as a function of time. [49]

A more elaborate CPFEM model was used by C. Zhang *et al.* [120] to study the heterogeneous deformation of commercially pure titanium in grain interiors and near grain boundaries. A 3-D CPFEM model was built by using the surface microstructure characterized using EBSD and the sub-surface grain boundary inclination identified by the non-destructive Differential Aperture X-ray Microscopy (DAXM). For comparison, another simpler quasi 3-D model was built using only surface grain orientation. Both models are shown in Fig. 1.16, where the left model contains only columnar grains without any grain boundary morphology under the surface, while the right model contains knowledge of the inclination of some of the sub-surface grain boundaries. By assessing the magnitude of the simulated stress/strain tensor in both models and comparing them with the experimentally estimated local strain, they found out that the 3-D model more accurately captured the values of the local stress tensor than the quasi-3D model. In addition, the comparison revealed that in order to accurately simulate the heterogeneous deformation in the grain interiors and near grain boundaries, it is more important to have an accurate geometrically realistic grain morphology than it is to fine-tune the crystal plasticity constitutive parameters. This study indicates that the necessity of including grain boundary inclination as part of the study of heterogeneous deformation near grain boundary.

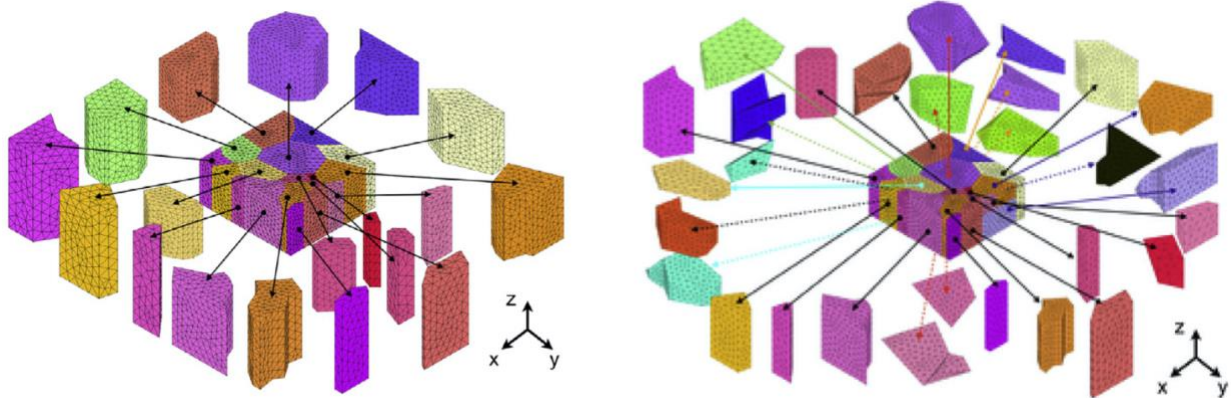


Figure. 1.16: Left image: Quasi-3D CPFE model shows the columnar microstructure of all the grains. Right image: 3D model with grain structure information obtained from DAXM. [120]

Characterization of the heterogeneous deformation near a grain boundary can also be achieved through assessment of the general stress (such as Von Mises stress) and/or strain (second Piola-Kirchhoff stress). For example, CPFEM has been applied to the study of heterogeneous strain field development and localization near grain boundaries at the macro-scale in pure Ni by Guan *et al.* [121]. Such CPFEM assisted in the identification of locations of stress concentrations near grain boundaries. Those predicted locations proved to be in the vicinity of the cracks formed in the experiment. Similar study of the investigation of strain localization using CPFEM can also be found in C. C. Tasan *et al.* [122] and W. Z. Abuzaid *et al.* [85].

In general, despite of numerous studies using CPFEM to characterize heterogeneous deformation in general, the application of CPFEM to the study of heterogeneous deformation near individual grain boundaries is much less common. Nevertheless, such site-specific studies can be very beneficial, as they can focus on specific types of slip transfer (slip transfer at a grain boundary with high  $m'$  can be significantly different than with low  $m'$ ), resulting in more detailed knowledge. Therefore, it is sensible to conduct studies of the slip transfer behavior near individual grain boundaries, and to simulate the deformation process using CPFEM with the goal of learning the specific mechanics of slip transfer at various grain boundaries.

#### **1.4 Motivations of this study**

In the light of previous studies, two major concerns regarding how to quantify the various interactions between slip systems and different types of grain boundaries still remain: A lack of reliable and comprehensive methodology for studying slip transfer with both experimental and CPFEM simulation components, and a model that quantitatively and accurately describe the interaction of multiple slip systems with various grain boundaries. This body of work seeks to

solve these two problems by analyzing slip transfer observations and comparing them with CPFEM simulations to obtain how individual slip systems evolves, which will eventually lead to the development of a new model that can be applied to predicting slip transfer at all types of grain boundaries.

Previous work that tried to combine the experimental observations with CPFEM simulations to study the effect of the grain boundary on the development of the heterogenous stress/strain is quite rare [120-122]. All of them investigated the deformed grain boundaries of a polycrystal in a uniaxial tensile post-mortem test and conducted corresponding simulation in the area of interest with CPFEM. The nature of the post-mortem experiments and the complicated stress/strain development of polycrystalline material means that we are blind to the actual history of the evolution of slip in grain boundary vicinity. In other words, knowledge of the initial formation/nucleation of the slip band at the grain boundary and the direction of the slip transfer across the grain boundary are impossible to acquire. To overcome these disadvantages, precisely located nanoindentation near grain boundaries was conducted. Under such simple bi-crystal nanoindentation environment, it is obvious when and where the slip transfer will occur. In addition, the direction of the slip transfer can also be controlled by placing the nanoindentation on either side of the grain boundaries.

Attempts to theorize the nature of slip transfer across grain boundaries are also not common. Most of the works are limited to the assumption of only one outgoing slip system is triggered by one incoming slip system. Such an assumption can significantly reduce the complexity of the problem, as the activation of a secondary and/or tertiary slip system increases the potential combination of outgoing slip systems dramatically. Traditional tangential continuity theory [5] [12], being the only model that can be used for quantifying multiple slip

system activations near grain boundary. But is also not accurate enough to predict the slip transfer that involves more than one slip system (testing of the traditional tangential continuity model will be conducted in Chapter 4). Improvement of the tangential continuity model and its implementation into crystal plasticity finite element framework is still under progress and not ready for experimental validation [12]. As a result, it is desirable to invent a new model that can be used in cases when multiple slip systems are active near grain boundary. Validation of the model using experimental observations (in our case slip trace analysis) is also critical.

By solving the two problems outlined above, our knowledge of how strain/slip interacts with grain boundaries will be expanded both experimentally and theoretically, meaning that we will be one step closer to building a predictive model that can capture both heterogenous deformation evolution and damage nucleation at grain boundary vicinities.

## **1.5 Overview of this thesis**

An outline is presented here to help reader navigate this dissertation. The main objective of the current work is to quantitatively study the slip transfer near grain boundaries using bi-crystal nanoindentations and slip trace analysis. Simulations using CPFEM are included to obtain additional insights of the deformation mechanisms of individual slip system. An iterative stress relief model (ISRM) is proposed to predict multiple slip system accommodation near grain boundary and it is validated by the comparison with experiments.

Chapter 2 covers the materials that were used in the study, as well as the procedure of sample preparation, the experimental details of the study, and the basic concept of the CPFEM used in the study.

In Chapter 3, the influence of grain boundaries on plastic deformation was studied by conducting nanoindentation near grain boundaries. Surface topographies of indentations near grain boundaries were characterized using atomic force microscopy (AFM) and compared to corresponding single crystal indent topographies collected from indentations in grain interiors. Comparison of the single crystal indents to indents adjacent to low-angle boundaries shows that these boundaries have limited effect on the size and shape of the indent topography. Higher angle boundaries result in a decrease in the pile-up topography observed in the receiving grain, and in some cases increases in the topographic height in the indented grain, indicating deformation transfer across these boundaries is more difficult. A crystal plasticity finite element (CPFE) model of the indentation geometry was built to simulate both the single crystal and the near grain boundary indentation (bi-crystal indentation) deformation process. The accuracy of the model is evaluated by comparing the point-wise volumetric differences between simulated and experimentally measured topographies. The discrepancies between experimental and simulation results will be discussed in terms of reverse plasticity, dislocation nucleation versus glide in the model, and in the physics of the slip transfer process. To remedy the discrepancies between experimental and simulation results, a revision of the original finite element model, which inserted a layer of grain boundary elements between two adjacent grains, was proposed. The new model and its associated modeling parameters are then briefly validated using experimental observations.

In Chapter 4, a new model (ISR) is proposed to quantitatively describe the accommodation/outgoing of slip/shear by multiple deformation systems at a grain boundary. The model uses an iterative approach to sequentially determine the accommodating/outgoing slip systems and their relative shear. The outcome of this iterative stress relief model is mainly

controlled by the continuity of Burgers vector in the grain boundary and the evolution of the impinging stress tensor at the grain boundary. The model was tested by comparing predictions with observations of shear accommodation in  $\alpha$ -Ti quantified using orientation informed slip trace analysis and quantitative atomic force microscopy. Similar comparisons were conducted between tangential continuity model predictions and the experimental observations. Critical resolved shear stress ratios used in this iterative stress relief model were optimized by maximizing the accuracy of the model predictions.

Chapter 5 draws the conclusion of this dissertation and projects the possible ways of continuing the current study.

## CHAPTER 2 MATERIALS, EXPERIMENTAL DETAILS, AND THE CONSTITUTIVE LAW OF CPFEM

### 2.1 Description of material

The grade 2 commercially pure  $\alpha$ -Ti used in this study was acquired from two different sources, and will be designated as Material A and Material B. The studies presented in Chapter 3 and 4 were conducted with Material A and Material B, respectively.

#### 2.1.1 Material A

Material A was provided by the Max-Plank-Institut für Eisenforschung, Düsseldorf, Germany (MPIE). This grade 2 commercially pure  $\alpha$ -Ti was determined to contain 0.17 wt% oxygen and 0.015 wt% carbon using infrared spectroscopy of combustion products. The material had an average grain size of  $\sim 130 \mu\text{m}$ , and was also textured in such a way that the majority of the c-axis of the grains were parallel to the material surface, as shown in the EBSD map in Fig 2.1. Sample A was cut from Material A using electron discharge machining into a size of approximately  $5 \times 5 \times 5 \text{ mm}^3$  and used later for nanoindentation tests.

#### 2.1.2 Material B

Material B was provided by Chris Cowen. The material was textured and had an average grain size of  $80 \mu\text{m}$  as shown in Fig. 2.2. The sample B was cut from Material B with electron discharge machining into a size of approximately  $25 \times 3 \times 2.5 \text{ mm}^3$  for four point bending test.

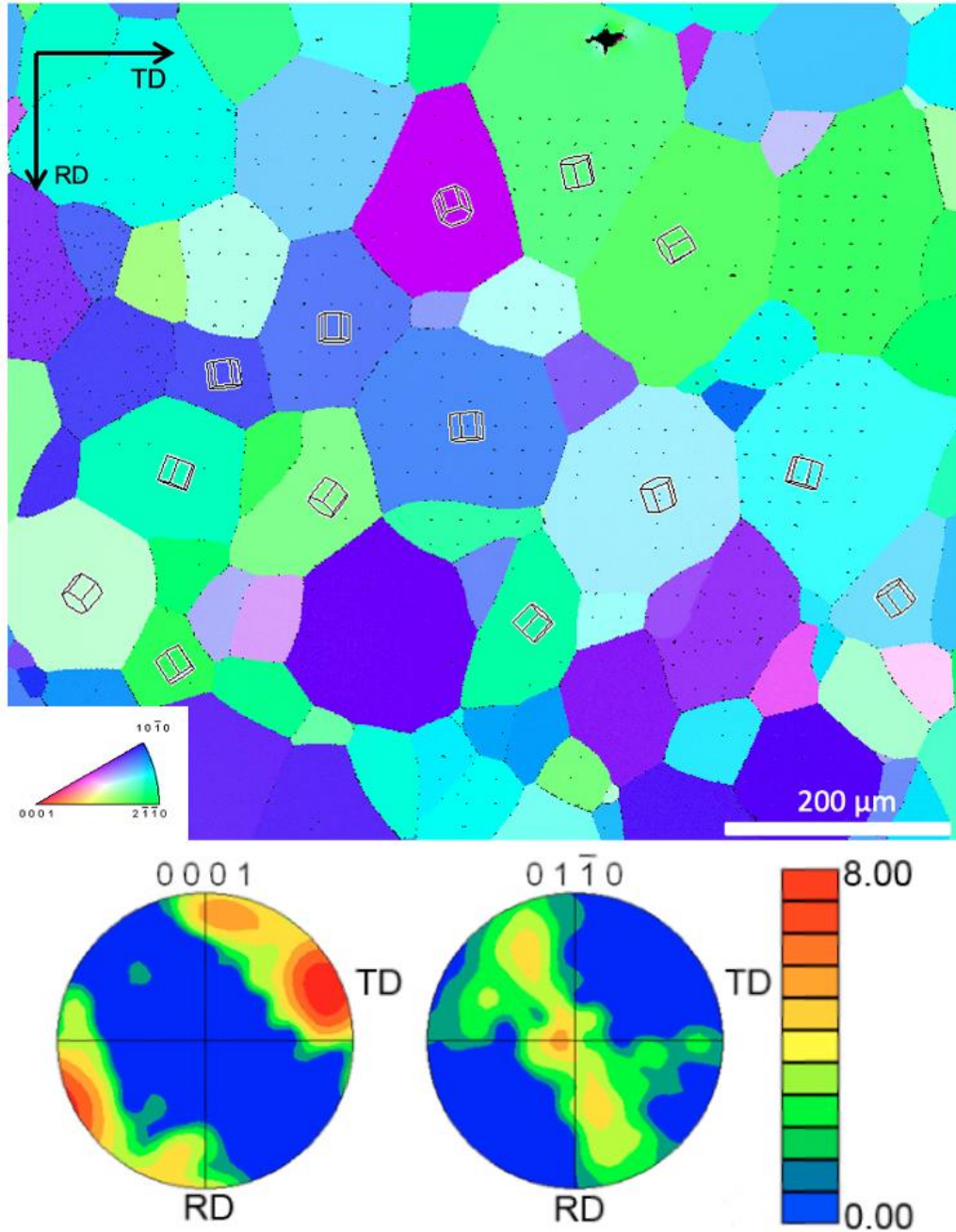


Figure 2.1: An EBSD inverse pole figure (IPF) map of the area of interest in material A is presented. The texture of the material A shows a moderately strong texture with the c-axes lying predominantly in the plane of the image [40]. The array of black dots in the IPF map is a grid of nanoindentations to mark the area of interest.

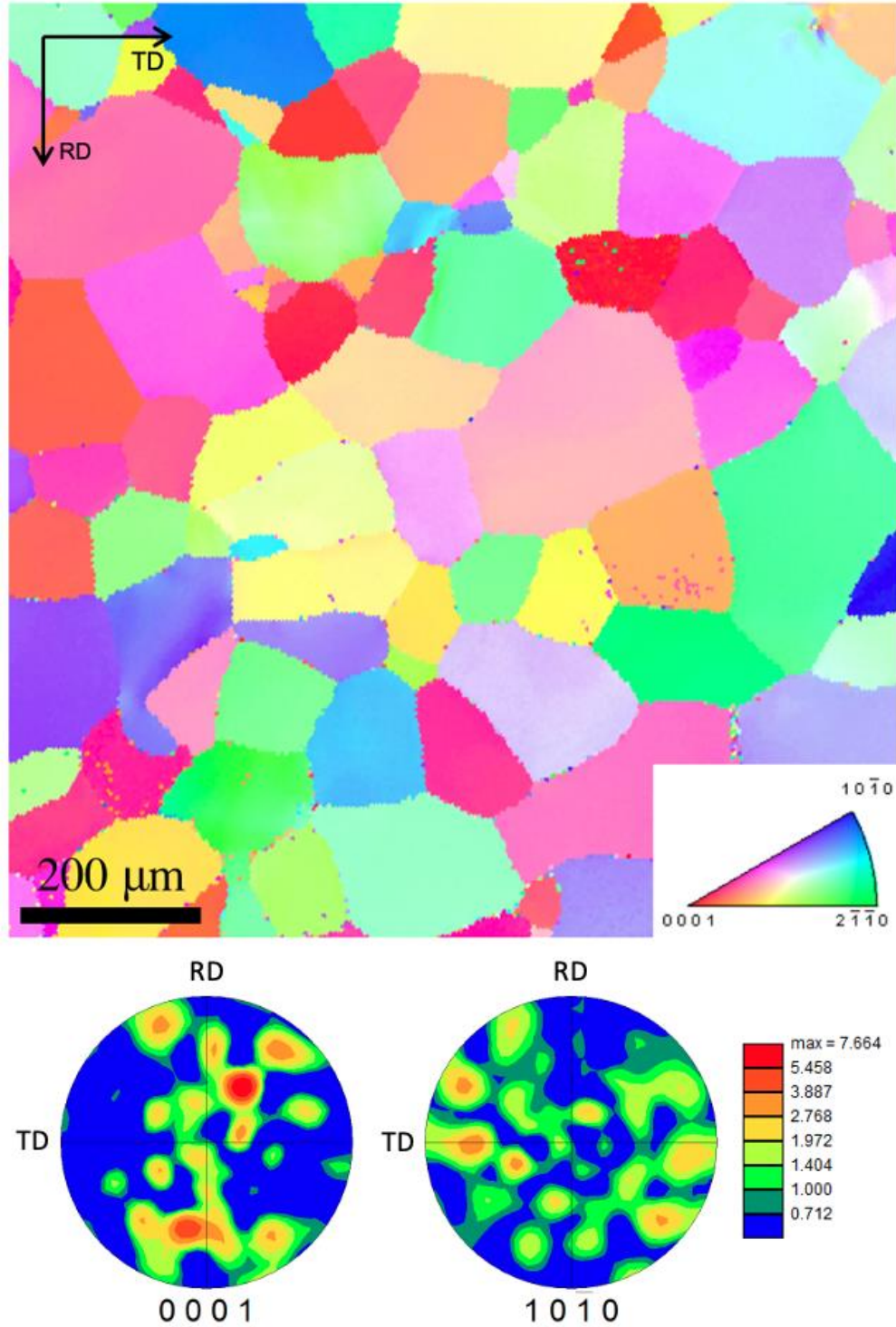


Figure 2.2: An EBSD inverse pole figure map of a random area in material B is presented. The texture of the material B is almost random.

## **2.2 Sample preparation**

### **2.2.1 Sample A**

To mitigate the difficulty in handling the small size of the sample A, it was metallographically mounted in Konductomet<sup>®</sup> (Buehler, Lake Bluff, IL, USA). The sample was then mechanically ground with 400, 600, 1200, 2500, 4000 grit silicon carbide (SiC) paper to achieve a mirror finish with minimal amount of scratches, and then chemical-mechanical polished with a solution consisting of 80 vol% colloidal silica and 20vol% hydrogen peroxide. The sample was then etched with HF. To minimize the residual dislocations caused by the grinding, the final polishing and etching were repeated three times.

### **2.2.2 Sample B**

The sample was mechanically ground from 400 to 4000 grit and polished in a solution consisted of 80 vol% colloidal silica and 20 vol% hydrogen peroxide. To further minimize the influence of the residual dislocations caused by grinding, the sample was electro-polished in a 59% methanol, 35% isopropanol, and 6% perchloric acid (in volume) solution at 38.5 volts and -30° C for about 2 minutes until the channeling patterns of the sample in the SEM was sharp and crisp.

## **2.3 Experimental details**

### **2.3.1 Scanning electron microscopy**

#### **2.3.1.1 Electron imaging**

The two samples, A and B, were imaged using two different SEMs. All electron imaging of sample A was conducted on a high resolution JEOL 6500F (Tokyo, Japan) SEM located in the

Department of Microstructure Physics and Metal Forming, MPIE. All secondary electron (SE) images and backscattered electron (BSE) images were taken at an accelerating voltage of 15 kv and with 1024 x 768 pixel digital resolution.

Sample B was imaged using a Tescan Mira III SEM located in Department of Chemical Engineering and Material Science, Michigan State University. All SE images were acquired using a conventional Everhart-Thornley detector at an accelerating voltage of 20 kv, and BSE images were acquired using a retractable 4-quadrant Si diode detector at 20 kv. All images are captured with 1024x1024 pixel digital resolution.

#### **2.3.1.2 EBSD/OIM scan**

Electron BackScattered Diffraction (EBSD) is a SEM-based technique used to determine crystallographic orientation, phase, and defect densities. Figure 2.3a shows the sample configuration in an SEM to capture the EBSD pattern (Fig. 2.3b).

In this study, the crystallographic orientation of the grains was obtained using either the high resolution JEOL 6500F SEM with EDAX-TSL orientation imaging system or the Tescan Mira III SEM also with an EDAX-TSL orientation imaging system. All EBSD scans were conducted at an accelerating voltage of 20 kv and a working distance between 15-25 mm. The EBSD scan was post-processed using OIM Analysis (TSL, Draper, UT, USA).

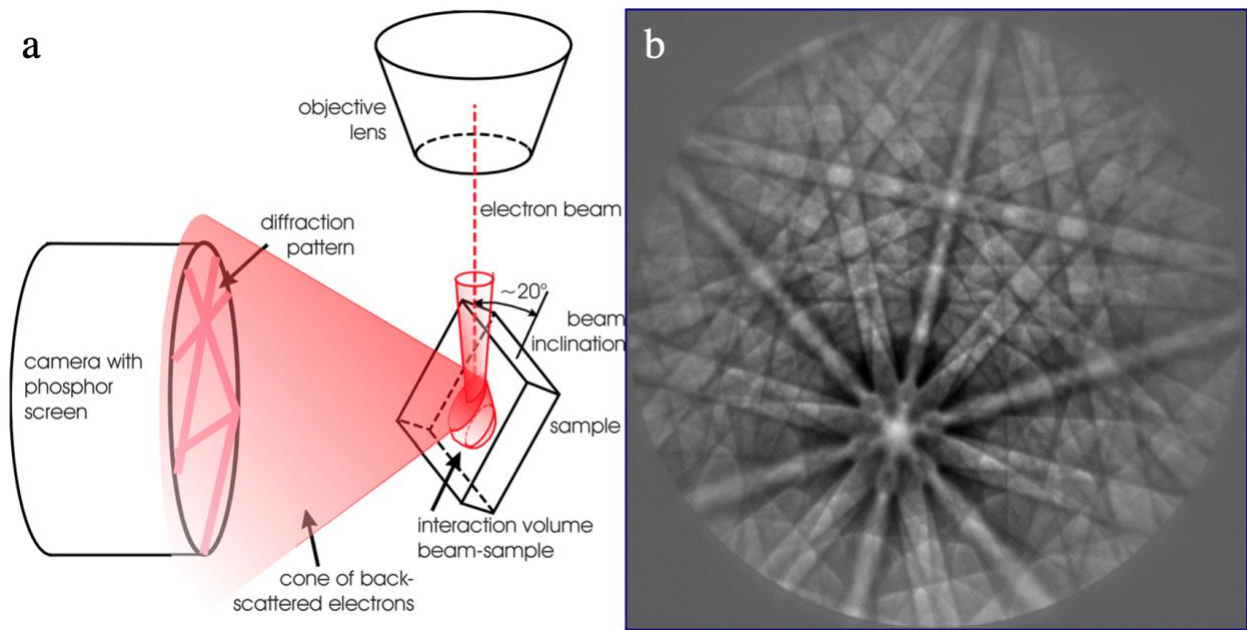


Figure 2.3: A schematic showing the setup of EBSD inside of an SEM (left image) and a typical diffraction pattern (Kikuchi pattern in right image) acquired in the EBSD scan that can be used for determining the crystalline orientation of the diffracted region. (Revised based on the image on <https://www.mpie.de/3077954/EBSD>)

### 2.3.2 Focused Ion Beam (FIB) cross sectioning

Focused Ion Beam (FIB) is a nano-scale technique that allows one to carve/modify the topographies on a sample surface, which is achieved by shooting a focused beam consisting of gallium ions to sputter away the unwanted material.

In this work, FIB was used to expose cross sections of material at grain boundary with the purpose of acquiring grain boundary inclination below sample surface. All FIB cross-sectioning was carried out using a Carl Zeiss (Oberkochen, Germany) Auriga Dual Column focused ion beam scanning electron microscope (FIB-SEM). In addition, the FIB cross-sectioning was conducted in several steps with varying beam currents, from 4nA to 1nA, and ending with 600 pA, to generate a smooth cross-section surface that reveal the location of the grain boundary. Finishing the milling with a low beam current also minimizes the beam damage to the cross-section surface, which may obscure the imaging of the grain boundary on the cross-section. An example of the FIB cross-sectioned grain boundary is shown in Fig. 2.4, where the grain boundary inclination in the image was measured and labeled as  $\theta$ . The accurate grain boundary  $\theta_{\text{correct}}$  was acquired by correcting the  $\theta$  using equation:

$$\tan\theta_{\text{correct}} = \frac{\tan\theta\cos\xi}{\sin(54^\circ)} \quad \text{Eq 2.1}$$

where the  $\xi$  is the angle between direction of the FIB cut and the grain boundary normal and the  $54^\circ$  represents the tilt angle of the sample in the SEM.

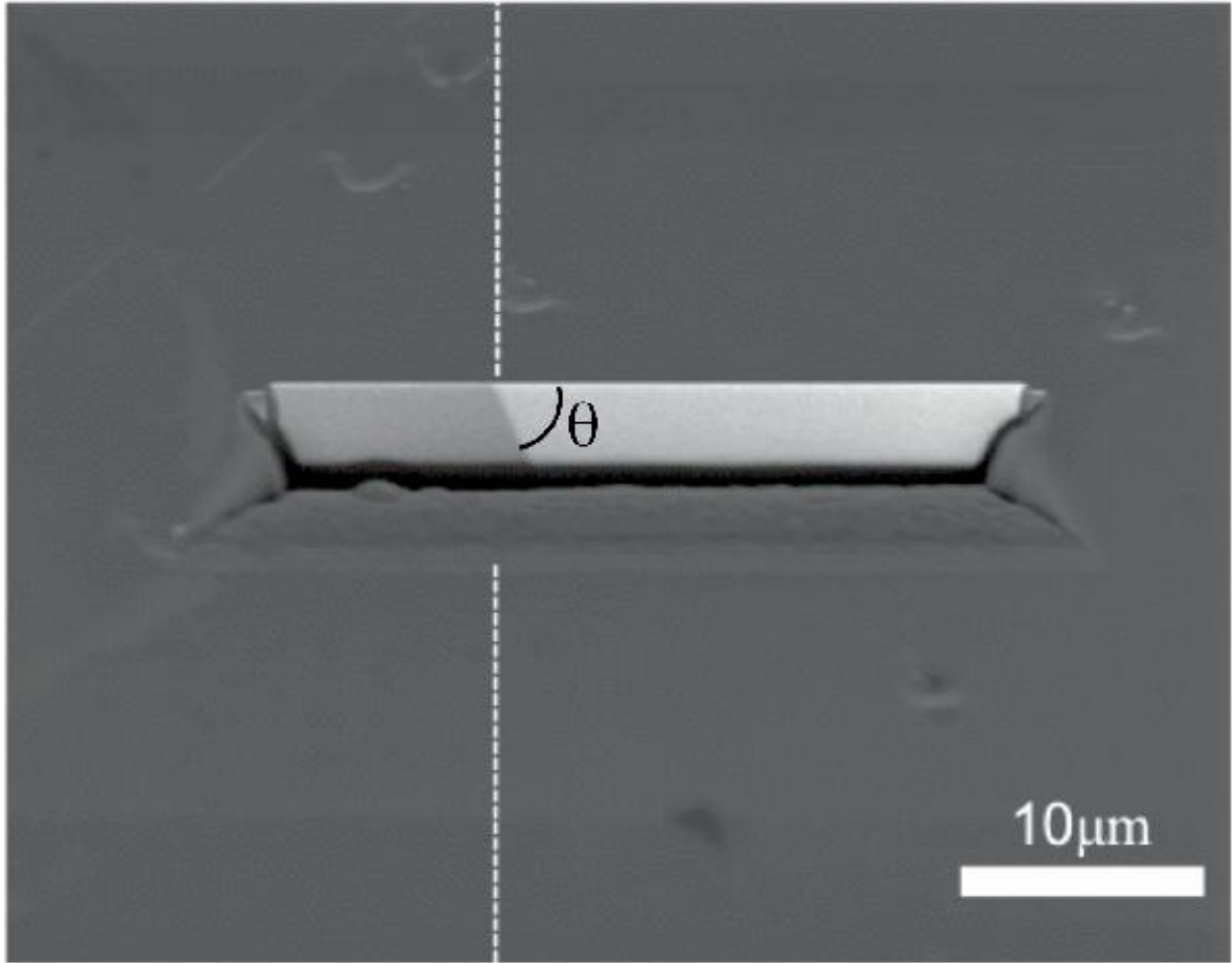


Figure. 2.4: Backscattered electron image showing a FIB cross-section cut used to determine the grain boundary inclination below the surface, where  $\theta$  is inclination angle measured from image and is used for the calculation of real grain boundary inclination using Eq. 2.1.

### 2.3.3 Atomic Force microscopy (AFM)

AFM is commonly used for measuring the surface topographies of the object at nano-scale. The AFM measurements in this work were carried out using a VEECO Dimension 3100 (VEECO Instruments Inc. Plainview, NY, USA). The precision of this equipment on the Z axis (height) is around 0.1 nm, while being ~1nm on the two lateral axis. The AFM probes used were TESP etched silicon probes (Bruker, Billerica, Massachusetts, USA). All AFM scans were conducted in tapping mode. Under this mode, the surface damage from the AFM tip was minimized while the surface profiling still maintains highly accurate. The resolution of the AFM scans was chosen between 256x256 or 512x512, depending on the size of the scan area. Post-processing of the AFM scan was finished with the Gwyddion software package<sup>2</sup>.

### 2.3.4 Nanoindentation

Nanoindentations were conducted only on sample A using a Hysitron TriboScope 900 (Minneapolis, MN, USA) nanoindenter equipped with a 1.4  $\mu\text{m}$  sphero-conical diamond tip indenter. All indentations were performed in load-controlled mode. A maximum load of 6 mN was used with a load-hold-unload profile of 5 seconds for each segment. An array of indents (31 by 31) was placed at the area of interest on sample A. The indents in the array were spaced by 20  $\mu\text{m}$  vertically and 30  $\mu\text{m}$  horizontally. An SEM image of the indentation array was shown in Fig. 2.5. Another round of nanoindentations were placed within the array of the indents while at varying distances from 9 selected grain boundaries of interest. An example of the indentations in the grain boundary vicinity is shown in Fig. 2.6. The surface topographies of selected nanoindents were measured using AFM.

---

<sup>2</sup> Gwyddion is a free software for visualization and analysis of scanning probe microscopy such as AFM.

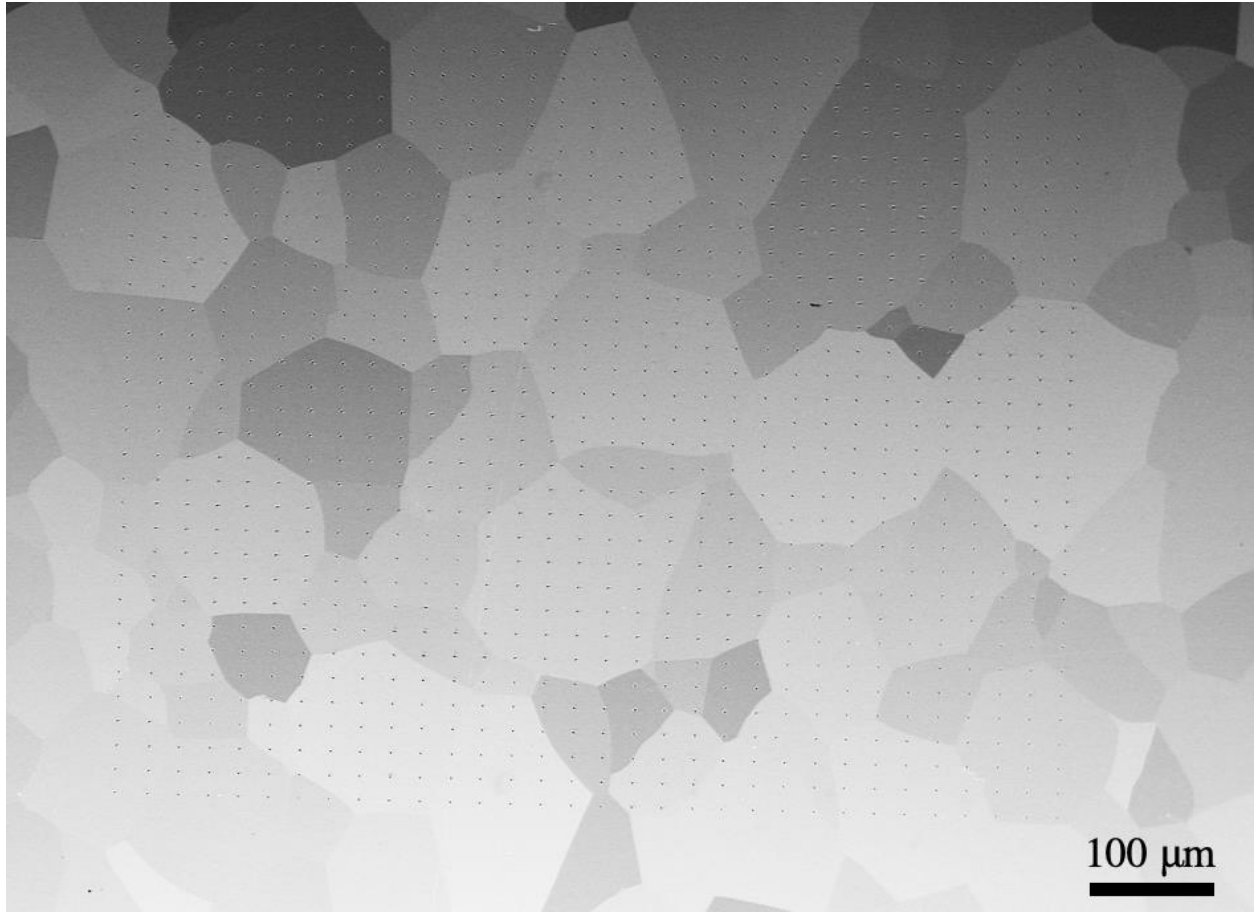


Figure 2.5: An SEM image of the region that contains the grid of nanoindentations (shown as black dots) in material A.

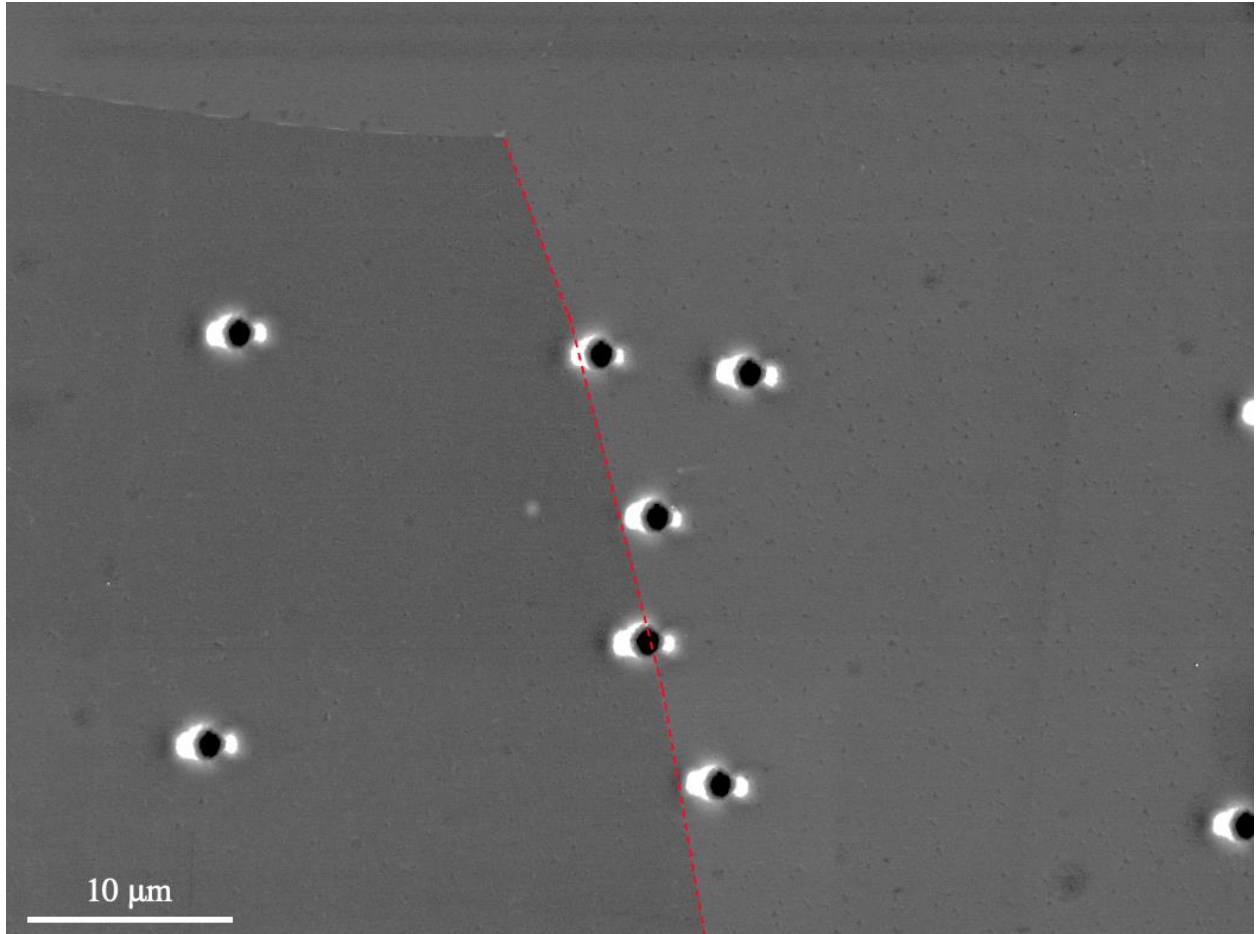


Figure 2.6: An SEM image of bi-crystal nanoindentations near a selected grain boundary with varying distances from the boundary in material A. The investigated grain boundary is colored in red dash line.

### 2.3.5 Four-point bending

Four-point bending was selected to be the method to deform Sample B, because it generates maximum tensile stress states on the sample surface between the two inner pins while eliminating the triaxial stress states present in the uniaxial tensile tests. In addition, the plastic strain of on the sample surface between the two inner pins are roughly uniform according to the finite element simulation of four-point bending J. Seal [123]. The bending stage used in this work is shown in Fig. 2.7. The two outer and inner pins of the stage are 20 mm and 5 mm apart, respectively.

Sample B was carefully strained to ~1.5%. The low magnitude of strain maintains a flat sample surface. In addition, the low density of slip traces under low strain limited the occurrence of cross-slip which is not the focus of this study. Characterization of the sample surface was concentrated only in the regions between two inner pins. SEM imaging and EBSD scans of the area of interest was conducted both before and after deformation. Surface profiles of the slip traces at selected grain boundaries was characterized using AFM.

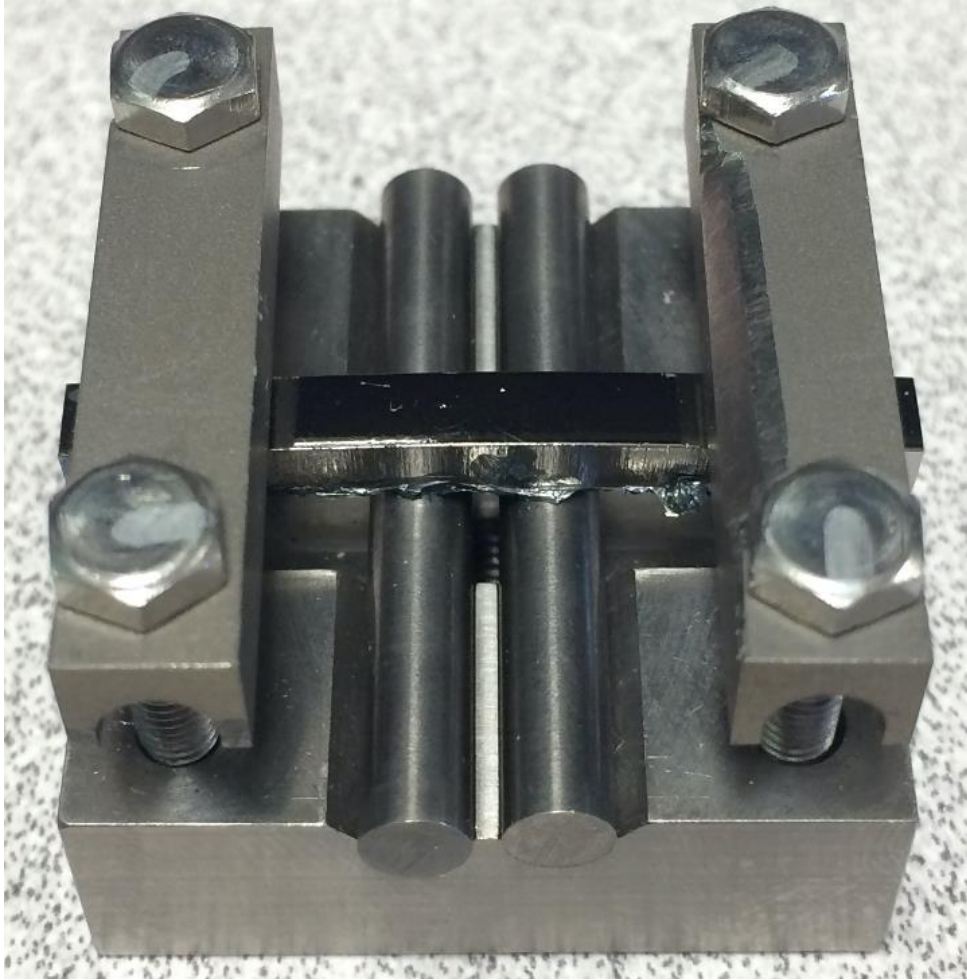


Figure 2.7: The picture of the four point stage with the sample.

## 2.4 Slip trace analysis

Slip trace analysis used an algorithm that allows the determination of slip plane, and in certain cases even Burgers vector associated with the slip band observed in experiment. An example slip trace analysis is shown in Fig. 2.8a, where the major slip traces can be observed sharing a common direction that goes from the lower left to upper right. To identify the slip system associated with these slip lines, the orientation of the unit cell is determined (the hexagonal structure with black edges) using the Euler's angle measured from the EBSD. With the known orientation of the unit cell, directions of the slip traces formed by all 24 potential slip systems are determined. By matching the observed slip trace with each of the 24 calculated slip traces, one can decide which slip system is the active one. In the case shown in Fig 2.8a, the slip lines of the prismatic  $\langle a \rangle$  slip system (the grey slip plane with the white Burgers vector on the unit cell) agrees perfectly with AFM measured slip lines.

In some special cases where more than one slip systems can produce slip traces that agree well with the observations, the inclination of the slip plane was used as a secondary criterion to determine which slip system is active. For example, in Fig. 2.8b and c, two slip lines from both slip planes (shaded in grey) agree well with the observation. Nonetheless, only the upper slip plane shares the same inclination as the AFM measured slip band.

In addition to resolving the active slip plane, the active Burgers vector can be determined if the slip occurs on prismatic and pyramidal plane where there is only one available Burgers vector. In the case of an active basal slip plane where there are three potential Burgers vector, the global Schmid factor needs to be calculated for each of the three slip systems. The Burgers vector with the highest global Schmid factor is chosen as the active slip system.

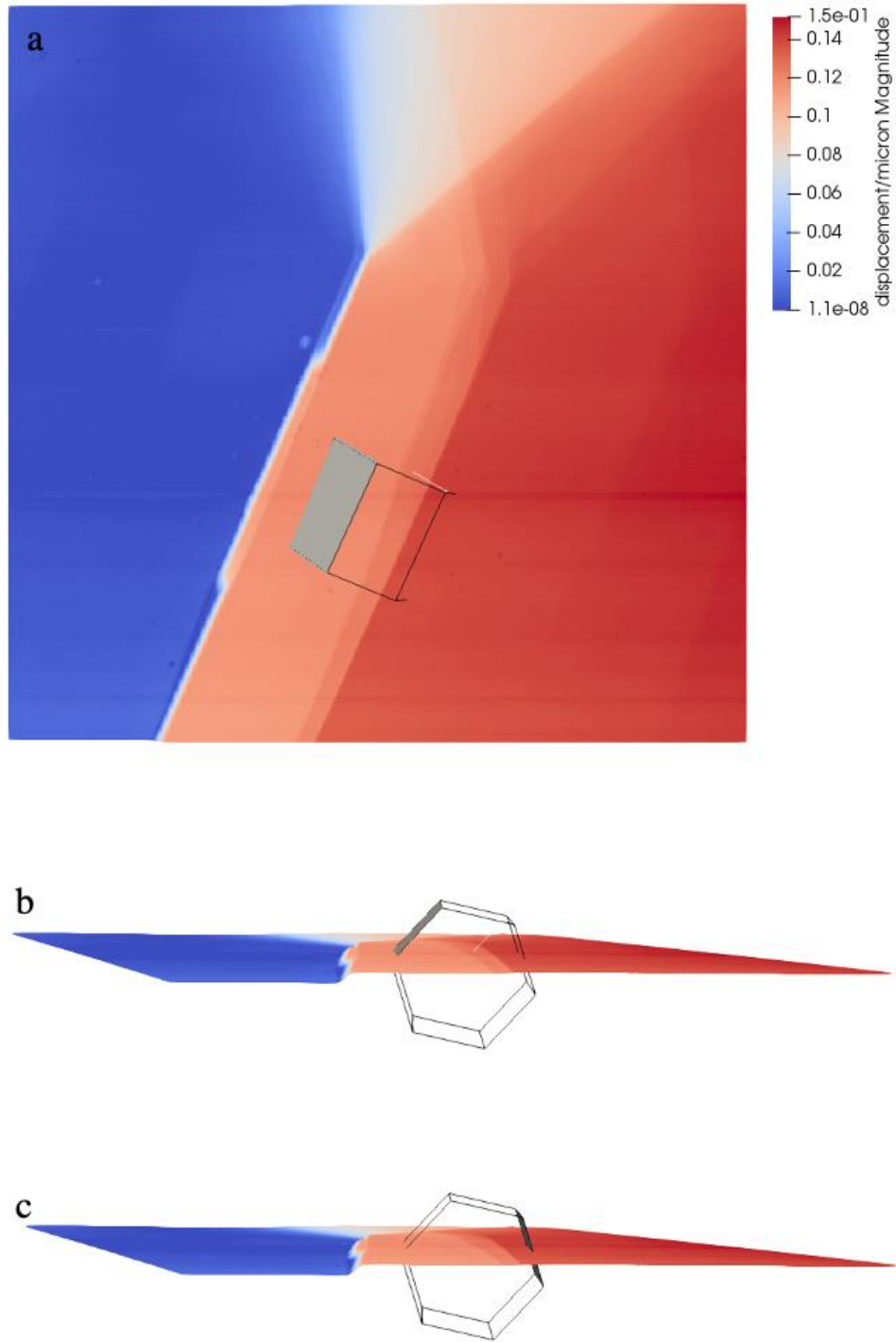


Figure 2.8: The AFM measured surface profile of a slip trace (blue suggests lower heights) overlaid with a unit cell of the corresponding grain orientation shown in top view (a) and side view (b, c). The assumed active slip plane in the slip trace analysis is colored in grey in the unit cell.

## 2.5 Constitutive law in Crystal Plasticity Finite Element Method (CPFEM)

The CPFEM formulation used in the present study is based on previous work of Kalidindi *et al.* [124]. Models were built to simulate both the loading and unloading segment of the nanoindentations. All simulations in this work adopted a finite strain framework of elastoplasticity with a multiplicative decomposition of deformation gradient  $\mathbf{F}$  into an elastic (including rigid-body rotation) and plastic part:

$$\mathbf{F} = \mathbf{F}_e \mathbf{F}_p \quad \text{Eq. 2.2}$$

The second Piola-Kirchhoff stress  $\mathbf{S}$ , acting in the intermediate configuration, is the product of elastic Green's Lagrangian strain  $\mathbf{E}_e$  and fourth-order stiffness tensor  $\mathbb{C}$  as:

$$\mathbf{S} = \mathbb{C} \mathbf{E}_e = \frac{1}{2} \mathbb{C} (\mathbf{F}_e^T \mathbf{F}_e - \mathbf{I}) \quad \text{Eq. 2.3}$$

The evolution of the plastic deformation gradient is connected to the plastic velocity gradient  $\mathbf{L}_p$  through:

$$\dot{\mathbf{F}}_p = \mathbf{L}_p \mathbf{F}_p \quad \text{Eq. 2.4}$$

Plastic deformation is restricted to shear on defined slip systems, which means the plastic velocity gradient can be assembled from shear rates on every slip system by:

$$\mathbf{L}_p = \dot{\mathbf{F}}_p \mathbf{F}_p^{-1} = \dot{\gamma}^\alpha \mathbf{d}^\alpha \otimes \mathbf{n}^\alpha \quad \text{Eq. 2.5}$$

The shear rate  $\dot{\gamma}^\alpha$  on slip system  $\alpha$  is expressed in terms of resolved shear stress,  $\tau^\alpha$ , and the critical resolved shear stress,  $\tau_{\text{cr}}^\alpha$ :

$$\dot{\gamma}^\alpha = \dot{\gamma}_0 \left| \frac{\tau^\alpha}{\tau_{\text{cr}}^\alpha} \right|^{\frac{1}{m}} \text{sign}(\tau^\alpha) \quad \text{Eq. 2.6}$$

where  $\dot{\gamma}_0$  and  $m$  are material parameters. The  $\tau_{\text{cr}}^\alpha$  evolve with shear on other slip systems  $\beta$  according to:

$$d\tau_{\text{cr}}^\alpha = \sum_\beta h^{\alpha\beta} |d\gamma^\beta|, \quad h^{\alpha\beta} = q^{\alpha\beta} h^\beta \quad \text{Eq. 2.7}$$

The hardening matrix,  $h^{\alpha\beta}$ , is composed of the self-hardening,  $h^\beta$ , and the cross-hardening matrix,  $q^{\alpha\beta}$ . The self-hardening,  $h^\beta$ , is calculated by:

$$h^\beta = h_0^\beta \left(1 - \frac{\tau_{cf}^\beta}{\tau_s^\beta}\right)^a \quad \text{Eq. 2.8}$$

where  $h_0^\beta$  and  $a$  are, respectively, the initial hardening slope and hardening exponent, which affects the shape of the self-hardening curve. The diagonal elements of cross-hardening matrix,  $q^{\alpha\beta}$ , are all assigned to unity, while off-diagonal elements are taken as 1.4.

## CHAPTER 3 STUDY OF SLIP TRANSFER USING NANOINDENTATION AND CRYSTAL PLASTICITY MODELING

In this chapter, a novel approach to studying the interaction between slip and grain boundaries using bi-crystal nanoindentation is outlined. Previous research has tried to approach this problem by quantifying the differences in the nano-hardness, load-displacement curves between nanoindents in grain interiors and near the grain boundary. In this study, the influence of grain boundary on the formation of surface topographies of nanoindentations<sup>3</sup> in the boundary vicinity compared to those in grain interior was observed. Such influence is found to be strongly dependent on the character of the grain boundary. To understand how a grain boundary alters the development of nanoindent surface topographies, AFM measurements of surface topographies of indents both near and away from grain boundary were compared, the differences were quantified using a new metric: the volume of each indent surface topography. In addition, the differences between single and bi-crystal indentation were related to slip transfer criterion such as  $m'$  and  $M$  (LRB criterion). To further obtain the stress, strain, and shear of individual slip system under both single and bi-crystal indentations, CPFEM models were built for the two conditions using the Matlab toolbox Stabix developed by D. Mercier *et al.* [125]. The model successfully captured the surface topographies of all single crystal and most of the bi-crystal nanoindentations. For some high angle grain boundaries, the accuracy of the model decreases notably. Discussion of the discrepancies between observations and simulations suggest that the cause might be several underlying assumptions of CPFEM. (This work has been published. [126])

---

<sup>3</sup> Previous work on the formation of surface topographies in single crystal nanoindentations were carried out in pure copper,  $\gamma$ -TiAl, and commercially pure  $\alpha$ -Ti. [2002 copper, two Claudio's papers]

### 3.1 Overview of the locations of nanoindentations

A sample with large grain size (around 130  $\mu\text{m}$ ) was used for this study. An overview map of the microstructure of the indented region is shown in Figure 2.4. Nanoindentations away from the grain boundary<sup>4</sup> in this region were deemed as single crystal nanoindentations as the indent is not influenced by any grain boundary. In addition, indents in the vicinity of grain boundary<sup>5</sup> were treated as bi-crystal nanoindentations. Both bi-crystal and corresponding single crystal nanoindentations were placed near 6 different grain boundaries and inside 12 grains that shared those 6 boundaries. Figure 3.1 gives an overview map of all the nanoindents studied in this chapter. As a result of the difficulty of controlling the distance between the location of the indent and the grain boundary, multiple nanoindents were present at each grain boundary with only a fraction of them ending up close to the boundary. Only those nanoindents that are influenced by the grain boundary were treated as bi-crystal nanoindents.

---

<sup>4</sup> An indent located beyond 10  $\mu\text{m}$  from the grain boundary is generally considered a single crystal indent.

<sup>5</sup> An indent within 2  $\mu\text{m}$  distance from the grain boundary is considered a bi-crystal indent.

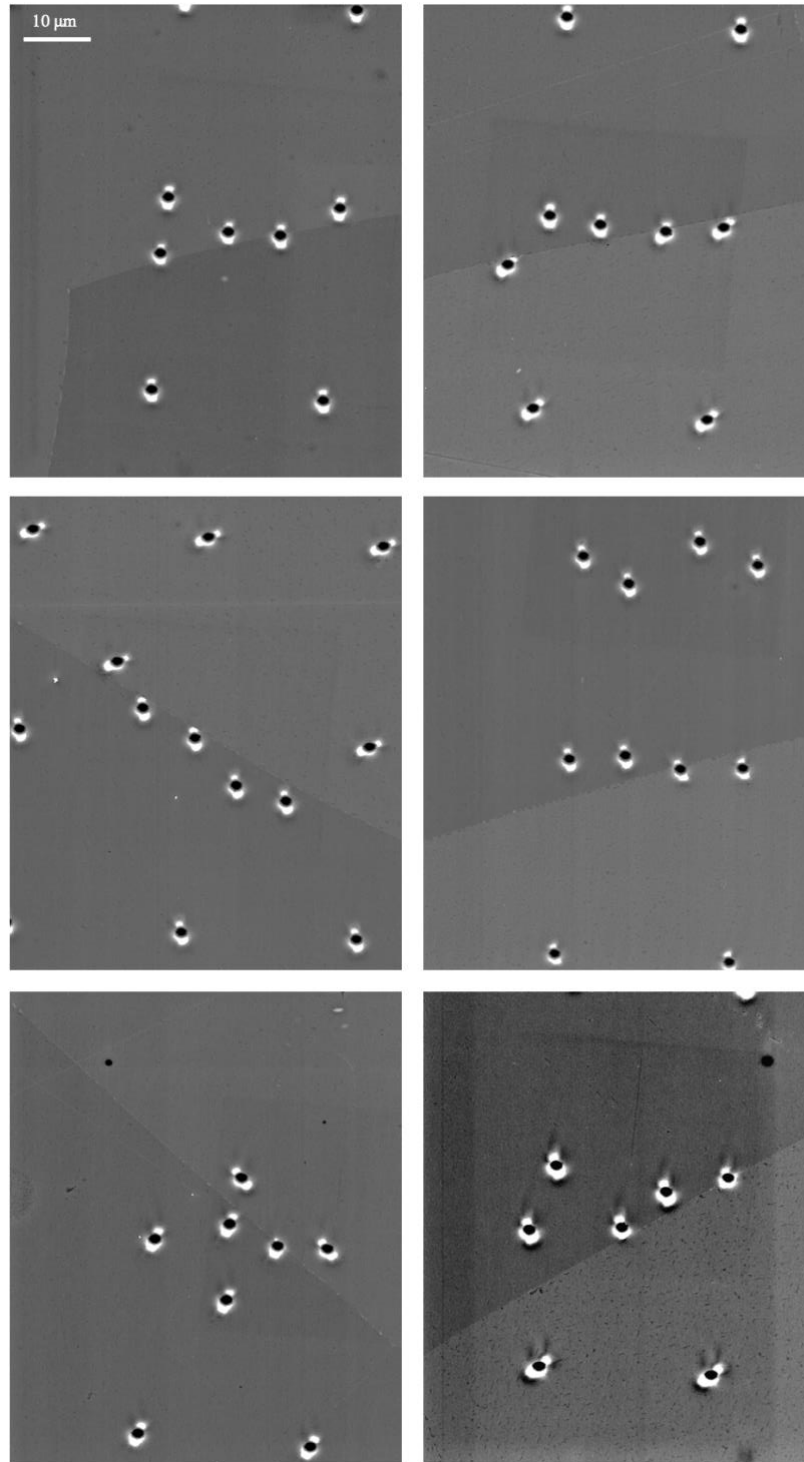


Figure 3.1: SEM images of bi-crystal nanoindents near the six selected grain boundaries and the corresponding single crystal indents in the two adjacent grains.

### 3.2 Nanoindentation load-displacement curves

For single crystal indentation, the maximum indentation depths ranged from 250 nm to 300 nm, reflecting material property, such as nano-hardness, variations in different grain orientations. Nevertheless, load-displacement curves for nanoindents within the same grain are highly reproducible, with variations in both load and maximum displacements of less than 1%. The load-displacement curves for single crystal indents and the corresponding bi-crystal indents are sometimes notably different. An example of this comparison is shown in Fig. 3.2, where the indentation load-displacement curves show slightly enhanced hardening for indents placed near grain boundaries. This is evident in the slightly larger slope of the bi-crystal indent under the condition that the same load profile was used. The curves also indicate that forward creep occurs during holding at peak load. This is consistent with observations of stress relaxation and creep at ambient temperature in  $\alpha$ -Ti ([127-131]).

In only four of the nine grain boundaries studied, displacement jumps of 5nm to 15 nm were observed, an example of which is shown in Fig. 3.2. For those bi-crystal nanoindents that did not cause displacement jumps on the load displacement curves, no verified answer can be provided. One possible explanation is the uncertainty of the distribution of defects on the grain boundary, which can lead to the random formation of displacement jumps in any bi-crystal nanoindentation.

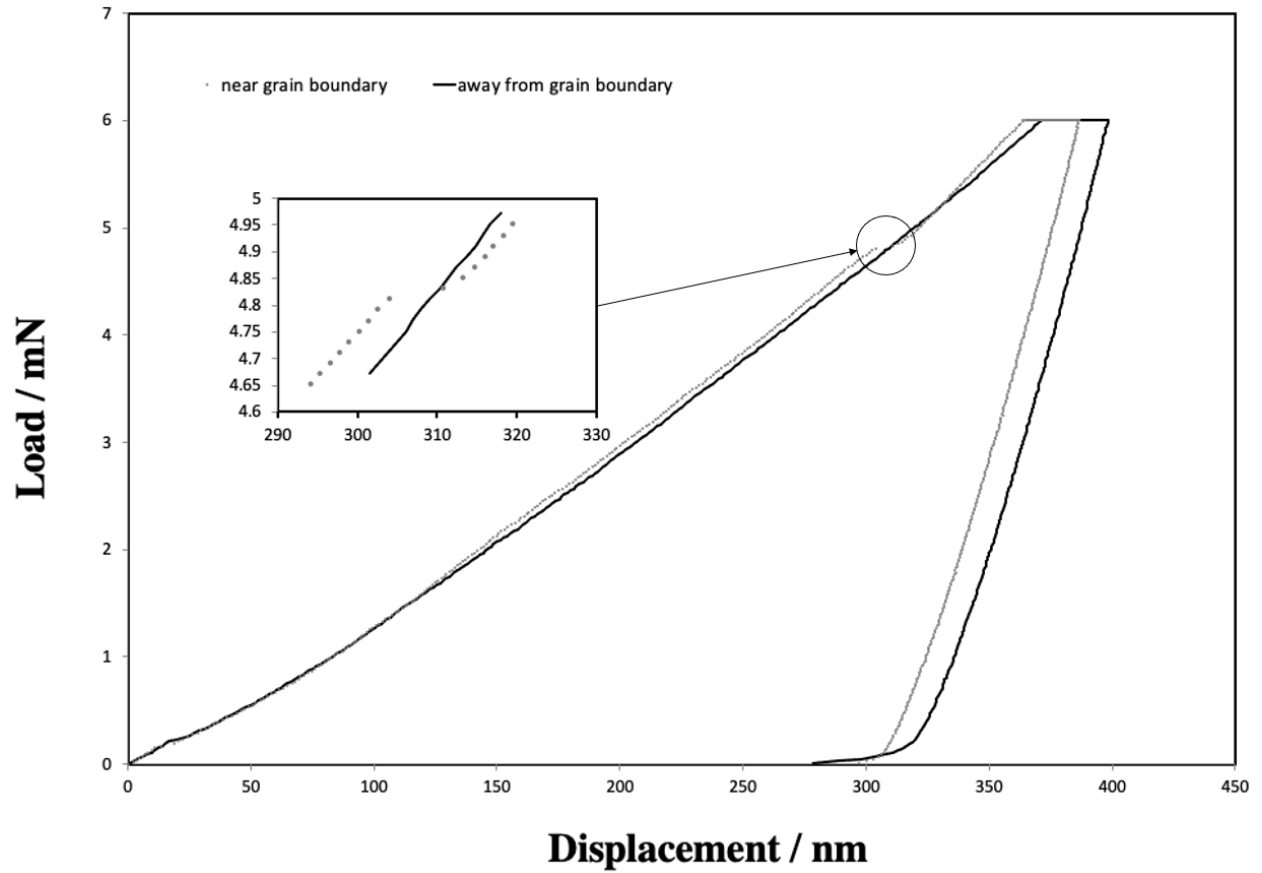


Figure 3.2: Load-displacement curve of a bi-crystal indent (shown as the grey dotted line) and the corresponding single crystal indent in the originating grain (shown as the black solid line). A magnified inset is used to show the displacement jump occurred in the bi-crystal indentation.

### 3.3 Differences of the topographies formed in single and bi-crystal nanoindentations

#### 3.3.1 Quantifying the volume difference of two indent topographies

As both the AFM measurement of indent topographies and the simulation results are pixelated data, it is essential to establish a point-to-point comparison to quantify the differences between indent topographies, so that the comparisons are carried out in a systematic manner.

Thus, the volume difference,  $\Delta V_{a,b}^{(A)}$ , between two indentation topographies  $a$  and  $b$  within a grain interior, as shown in Fig. 3.3, is defined as the integral of the absolute value of the height difference using equation:

$$\Delta V_{a,b}^{(A)} = \int |h_a(r, \theta) - h_b(r, \theta)| dA \approx \sum_{(x,y) \in A} |h_a(x, y) - h_b(x, y)| \Delta x \Delta y \quad \text{Eq. 3.1}$$

where  $h_a(r, \theta)$  and  $h_a(x, y)$  is the height at corresponding points with the coordinate of either  $x = (r, \theta)$  of a radial coordinate system or  $x = (x, y)$  of a Cartesian coordinate system, over the relevant area of interest  $A$ . In addition, the (absolute) volume of an indent topography  $a$  is, similarly, defined as:

$$\Delta V_a^{(A)} = \int |h_a(r, \theta)| dA \approx \sum_{(x,y) \in A} |h_a(x, y)| \Delta x \Delta y \quad \text{Eq. 3.2}$$

There are two major reasons for using volume differences as a measure to compare indentation topographies. The volume of an indentation topographies is an indication of the amount of plastic strain the indentation has generated. As a result, it facilitates our study of the interaction between plastic deformation and grain boundary. The other reason of using volume representation is due to its simplicity and intuitive for visualization.

### 3.3.2 Reproducibility of nanoindentation topographies

The subsequent interpretation of bi-crystal indentation topographies on or close to grain boundaries relies on comparisons to corresponding single crystal indent topographies. To ensure that such comparisons are meaningful, the reproducibility of the indent topography needs to be established. To assess this, the absolute height difference between corresponding points  $x = (r, \theta) = (x, y)$  of two indent topographies a and b is summed using eq.3.1, as illustrated in fig. 3.3a and b (The AFM data of indent topographies a and b in 3D are shown in appendix A.). The resulting  $\Delta V_a^{(A)}$  determined by radial integration over the ring region  $A = \pi(r_{\text{out}}^2 - r_{\text{in}}^2)$  with varying  $r_{\text{out}}$  is plotted as a function of A shown in Fig. 3.3c, where  $r_{\text{in}}$  is the approximate indentation impression radius. In Fig. 3.3c, two distinct slopes are found. Within the area influenced by the indentation plastic deformation zone that is about three times the indent diameter [81], about  $16 \mu\text{m}^2$  for this example, a high slope is found. At large areas beyond the influence of the indent, a low slope is observed that represents the random mismatch between the two topographies due to surface roughness (and AFM noise). The high slope in smaller areas can be attributed to actual differences in the two indentation topographies (a and b). Thus, a measure of reproducibility of indent topography can be defined by the difference between these two slopes that corresponds to an average height difference between two topographies in excess of unavoidable surface roughness and measurement noise.

This methodology was applied to nominally identical indentation pairs in eight single crystal orientations and two bi-crystal situations to assess their individual reproducibility. Fig. 3.3d shows a plot of the cumulative probability of surface roughness (dotted line) and topography reproducibility (solid line) for the bi-crystal and single crystal indents. For both single and bi-crystal indents the surface roughness is very similar and falls between 1 nm to 3 nm, with two

outliers of exceptionally low roughness around 0.2 nm. The reproducibility of single crystal indent topography (black solid line) ranges between about 1 nm to 2 nm and is slightly better than the reproducibility observed for the two bi-crystals (grey solid line). Comparisons between the two pairs of bi-crystal indents are somewhat more problematic due to the inability to accurately control the distance of the indent from the grain boundaries, resulting in differences in the distance from the grain boundaries being  $\Delta d = 0.02 \mu\text{m}$  and  $0.44 \mu\text{m}$  in the two cases. Nevertheless, the reproducibility of bi-crystal indent topography is only slightly worse than that of the single crystal topographies, at approximately 3 nm. Overall, the reproducibility of 2 nm to 3 nm compares very favorably to the overall indent pile-up heights that range from approximately 130 nm to 180 nm, and thus establishes a base noise level for comparison of topographies of indentations carried out under different conditions.

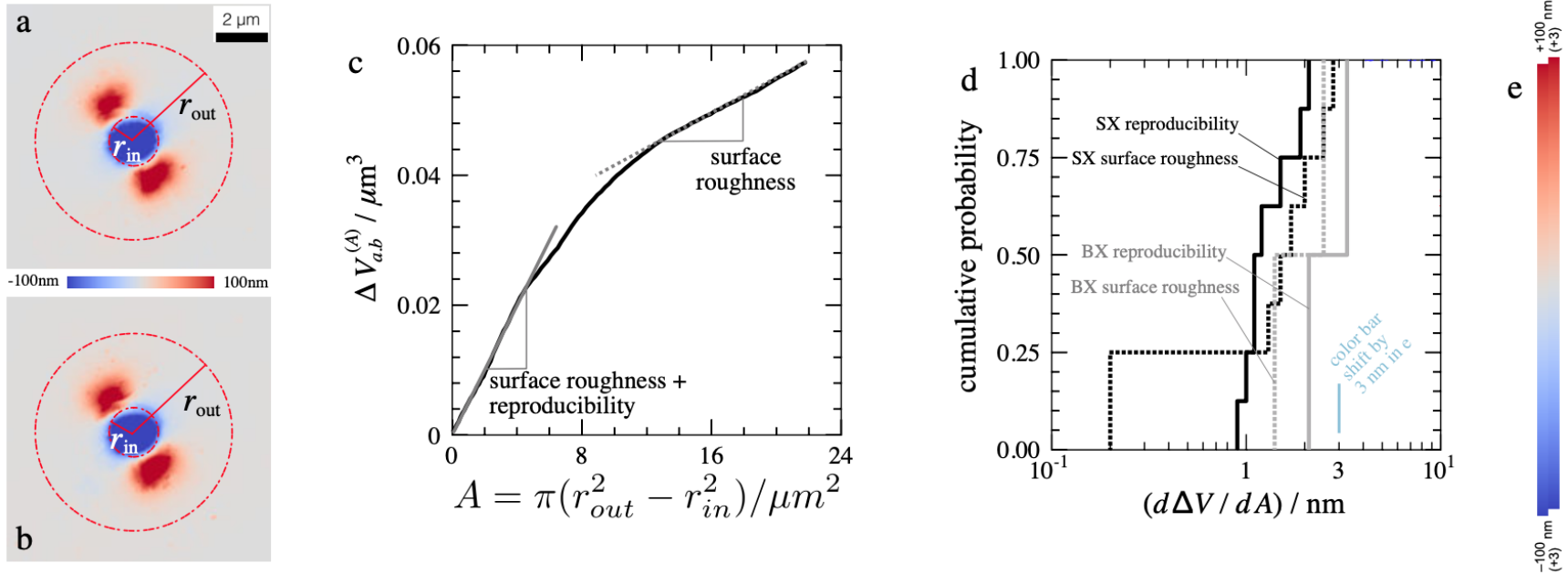


Figure 3.3: a,b): Example of two single crystal nanoindents from the same grain used for establishing the reproducibility and surface roughness of nominally identical nanoindentations, where  $r_{in}$  and  $r_{out}$  are the inner and outer radius of a ring centered on the indent and isolating the major indent topography features. c): Correlation between  $\Delta V$  (short for  $\Delta V_{SX.SX}^{ring}$  or  $\Delta V_{BX.BX}^{ring}$ , calculated based on Eq. 3.1) and ring area  $A$ . d): Cumulative probability of the surface roughness levels (dotted), established from the slope of the dotted line in (c), and reproducibility (solid) of single and bi-crystal indentation, as determined by the difference between slopes of the solid and dotted lines in (c). A reproducibility better than 3 nm corresponds to negligibly small perceived differences, as demonstrated by shifting one part of the color bar by that amount (e). [126]

### **3.3.3 Comparing single crystal indent topographies with the corresponding bi-crystal indent topographies**

To effectively evaluate the influence of grain boundaries on the formation of indent topographies, indentations affected by grain boundaries were categorized into two groups: indents with part of the residual impression in both grains i.e., crossing the boundary, as shown in Fig. 3.4, and indents that were placed sufficiently close to a grain boundary such that only their topographies were reached and/or exceeded the grain boundary, as exemplified in Fig. 3.5. In both cases, indentations are expected to involve a number of processes, including slip transfer across the boundary, grain boundary deflection of dislocations due to differences in the elastic behavior of the two grains, and shifting of the boundary from its original location.

*Indents located on the grain boundaries.* The surface topographies of the three indents that fall across grain boundaries, along with the corresponding single crystal indents from both sides of the grain boundary, are shown in Fig. 3.4. In these cases, indentation topographies have developed on both sides of the grain boundaries. The location of those indent topographies are for the most part consistent with the corresponding single crystal topography of the grain on the respective sides of the boundaries. Nevertheless, the sizes of these indent topographies are typically smaller than those of the corresponding single crystal indents. In general, slip transfer across the grain boundary is not a dominant feature for this category of indents.

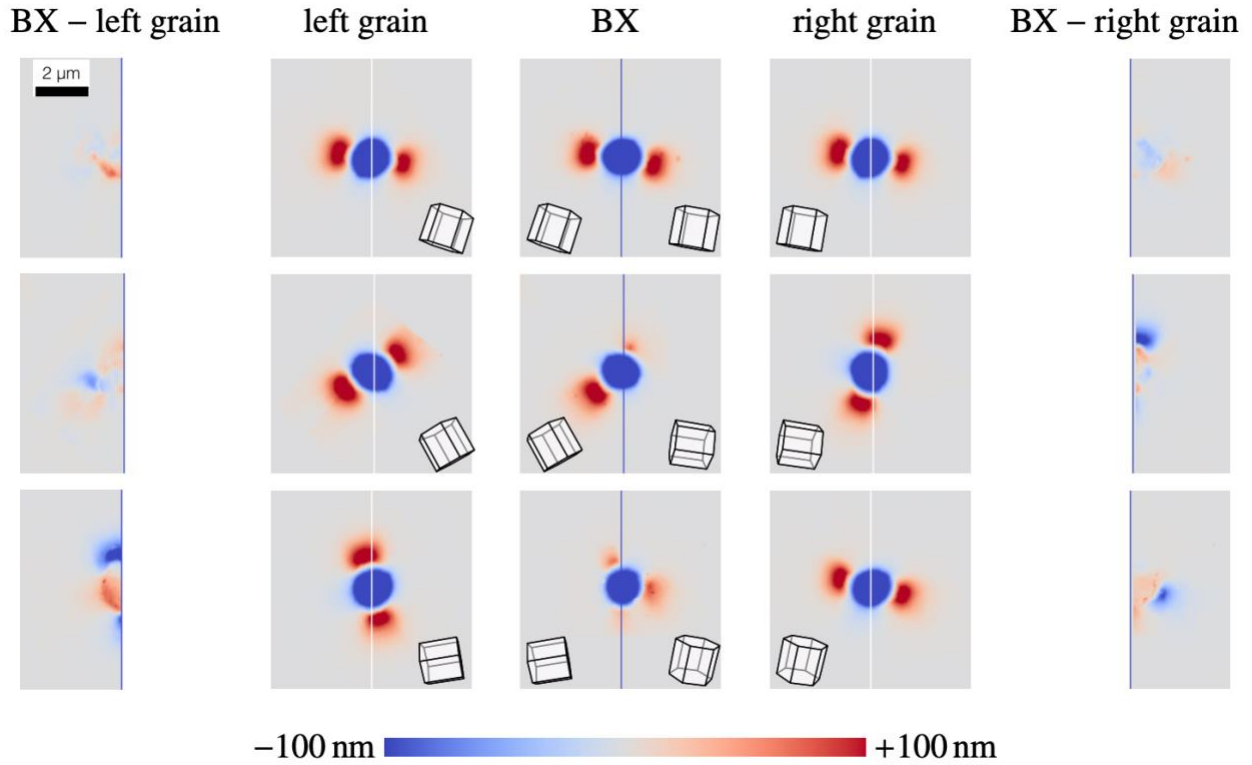


Figure 3.4: Nanoindent topographies developed when the indents impression falls across grain boundaries (center column), in comparison to corresponding single crystal indent topographies from both sides of the grain boundaries (second and fourth columns). The differences between the single and bi-crystal indents are mapped for the left grain and the right grain (first and last column).

*Indents near grain boundaries.* When indents were located entirely in one grain with only the indent topography reaching the grain boundary, the indent topography was generally reproducible, but significant differences in indent topography were observed between different grain pairs or for different boundary orientations between the same pair (Fig. 3.5). This suggests that the nature of the boundaries directly influences the indent topographies, and allows the indent topography to be used to study how strain is accommodated at and transferred across different boundaries.

Nine indent topographies close to six grain boundaries with different  $m'$  values<sup>6</sup> are compared in Fig. 3.5. Two of these, with  $m' = 0.62$ , show indents on either side of the same grain boundary. Two other pairs, for grain boundaries with  $m' = 0.98$  and  $0.56$ , each show two indents taken from the same side of the boundary. Circular areas, which are consistent with the observed indent impressions, have been used to mask the subsurface portion of the indents in Fig. 3.5, such that only the relevant indent topographies are assessed. Dark vertical lines mark the grain boundaries for bi-crystal indents while white lines indicate the corresponding position for single crystal indents (Note that the white lines are only fiducial lines used to facilitate the comparison between the corresponding regions between bi-crystal and single crystal indents). Bi-crystal indent topographies are shown in the central column, with the corresponding  $m'$  values shown in the upper right corner of each of these figures. The corresponding single crystal indent topographies collected from the grains to the left and right of the grain boundaries are shown in the two columns immediately to the left and right (second and fourth). The differences between

---

<sup>6</sup> In the present study, a more involved method of determining the  $m'$  was carried out through 3 steps: 1. Slip systems of both the originating and the receiving grain were ranked according to the accumulated shear calculated in simulation; 2. The most active slip systems on each side and in the vicinity of the grain boundary were picked for the calculation of the  $m'$ ; 3. If two systems had similar accumulated slip near the grain boundary, the one that rendered a higher  $m'$  was chosen.

the topographies of the bi-crystal indents and corresponding single crystal indents are mapped in columns 1 and 5. Positive and negative height differences are colored red and blue, respectively, to indicate a bi-crystal topography is higher or lower than the corresponding single crystal topography.

Under constant indentation load (6 mN), the resulting bi-crystal indentation impression depths ( $h$  in Fig. 3.5) were consistently less than the corresponding single crystal indents, reflecting the deformation resistance associated with the grain boundaries. In response to the presence of a grain boundary, the height of the resulting pile-ups in the originating grain may either increase or decrease. This is illustrated by column 1 in Fig. 3.5, which shows that difference plots may be either red or blue in the originating grain (left of grain boundary). In many cases in column 1, the bi-crystal indentation leads to higher topography (red) very close to the indent, perhaps indicating more resistance to plasticity as a result of the grain boundaries. This is particularly evident in grain boundaries with higher slip system misorientation, as indicated by lower  $m'$  (arranged from top to bottom).

The indent topography heights in the receiving grain of a bi-crystal indent are typically different from the heights in either of the two corresponding single crystal indents, but the locations of the topographies in the bi-crystal indents can always be associated with topography locations in at least one of the single crystal indents (Fig. 3.5 column 3 compared to columns 2 and 4). Upon initial inspection, it appears that these heights may simply be either higher or lower than the corresponding single crystal indent topographies (Fig. 3.5 columns 1 and 5), however, more details were found in more specific observations. That is, the bi-crystal indent topography in the receiving grain is always lower (indicated by blue in column 5) than the corresponding single crystal topography for that receiving grain (i.e., comparing the blue

location in Fig. 3.5 column 5 to the topography in column 4). Nevertheless, these same receiving grains often show areas of higher topography (indicated by red in column 5) that correspond to the indent topography of the respective originating single crystal grain in that area (topography locations in column 2). Similar observation can be made regarding the receiving grain in column 1 of Fig. 3.5. These topography differences are likely caused by the change in the stress field and/or by the change of the slip kinematics due to the different lattice orientation.

In the following, how the differences in indent topography can be correlated to grain boundary nature, as indicated by  $m'$ , are rationalized. The top two rows of Fig. 3.5 show an example of a boundary that does not have a strong influence on the indent topography development. The topographies of the indentations in both the originating and receiving grains do not appear to be restricted by the low-angle grain boundary, and a significant amount of indent topography has developed in both originating and receiving grain. This is consistent with the excellent alignment of all of the slip systems across the grain boundary, as indicated by the high  $m'$  value of 0.98. At the other extreme, as shown in the bottom row of Fig. 3.5, the formation of a indent topography in the originating grain next to the grain boundary is reduced due to its high-angle character, indicated by an  $m'$  of 0.51. The seventh and eighth rows in Fig. 3.5 show another high-angle grain boundary, with an  $m'$  value of 0.56, where two indents are located at the same distance from the grain boundary. In this case, both indents show virtually identical indent topography, both of which are strongly inhibited by the grain boundary, with only limited pile-up “spilling into” the receiving grain. Indents near another high-angle grain boundary, with  $m'$  being 0.62, are displayed in rows four and five. Here, the slip systems are somewhat more aligned, and the indent topography transferred into the receiving grain is moderately larger. It is worth noting that the two indents near this high-angle grain boundary are

on opposite sides of the same boundary. The limited indent topography transfer in both directions suggests that strain transfer is difficult at a high-angle boundary regardless of the directionality. Overall, it is clear that the indent topography development in the receiving grain is strongly affected by the slip system alignment on both sides of a grain boundary. This analysis also indicates that the relative magnitude of the grain boundary resistance to slip can be assessed using the quantitative comparison between single and bi-crystal indent topographies illustrated in Fig. 3.5.

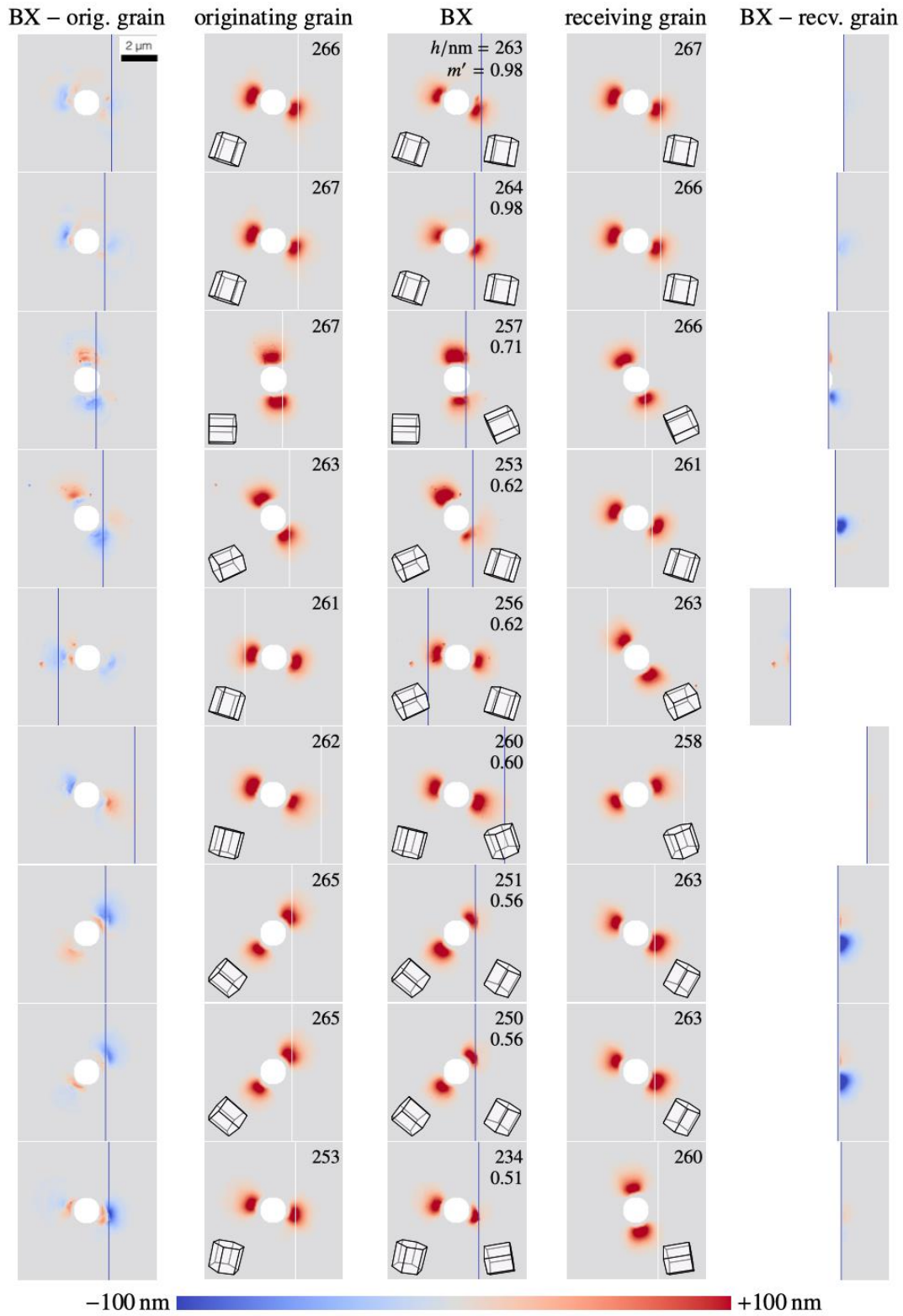


Figure 3.5: Nine bi-crystal indents (center column) collected near six different grain boundaries (blue lines) compared with corresponding single crystal indents in both the originating grains

Figure 3.5 (cont'd) (second column) and receiving grains (fourth column). Both single and bi-crystal indentation impression depths ( $h$ ) are labeled near the indents, and the  $m'$  of the six grain boundaries are listed in the image of bi-crystal indent in decreasing order. Indent topography differences caused by the grain boundary are mapped in the outermost columns as the difference between grain boundary indent and single crystal indent. The central indent valleys have been removed in order to enhance visualization of the indent pile-ups around the valleys. [126]

### **3.4 Simulations of single and bi-crystal nanoindentations using CPFEM**

#### **3.4.1 Computer-assisted processing of experimental data and automatic conversion into simulation files**

A number of computational crystallographic codes were integrated into several graphical user interfaces (GUIs) to support processing and analysis of the experimental data [125]. These data processing tools were crucial for minimizing possible sources of error in the numerous crystallographic calculations.

The first of the modules was developed to analyze the lattice alignment of grain pairs based on orientations collected through EBSD and associated grain boundary networks. Evaluation based on different slip transfer parameters such as the maximum value of  $m'$  was carried out with no stress state imposed, and the resulting parameters were displayed on grain boundary maps, as shown in Fig. 3.6 (left). A second GUI was used to visualize slip system relationships across a grain boundary (see Fig. 3.6 (middle)). A third GUI (see Fig. 3.6 (right)) converted the bi-crystal geometry, including grain boundary inclination, and grain orientations into a finite element mesh and produced the associated input files for direct simulation of the grain boundary indentation process.

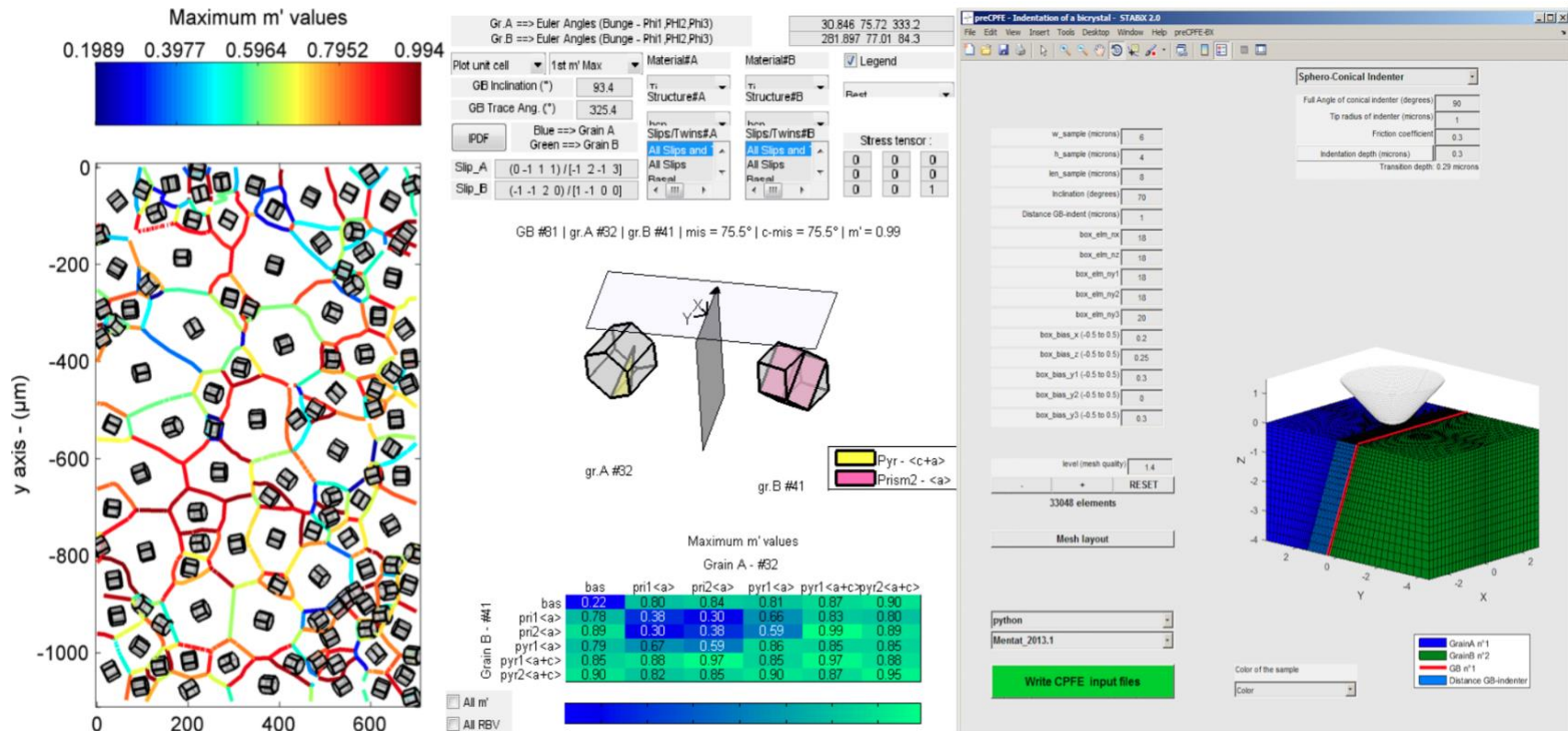


Figure 3.6: The GUI of Stabix used for generating simulation input files by using grain orientation data from EBSD.

Left image: EBSD crystallographic orientation data was first processed using the left GUI to determine the maximum  $m'$  parameter and to color the associated grain boundary. The hexagonal cells represent the orientations of each of the grains. Although the simulations include basal  $\langle a \rangle$ , prismatic  $\langle a \rangle$ , and pyramidal  $\langle c + a \rangle$ , the GUI only includes basal  $\langle a \rangle$  and prismatic  $\langle a \rangle$  for  $m'$  calculation. Middle image: The second GUI was used to display the crystallographic and slip system relationships. In the upper part

Figure 3.6 (cont'd) of the figure, grain boundary information, such as Euler angles, the orientation of the grain boundary line, the inclination of the grain boundary plane, and the active slip systems, can be entered to study the slip transfer of a desired grain boundary. Specific  $m'$  (or  $M$ ) associated with each pair of slip systems are tabulated in lower part of the figure. Right image: Using the grain boundary information entered in the second GUI, the third GUI builds finite element meshes for bi-crystal indentation simulations. Sample dimensions, mesh resolution, indentation depth, and indenter tip geometry are required as input. [126]

### 3.4.2. Formulation of a constitutive model for $\alpha$ -Ti

The crystal plasticity formulation used here has been detailed in section 2.5 based on the work of Kalidindi *et al.* [124], and adapted to  $\alpha$ -Ti with hexagonal lattice structure having  $c/a = 1.57$ . The deformation process of  $\alpha$ -Ti was simulated with 18 active slip systems. Three prismatic  $\langle \mathbf{a} \rangle$  slip directions are defined to be the most active slip systems, followed by 3 basal  $\langle \mathbf{a} \rangle$  and 12 pyramidal  $\langle \mathbf{c} + \mathbf{a} \rangle$  slip systems. Twinning is not included in this model as it was not observed in the nanoindentation experiments in this study.

The elastic constants used in the model were  $c_{11} = 162.4$  GPa,  $c_{12} = 92.0$  GPa,  $c_{13} = 69.0$  GPa,  $c_{33} = 180.7$  GPa,  $c_{44} = 49.7$  GPa,  $c_{66} = 76.5$  GPa ([132]). The initial slip resistance,  $\tau_0$ , and saturation slip resistance,  $\tau_s$ , were identified via a single crystal optimization method described in the work of Zambaldi *et al.* [133], and are listed in Table 3.1. The material hardening parameters,  $h_0$  and  $a$ , were fixed at 0.2 GPa and 2.0, respectively. The stress exponent and reference shear rate,  $n$  and  $\dot{\gamma}_0$ , were chosen to be 20 and  $10^{-3} \text{ s}^{-1}$ , respectively

Table. 3.1: Material parameters used for simulating the  $\alpha$ -Ti. [133]

	$\tau_0$ /MPa	$\tau_s$ /MPa
Prismatic $\langle \mathbf{a} \rangle$	150	1502
Basal $\langle \mathbf{a} \rangle$	349	568
Pyramidal $\langle \mathbf{a} \rangle$	1107	3420

### 3.4.3. Three dimensional finite element simulation of indentation process

The crystal plasticity formulation was implemented into the commercial finite element solver MSC.Marc<sup>3</sup> using the HYPELA2 user subroutine. For single crystal indentation, the simulation process followed previous work of Zambaldi *et al.* [133].

To model the 3D nanoindentation deformation process near grain boundaries, bi-crystal specimen meshes (an example of the mesh was shown in Fig. 3.7) with about 40000 elements, depending on the indentation sample size, were generated using MSC.Mentat<sup>3</sup>. These meshes were developed using procedure files produced by the third GUI (Fig. 3.6 right), which uses the EBSD data and the FIB cross sectional measurements of grain boundary inclination. Meshing of the bi-crystal nanoindentation volumes was done so that the volume under the indenter and in the vicinity of the grain boundary was discretized by the smallest elements. The location of the nanoindentation was determined using the relative distance from the indent center to the grain boundary measured from the overlays of secondary electron images on AFM scans. The mesh size was adapted for simulations of different indents depending on the topographies produced by indentations, so that the influence of the mesh surface on indent topographies was minimized. Multiple simulations were carried out for the same experimental conditions of crystal orientation and indentation depth, but with a range of mesh sizes (from about 10,000 to 40,000 elements). The resulting simulated topographies were found to be insensitive to mesh size, with topographies varying by only a few percent (as determined by  $\Delta V$  defined in section 3.3.1 and 3.3.2). In the following sections, meshes with element numbers in the range of 30,000-40,000 elements were used as they result in smoother representation of indent topographies. Following previous studies, the spherical nanoindenter with a 1.4  $\mu\text{m}$  tip radius was modeled as a rigid body, and the friction coefficient between the indenter and metal was set to 0.3 [133]. The

indentation process was modeled using displacement control. The residual indentation impression depth of simulations was set to match that of the corresponding experiments in order to facilitate comparison between experimental and simulated indentation topography.

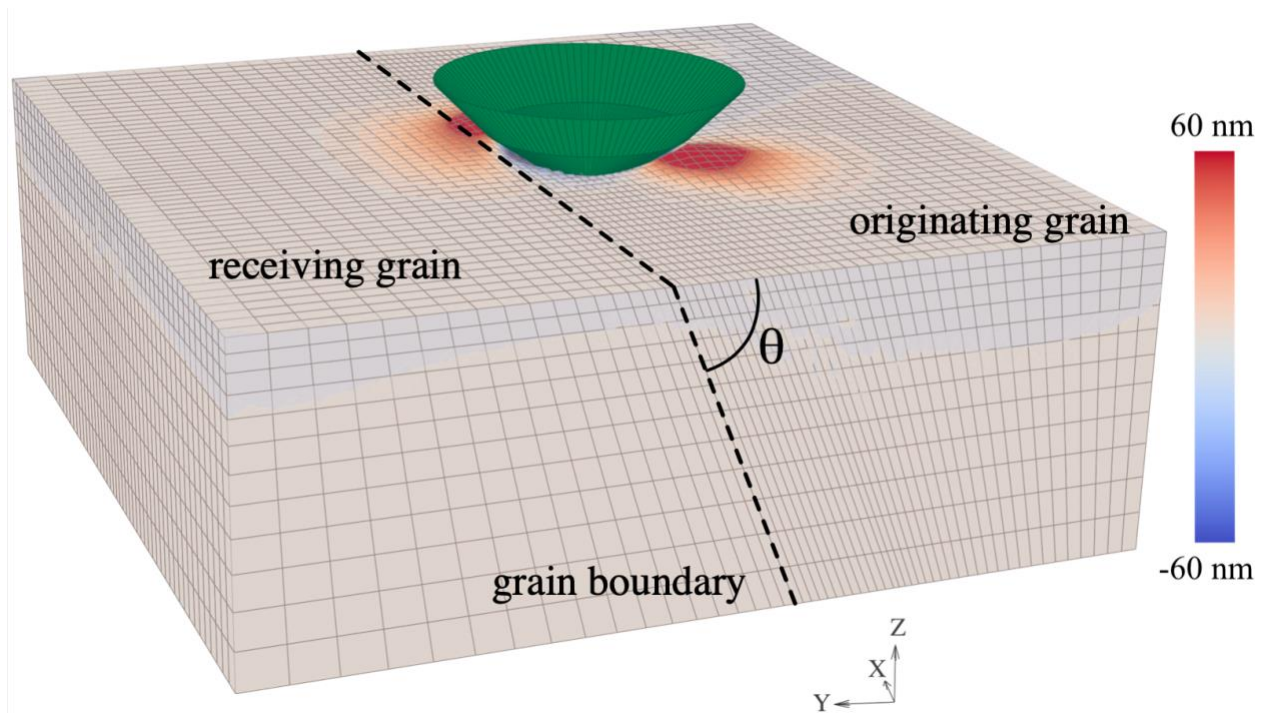


Figure 3.7: The finite element model used for a bi-crystal indentation tests where the black dotted line indicates the location of the grain boundary. The red color region indicates that the formation of surface topographies after the nanoindentation. [126]

### **3.5. Comparing of experimental and simulated indent topographies**

With the capability of simulating both single and bi-crystal nanoindentations, it is important to determine whether the nature of slip transfer can be reliably modeled using the current phenomenological CPFEM models. Thus, CPFEM simulations of the five indentations that fell on grain boundaries and nine indentations near grain boundaries, as well as several corresponding single crystal simulations of the grains on both sides of the boundaries, were carried out. Differences between simulated and measured topographies resulting from single and bi-crystal indentations are examined.

#### **3.5.1 Single crystal indent topography comparison between experiment and simulation.**

Single crystal indentation simulations of Ti, TiAl, and W ([133-135]) done in the past capture the general location and extent of the pile-up topography. In the present study, two examples of the single crystal indent topographies are shown for both experimentally measured and simulated cases in the first and second columns of Fig. 3.8, respectively. Close examination of the point-wise differences between experiment and simulation in the third column shows very good agreement between the shapes of the indent topographies and indent impression. In addition, the maximum indent depth and topography height are also found to be very close in Fig. 3.8.

Despite the generally good agreement, small systematic deviations between experimentally measured and simulated topographies are observed, illustrated by generally blue shades within the central area of the indent valley surrounded by a red-shaded ring in the central column of Fig. 3.8. These systematic deviations may be a result of a number of factors: (1) reverse plasticity may occur as the experimental load is released, resulting from the release of the back stress

associated with dislocation pile-ups; Such reverse plasticity is unlikely in the phenomenological model employed here, as it does not explicitly account for kinematic hardening resulting from dislocation pile-up formation; (2) while the indenter in the simulation is modeled as a perfect sphero-conical tip, it is quite likely that the actual indenter deviates somewhat from this geometry; (3) there may be some friction/cohesion forces between the indenter tip and sample, resulting from basic atomic interaction or indenter surface roughness that is approximated for in the simulation; (4) the simulation treats the indenter tip as a rigid body, while in fact one would expect some elastic behavior of the tip. The exact reasons for these deviations are presently not well established.

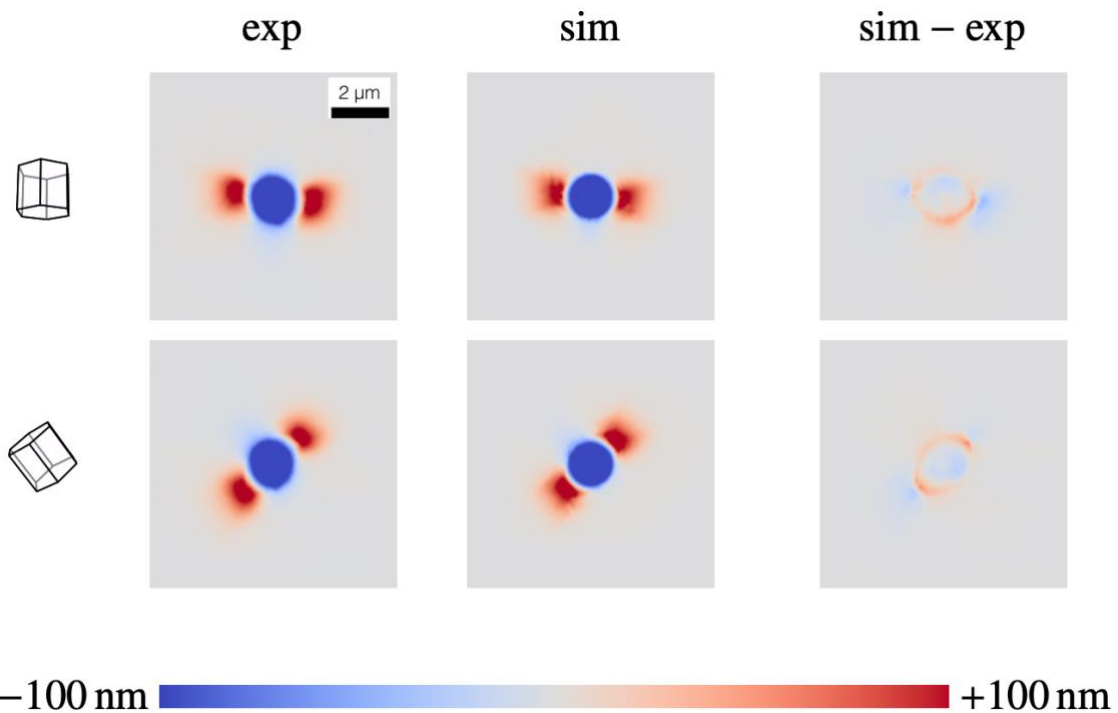


Figure 3.8: Experimentally measured (first column) and simulated (second column) topographies of two single crystal indent and the corresponding point-wise differences between experiment and simulation shown in the third column. [126]

### 3.5.2 Bi-crystal indent topography comparison between experiment and simulation.

Figures 3.9a and 3.9b show experimentally measured and simulated indent topographies of bi-crystal indentations performed on grain boundaries and near grain boundaries respectively. The third column illustrates the difference between simulated and experimental topographies, where red (blue) shades indicate the simulated topography is higher (lower) than the experiment. A careful examination of the indent topography difference maps between simulations and experiments (third column in Figs. 3.9a and 3.9b) shows that in all but one case (row three of Fig. 3.9b), the systematic red ring observed for the single crystal indents is again observed in these bi-crystal indentation comparisons. In this case the red ring is more pronounced than in the single crystal cases in Fig. 3.8, indicating potential stronger reverse plasticity caused by the presence of the grain boundary in the experiments of bi-crystal indentations than single crystal indentations. Ignoring these systematic deviations, the locations and shapes of the simulated indent topographies are consistent with the experimental measurements. By careful examination of the impression (area inside the red ring), the maximum indentation depth between experiment and simulation are found to be very close.

In addition, the comparison between the indent topography (regions with heights above the sample surface) shows that the maximum heights of both experiment and simulated topographies do not always agree in the originating grain (two examples of large discrepancies shown in Fig. 3.9a row 3 and 4). In other words, shades of blue were frequently observed in the originating grain in the third columns of Fig. 3.9a, meaning higher surface topographies has been developed in the experiments than in the simulations in the originating grain. One possible explanation is that the grain boundary resistance to strain transfer is higher in the experiment than in simulation, in other words the phenomenological model does not fully capture the actual grain boundary

resistance to plastic strain transfer. As a result of this larger resistance in experiment, the indent surface topographies are prone to form in the originating grain rather than the receiving grain in the experiment, causing the height of indent topography to be larger in experiment.

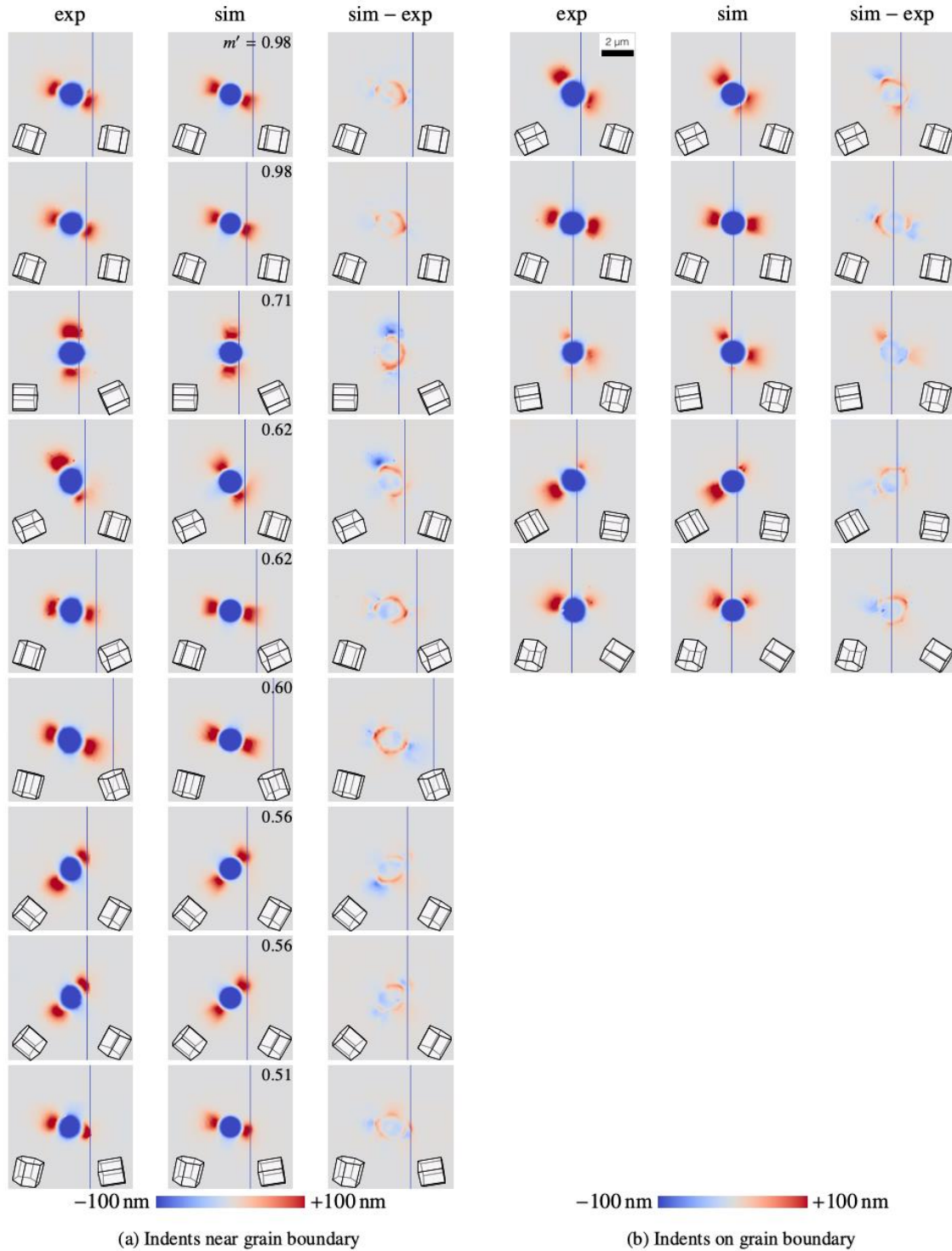


Figure 3.9: Comparisons between experimentally measured and simulated indent topographies near six grain boundaries. a) Indents that are located near the grain boundary. b) Indents that are right on the grain boundary. [126]

### 3.6. Discussion

#### 3.6.1 Quantifying the quality of single crystal and bi-crystal simulation using $\Delta V_{\text{sim.exp}}$

In addition to the point-wise comparison of indent topographies between experiments and simulations shown in section 3.5, it is also desirable to generalize the overall quality of the simulations of both single and bi-crystal indentations.

To quantify the overall accuracy of single crystal indentation simulations, the  $\Delta V_{\text{sim.exp}}^{\text{SX}}$ , calculated using Eq. 3.1 and 3.2, for single crystal indents were divided by the area over which the AFM measurements were taken and compared to the corresponding indentation noise level (same as noise level in Fig. 3.3d) in Fig. 3.10 (dotted blue and dotted red respectively). It is clear that the differences between the simulated and experimentally measured topographies are, as expected, larger than the noise level, but are still only in the range of 1.7 nm, which is very small compared to the overall indentation heights of about 150 nm. This small discrepancies of  $\Delta V_{\text{sim.exp}}$  shows that the simulation matches the experimental indentations quite well in single crystal case.

In the case of bi-crystal, the same routine was followed to calculate the  $\Delta V_{\text{sim.exp}}^{\text{BX}}$  using Eq. 3.1 and 3.2. The resulting  $\Delta V_{\text{sim.exp}}^{\text{BX}}$  is compared to the noise level of bi-crystal experiment  $\Delta V_{\text{exp.exp}}^{\text{BX(noise)}}$  in Fig. 3.10. The differences between the simulated and experimentally measured indent topography (solid blue in Fig. 3.10) are only slightly larger than the bi-crystal indentation noise level (solid red in Fig. 3.10), and are also consistently greater than the differences between the single crystal simulations and experiments (dotted blue in Fig. 7). Nonetheless, the average  $\Delta V_{\text{sim.exp}}^{\text{BX}}$  per area is still in the range of 2-4 nm, which is very small compared to the average heights of indent topographies of about 150 nm. This again shows that the general quality of the

simulations of bi-crystal indentations, though slightly worse than single crystal simulations are still quite high.

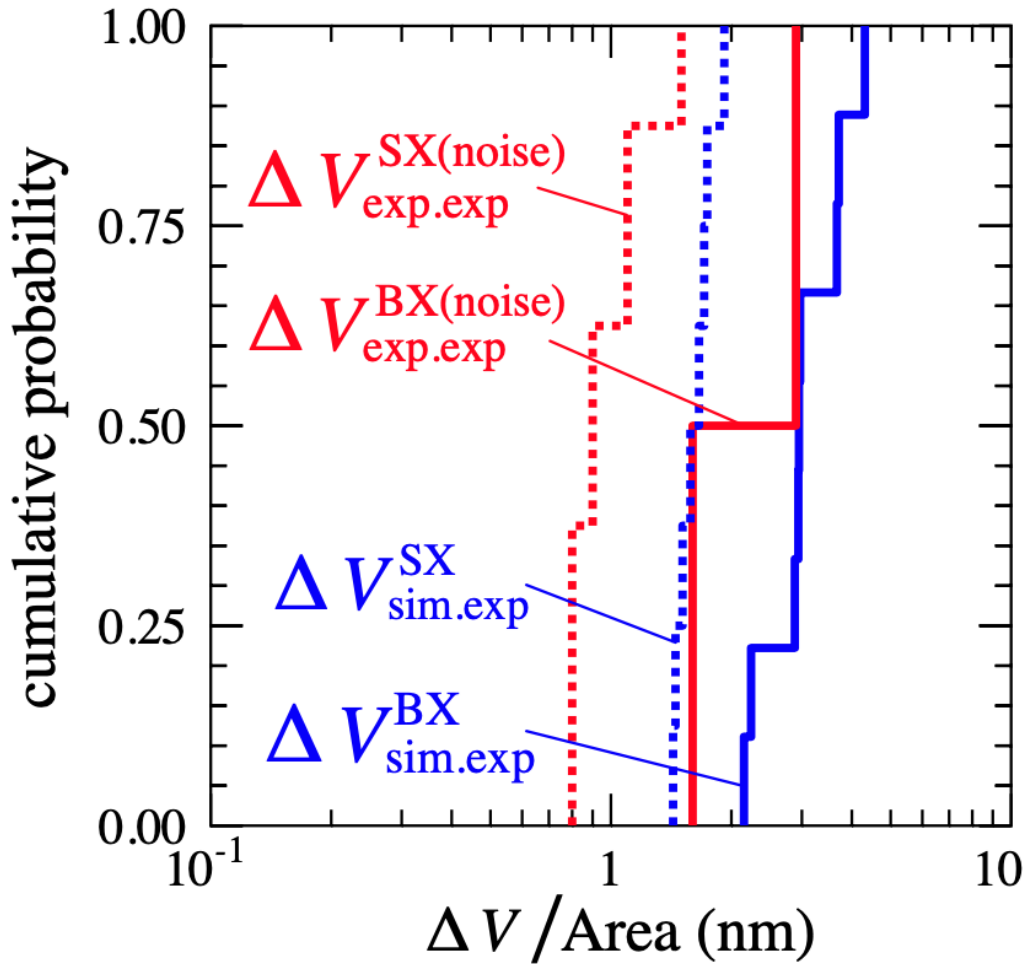


Figure 3.10: Cumulative probability distributions of the differences between simulated and experimentally measured indent topographies for single crystal and bi-crystal case are shown as dotted blue line and solid blue line, respectively. As a comparison, noise level in experimental measurements from Fig. 3.3 are plotted for single crystal (dotted red line) and bi-crystal case (solid red line). [126]

### 3.6.2 Correlating experiment and simulation results with slip transfer criterion $m'$ and $M$ (LRB criterion)

It has been shown that in both experiments and simulations (in Fig. 3.9a), the indent topographies development in the receiving grain is almost unhindered in cases where the slip systems of both adjacent grains are well aligned (first two rows in Fig. 3.9a), while in cases of poor alignment the indent topographies in the receiving grain are strongly limited (last two rows in Fig. 3.9a). To understand more on how different grain boundaries influence the development of bi-crystal indent topographies, a comprehensive analysis of  $\Delta V$  and  $V$  was carried out on the overall data set, including experiments and simulations of both single and bi-crystal indent topographies.

To facilitate the comparison, the  $\Delta V$  and  $V$  are evaluated separately for the indent topography in both the originating and receiving grains (i.e., left and right of the grain boundary shown in Fig. 3.11a, with indent topographies colored in red and impressions in blue) to quantify the influence of a grain boundary on the indent topography. All the results are shown in Fig. 3.11(b-d) as a function of slip transfer criterion  $m'$  or LRB.

Figures 3.11b and c plot the  $V$  ratios and the normalized values of  $\Delta V = 2(V_a - V_b)/(V_a + V_b)$  between bi-crystal and single crystal indents as a function of  $m'$ , with the experimentally measured values represented by crosses and the simulated values represented by circles, and the red and black representing the originating and receiving grain, respectively. The grain boundaries do not have a significant effect on the indent topography in the originating grains, as indicated by the red symbols being clustered around  $V$  ratios of one in Fig. 3.11b and normalized  $\Delta V$  of zero in Fig. 3.11c. In contrast, the differences in indent topography in the receiving grains (black symbols) between bi-crystal and single crystal indents increase with decreasing  $m'$ .

Similar behavior is noted for plots of normalized  $\Delta V$  versus  $M$  (LRB parameter) in Fig. 3.11e. The  $\Delta V_{\text{SX.BX}}^{\text{receiving}}$  displays a roughly linear correlation with  $M$ , (black crosses in Fig. 3.11e), while the  $m'$  shows a more exponential relationship, (black crosses in Fig. 3.11c). Furthermore, the ratios of the simulated  $V_{\text{BX}}^{\text{receiving}}/V_{\text{SX}}^{\text{receiving}}$  (black circles), which are consistently smaller than the experimentally measured ratios (black crosses), do not show strong functional relationships with  $m'$  or  $M$ . Though the two measures,  $\Delta V$  and  $V$ , are assessed across the entire positive and negative indent topography in Fig. 3.10, the two measures have been evaluated for indent pile-up (positive) and impression (negative) separately. Similar trends and conclusions are observed in all of these analyses, indicating that the overall indent topography is sufficient for quantifying the influence of grain boundaries on plastic strain transfer.

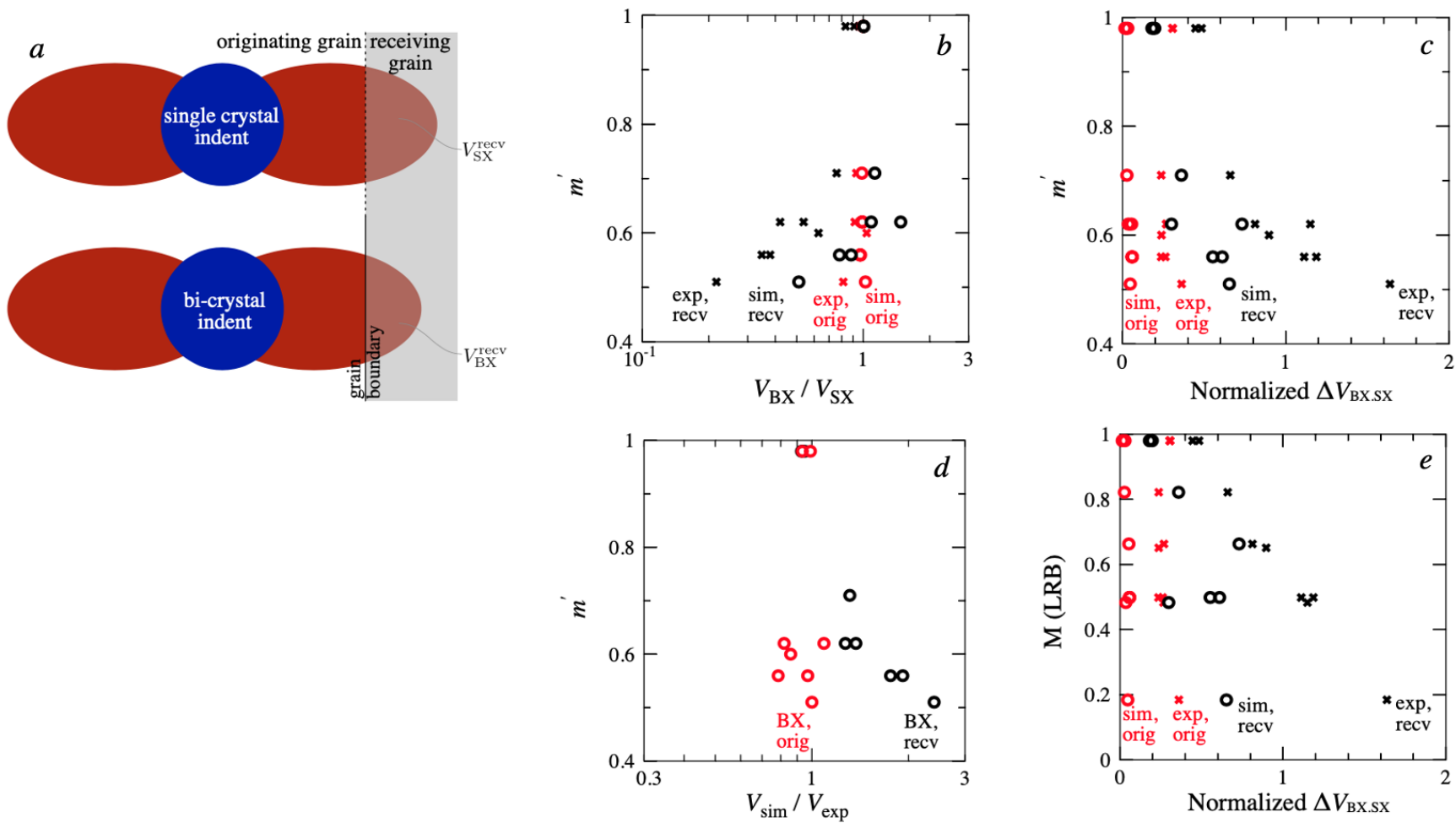


Figure 3.11: a): Schematic single and bi-crystal indents with gray areas representing  $V_{SX}^{receiving}$  (top) and  $V_{BX}^{receiving}$  (bottom). The grain boundary in the bi-crystal case is marked by a vertical solid line and continued as an imaginary ‘grain boundary’ for the single crystal case. b):  $m'$  vs. volume ratio (markers for experiment  $\times$  and simulation  $\circ$ ) between bi-crystal and originating single crystal

Figure 3.11 (cont'd) indents evaluated within the originating grain (red) and the receiving grain (black). c):  $m'$  vs. normalized volume difference (markers for experiment  $\times$  and simulation  $\circ$ ) between bi-crystal and originating single crystal indents evaluated within the originating grain (red) and the receiving grain (black). d): Volume ratio between simulated and measured bi-crystal indents evaluated within the originating grain (red circles) and the receiving grain (black circles). e):  $M$  vs. normalized volume difference (both sim and exp) between bi-crystal and originating single crystal indents evaluated within the originating grain (red) and the receiving grain (black). [126]

To interpret the difference between simulated and experimentally measured bi-crystal topographies, a number of factors that influence the kinematic response of a bi-crystal to an indentation can be considered. First, the difference in crystal orientation between the originating and receiving grain results in corresponding differences in the resolved shear stresses on the slip systems on either side of the boundary. This purely crystallographic effect is accurately captured by the crystal plasticity framework, so the differences between experiments and simulations cannot be rationalized simply on crystallographic characteristics. Second, a boundary can act as an intrinsic obstacle to plastic flow by hindering the passage of dislocations through (or dislocation absorption and nucleation at) the boundary into the receiving grain, leading to pile-ups of same-sign dislocations and local stress build-up. Barriers to plasticity activation the receiving side of a boundary are not accounted for in the phenomenological constitutive description, and it is not entirely clear how to best incorporate them into the plasticity framework. A number of approaches have been taken by other researchers that can be computationally expensive and that have varying levels of effectiveness ([110, 111, 114]). It is interesting to note that this intrinsic resistance to strain transfer at the boundaries increases with decreasing  $m'$ , as indicated by the growing discrepancy between the experiments (black crosses) and simulations (black circles) at lower  $m'$  boundaries (Figs. 3.11b and 3.11c), so that improvements to such models need to consider the effects of disorientation on the boundary resistance to plastic flow. Third, the ease of dislocation nucleation in the receiving grain (probably dislocation-starved) will also influence the kinematic response of the bi-crystal to an indentation. The present model effectively assumes an abundance of mobile dislocations at every material point to carry plasticity wherever the acting stress is sufficiently high, but this may not be the actual physical situation, where dislocation sources may be limited both at the boundary

and within the two grains. Such source limitations could be a reason for the consistently larger values of  $V_{\text{BX}}^{\text{receiving}}/V_{\text{SX}}^{\text{receiving}}$  and  $\Delta V_{\text{BX.SX}}^{\text{receiving}}$  in the experiments than in the simulations.

Finally, the model also fails to account for the cooperative backward motion of blocked dislocations within the originating grain that could result in a concurrent back flow of plasticity on the receiving side of the grain boundary upon release of the indentation load, which would result in the lower experimentally measured topographies in the receiving grain than predicted by the simulations. Given that the current model is purely phenomenological and lacking any detailed dislocation mechanics, the generally good agreement suggests that the kinematic incompatibility, which is naturally taken into account by crystal plasticity, plays a key role in the deformation process near grain boundaries in commercially pure  $\alpha$ -Ti. Since the present comparison between experimental and simulated topographies is done at a convenient but arbitrary indentation depth, it remains open whether such good agreement holds also for the prior evolution of topography with indentation depth.

### **3.6.3 Grain boundary sensitive CPFEM model for bi-crystal nanoindentation**

The comparison of simulated and experimentally measured bi-crystal indent topographies in the last section revealed an underestimation of grain boundary resistance to slip in the current CPFEM model compared to the experimental observations. In an attempt to remedy this discrepancy between model and observation, the original model for bi-crystal nanoindentation was modified by including a hardened layer of elements to act as a grain boundary. The material properties of the grain boundary elements were assigned independently from grain interior, meaning that all the material parameters used for grain boundary element were set according to the grain boundary character. For those grain boundaries with high resistance to slip transfer

(low  $m'$ ), the boundary layer elements are modeled using a harder material, and for boundaries with low resistance (high  $m'$ ) vice versa.

### 3.6.3.1 modified bi-crystal nanoindentation model and slip parameters in the model

The modified bi-crystal nanoindentation model, shown in Fig. 3.12, has two additional layers of grain boundary elements compared to the original model. The crystal orientation of each grain boundary layer is consistent with the orientation of the corresponding grain interior (for example, in Fig. 3.12, the crystal orientation of the right layer is the same as that of the right grain). The inclination of the two grain boundary layers was acquired from the FIB-cross section measurement detailed in section 2.3.2. The thickness of each of these two layers was set to around 200 nm, which is a relatively small number compared to the size of the indentation ( $\sim 2-3 \mu\text{m}$ ) while large enough to influence the strain transfer across the grain boundary in the simulation.

The commonly used slip parameters that control individual slip system in the current phenomenological model (for both grain interior and grain boundary) are the initial slip resistance  $\tau_0$ , saturation slip resistance  $\tau_{\text{sat}}$ , initial hardening slope  $h_0$ , and hardening exponent  $a$ . These four slip parameters define the shape of strain hardening curve of the modeled material illustrated in Fig. 3.13 (left). By changing the magnitude of each parameter, the hardening of the material undergoes a different path. For example, a larger value of  $h_0$  causes the material to harden faster in the beginning of the plastic deformation, while a larger  $\tau_0$  indicates that the resolved shear stress required to initiate each slip system is higher. The values of slip parameters used in the original bi-crystal nanoindentation model is shown in Fig. 3.13 (right) ( $a$  is set to 2 as constant). Each slip system had a different range of initial and saturation resistance, while the  $h_0$

and  $a$  were set to 1 and 2, respectively. Regarding to the slip parameters of the grain boundary layer, it is still unclear how to choose the optimal values. As a result, multiple groups of slip parameters were examined with the modified model, and the group that generated the most accurate simulation results was chosen as the optimal slip parameters for that grain boundary layer.

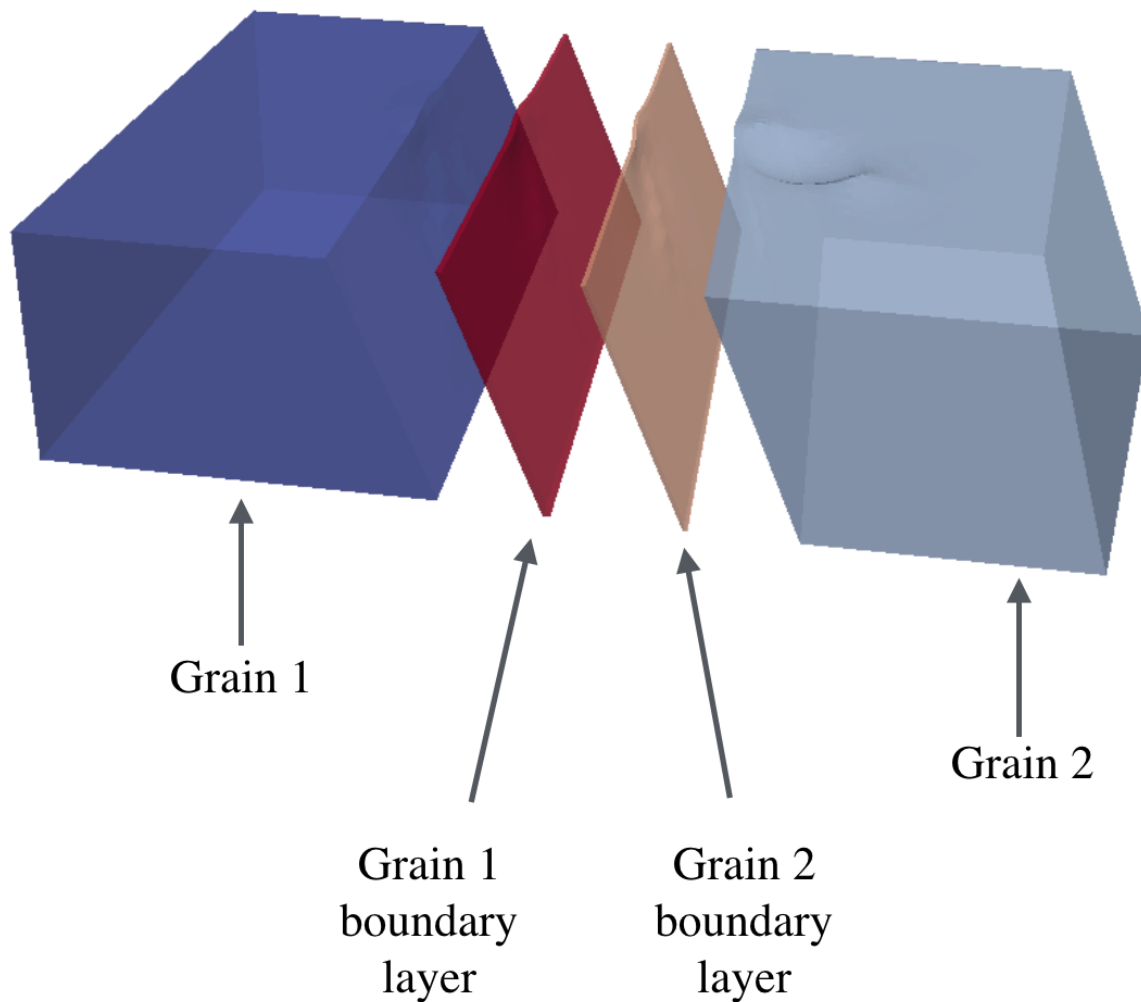


Figure 3.12: The grain boundary sensitive model proposed as a revision to the original model by inserting two layers of elements (Grain 1 boundary layer and grain 2 boundary layer) between the two adjacent grain 1 and 2.

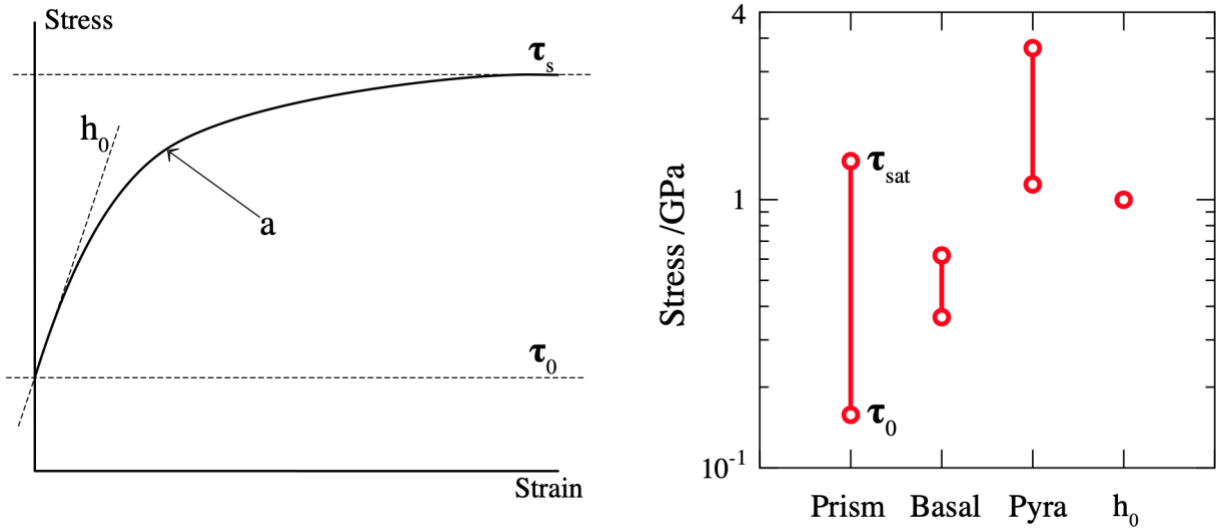


Figure 3.13: The physical meaning of the four slip parameters in the model is shown in a stress-strain curve in the left figure. The values of the  $\tau_0$  and  $\tau_{sat}$  used in the original model are presented in the right graph.

### 3.6.3.2 Optimizing the slip parameters of the grain boundary layer

To determine the optimal slip parameters for the grain boundary layer elements, slip parameters of all grain boundary elements, including  $\tau_0$ ,  $\tau_{\text{sat}}$ ,  $h_0$ , and  $a$ , were altered independently<sup>7</sup> (one dimensional optimization) to assess the influence of each slip parameter on the accuracy of the model. To accurately evaluate the influence of the grain boundary layer on the development of indent topography across the boundary in the bi-crystal indentation model, an objective function, used to optimize  $\tau_0$ ,  $\tau_{\text{sat}}$ ,  $h_0$ , and  $a$ , was determined to be  $V_{\text{sim}}^{\text{receiving}} / V_{\text{exp}}^{\text{receiving}}$ , which is the ratio between the volume of the simulated and the measured indent topography in the receiving grain.

The outcome of the optimization for each set of slip parameters ( $\tau_0$ ,  $\tau_{\text{sat}}$ ,  $h_0$ , and  $a$ ) of a the studied grain boundary is shown in Fig. 3.14(a-c). The values of individual slip parameters were plotted against the objective function  $V_{\text{sim}}^{\text{receiving}} / V_{\text{exp}}^{\text{receiving}}$ . As the  $\tau_0$  and  $\tau_{\text{sat}}$  are modified simultaneously by the same ratio their results are shown in one plot (Fig. 3.14c). It can be concluded from Fig. 3.14(a,b) that both the initial hardening slope,  $h_0$ , and hardening exponent,  $a$ , play no significant roles in providing additional grain boundary resistance to slip transfer as the objective function remains almost constant at all values of  $h_0$ , and  $a$ . As is shown in Fig. 3.14c, the model is quite sensitive to the combined initial and saturated slip resistance,  $\tau_0$  and  $\tau_{\text{sat}}$ . By increasing the values of both  $\tau_0$  and  $\tau_{\text{sat}}$ , the resistance to slip transfer rises significantly in the grain boundary region, leading to considerable drop of the objective function. In Fig. 3.14c a plateau is also observed at the end of the curve when  $\tau_0$  and  $\tau_{\text{sat}}$  are increased

---

<sup>7</sup> Due to the correlation between  $\tau_0$  and  $\tau_{\text{sat}}$  and the requirement of  $\tau_0 < \tau_{\text{sat}}$ , these two slip parameters cannot be adjusted independently. As a result, these two parameters are either increased or decreased simultaneously by the same ratio in this study.

more than  $\sim 2.0$  times of the original value. This suggests that there is an upper limit of the resistance to strain transfer that the grain boundary layer is able to provide. In other words, the grain boundary resistance to strain transfer remains constant, regardless how much the  $\tau_0$  and  $\tau_{\text{sat}}$  is raised beyond the limit. One possible explanation is that when the grain boundary layer elements are hardened beyond this limit, those elements become so difficult to deform that the grain boundary layer is pushed away from the indenter as a whole “rigid body”. In such a scenario,  $\tau_0$  and  $\tau_{\text{sat}}$  will not play a significant role in the strain transfer as the grain boundary is not heavily deformed. In general, the underestimation of grain boundary resistance to strain transfer can be best compensated at and above this limit, which is at  $\tau_{\text{sat}(0)}^{\text{revised}} \approx 3\tau_{\text{sat}(0)}$ . The same optimization procedure was conducted at another three grain boundaries. The limits that provide the most accurate simulations in the receiving grain were acquired for each grain boundary studied and are plotted as a function of  $m'$  in Fig. 3.14d. A positive correlation between the limits and the  $m'$  is observed. This suggests that two adjoining grains with poor slip system alignment (low  $m'$ ) need higher magnitude of compensation of grain boundary resistance in the model, which is fulfilled by the larger limit of  $\tau_{\text{sat}(0)}^{\text{revised}}/\tau_{\text{sat}(0)}$  shown in the Fig. 3.14d.

In summary, by incorporating a hardened grain boundary layer into the bi-crystal indentation model, some success has been achieved in providing more accurate simulation results of the indent topographies. This study is a preliminary attempt to improve the CPFE model accuracy in the vicinity of grain boundary, and by no means the most consistent and physically meaningful method to simulate heterogeneous deformation near grain boundary.

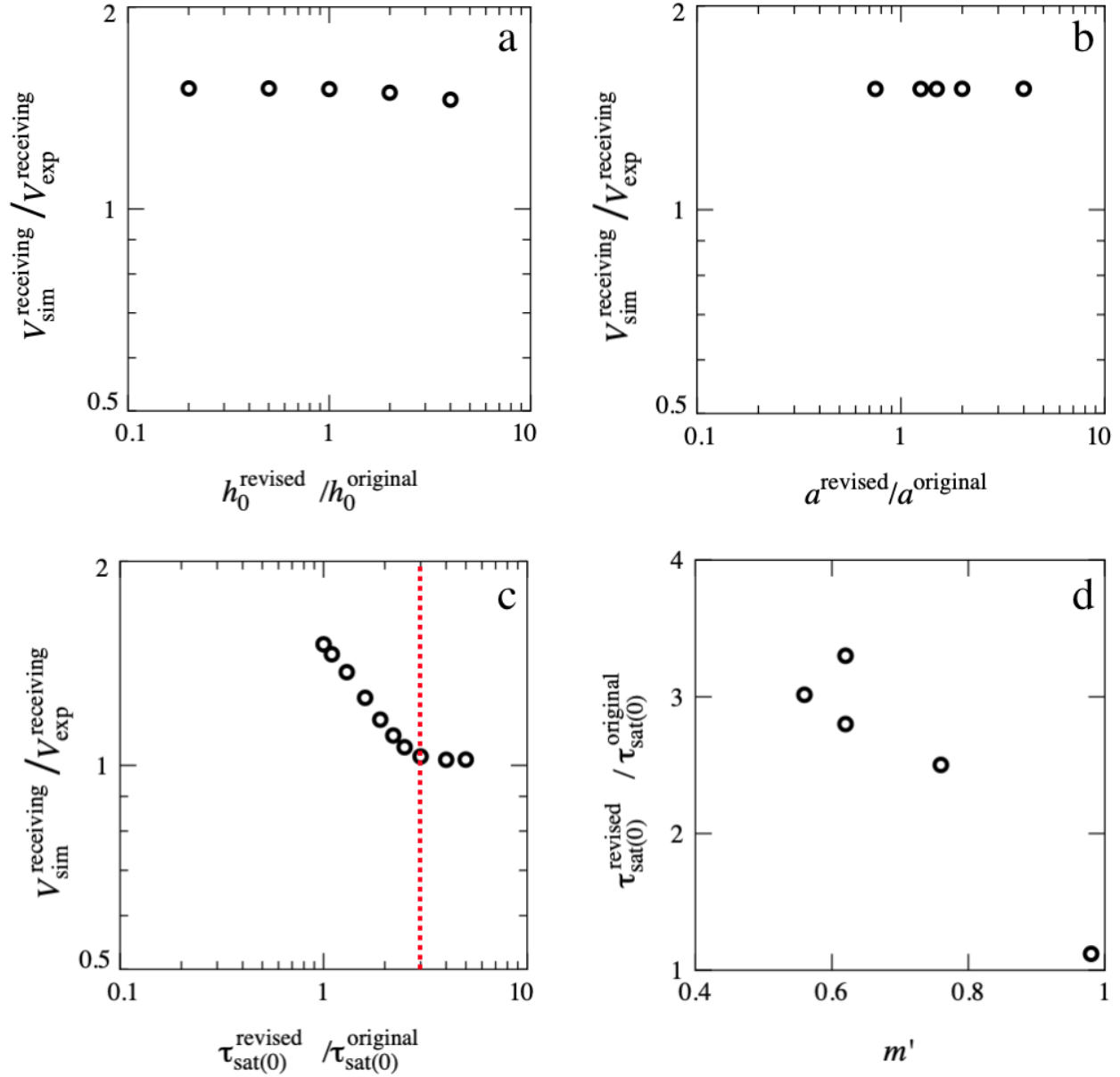


Figure 3.14: Figure (a-c) show how the accuracy of the new model ( $V_{sim}^{receiving} / V_{exp}^{receiving}$ ) alters as a function of the change in each slip parameters ( $h_0$ ,  $a$ , and  $\tau_{sat(0)}$ ). The red dotted line indicates the optimal value of  $\tau_{sat(0)}$  (in the ratio form of  $\tau_{sat(0)}^{revised} / \tau_{sat(0)}^{original}$ ) that generates the most accurate simulation compared to experiment. Figure d presents all the optimal values of  $\tau_{sat(0)}$  acquired at four grain boundaries as a function of the four  $m'$ .

### 3.7 Conclusions

The deformation process of nanoindentations in both grain boundary interiors and near a number of low and high angle grain boundaries are characterized using instrumented nanoindentation, EBSD, FIB, AFM and CPFÉ modeling in commercially pure  $\alpha$ -Ti. The deformation has been assessed using indent topographies.

The reproducibility of this method was evaluated by determining the variation in indent topographies carried out under nominally identical orientation conditions. The average topography deviation is only about 1 nm for single crystal indents and 2-4 nm for bi-crystal indents, compared to maximum topography elevations of approximately 150 nm, indicating that the indentation deformation is reproducible and hence it is reasonable to quantify the deformation processes using indent topography.

Comparisons of bi-crystal and corresponding single crystal indentation topographies reveal that grain boundaries with poorly aligned slip systems, as indicated by low  $m'$ , tend to develop limited amount of topography across the boundary into the receiving grain, suggesting that it is difficult to transfer slip across these boundaries, while high  $m'$  boundaries show only minimal reduction in the topography in the receiving grain. This proves that the study of bi-crystal indent topography can lead to the estimation of resistance of different grain boundaries to slip transfer. Furthermore, quantitative comparisons show good agreement between experimentally measured and CPFÉ simulated indent topographies, indicating that the crystal plasticity kinematics is a dominant factor in both single and bi-crystal indentation deformation. Nevertheless, these comparisons also reveal two types of systematic differences between experiment measurements and simulation results. The consistent deviations near the indent impression observed in both single and bi-crystal indentation comparisons are potentially caused by insufficient accuracy of

modeling the tip and its interaction with the sample, or may be caused by disregarding reverse plasticity in the model. The simulations often overestimate the deformation transfer to a small degree, especially for high-angle grain boundaries. Such overprediction of topography heights in the simulations is likely due to a neglect of explicit dislocation-grain boundary interactions and dislocation nucleation processes, particularly when considering the receiving side of the grain boundary being probably deprived of mobile dislocations before the indentation process.

An attempt to resolve the underestimation of the grain boundary resistance to strain transfer in the model has been made by incorporating a hardened layer of elements as grain boundary. Optimized slip parameters such as  $\tau_0$ ,  $\tau_{\text{sat}}$ ,  $h_0$ , and  $a$  were obtained by minimizing the differences between modeled and simulated indent topography. The revised model with tuned slip parameters was proved to provide more accurate simulation of the indent topography compared to the original bi-crystal indentation model.

## CHAPTER 4 PREDICTING SLIP TRANSFER ACROSS GRAIN BOUNDARIES WITH AN ITERATIVE STRESS RELIEF MODEL

As discussed in section 1.2, predictive metrics/models for assessing slip transfer at grain boundary are a paramount component to a complete description of the heterogeneous plastic deformation in polycrystal. Most of the proposed slip transfer criterion/models, such as  $N_{LC}$  [5],  $m'$ ,  $M$  (LRB criterion [9]), and  $M_s$  [7], are based on the assumption that the shear (slip or twin) of the incoming slip system is accommodated by only one outgoing slip system in its neighboring grain. Nevertheless, it is quite possible or even common that the accommodation of the incoming shear requires the activation of multiple outgoing slip systems. Early research of Livingston and Chalmers [5] suggested that the active outgoing slip systems should be decided based on the requirement of continuity of grain boundary strain. This approach, more commonly termed “tangential continuity”, is the only model capable of resolving the accommodation of shear through multiple slip systems at a grain boundary. Experimental validation of the tangential continuity model is rarely reported. Thus, it is desirable to further explore new theories/models of shear accommodation at grain boundaries and use tangential continuity model as a benchmark for comparison.

In this Chapter, slip trace analysis combined with AFM and EBSD is used for analyzing the slip accommodation observed at multiple grain boundaries in ~1.5% strained  $\alpha$ -Ti specimen. Two types of slip accommodation were observed most frequently: 1) the incoming slip system is accommodated by only one dominant outgoing slip system. 2) the incoming shear is accommodated by two outgoing slip systems with comparable amount of shears. To rationalize the two types of slip accommodations, a new iterative stress relief model was developed. This

new model, in addition to the tangential continuity model, was tested based on the slip accommodation observations. Optimizations of the model parameters, such as critical resolved shear stress (CRSS) ratios, were conducted to improve the accuracy of the new model.

#### **4.1 Observations of slip accommodation in $\alpha$ -Ti**

Slip band accommodation at grain boundaries was not commonly observed due to the low level of strain approximately 1.5%.<sup>8</sup> After investigating hundreds of grain boundary pairs using SEM, three types of slip transfer were found, as shown in Fig. 4.1. (SEM images of all slip transfer cases, as well as corresponding AFM measurements, are presented in Appendix A) Figure 4.1(top left) presents an example of a grain boundary where the slip line on both sides do not meet at grain boundary, indicating no apparent relationship between the slip lines on opposite side of the boundary. In most of these cases, including Fig 4.1(top left), the spacing pattern between slip lines are different and the differing sense of contrast of slip band in the SEM image suggests an opposite sense of shear, further supporting the argument that there is no correlation between two sets of slip bands on opposite side of the boundary. Figure 4.1(top center) shows an example of well-correlated slip transfer across a grain boundary, where the incoming slip system is accommodated by a unique outgoing slip system in the neighboring grain. Due to the one slip band-to-one slip band relation, the spacings between slip bands in both grains are correlated but not necessarily distributed evenly. Such “single accommodation” events occurred at about 30% of those boundaries with slip lines in the vicinity. In contrast, the top right image of Fig 4.1

---

<sup>8</sup> There are several advantages of using low strain to study slip transfer: 1) The surface remains relatively flat even at grain boundaries, which enables accurate AFM measurement and slip trace analysis in the vicinity of the grain boundary. 2) At low strain levels, the slip transfer plays a critical role in the activities of slip systems near grain boundaries (dislocations tend to nucleate at grain boundaries), while at high level of strain the nucleation of dislocations can also occur in the grain interior, complicating the whole analysis. 3) Cross-slip, which is rarely observed at low strain and more frequently found at high strain, is not desired in this study.

presents a scenario where a single set of slip lines in an incoming grain correlates with two sets of slip lines emanating from the boundary intersection in the outgoing grain. In these cases, the slip system in the incoming grain is well correlated at the grain boundary with the two outgoing slip bands. It is worth noting that at the grain boundaries where this double slip accommodation occurred, no signs of single slip accommodation were ever observed. These suggests the double slip accommodation mechanism is critical at these particular boundaries. This “double accommodation” cases were much less common than single slip accommodation, presenting only at a very small fraction of all grain boundaries. There were no observations of triple accommodation.

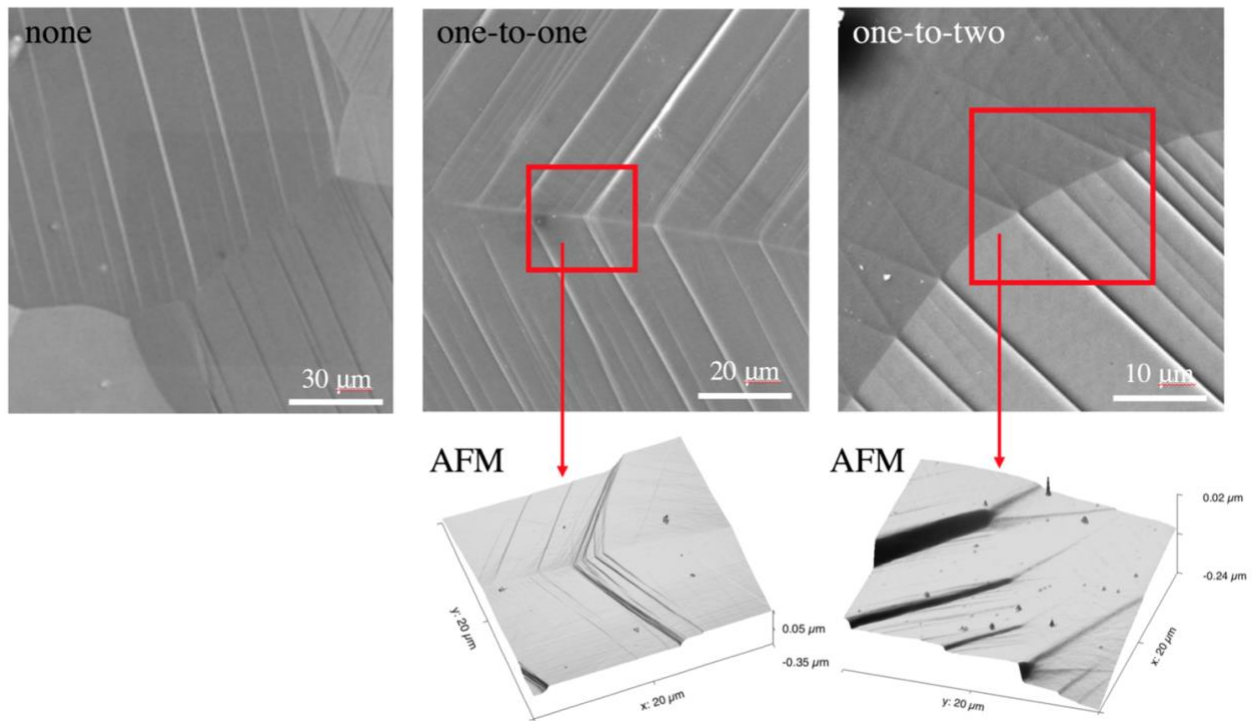


Figure 4.1: Secondary electron images of the three categories of slip accommodation: non-correlated (left), one-to-one correlated slip (center), one-to-two correlated slip (right), and corresponding topography maps measured by AFM (second row).

## **4.2 Determining the active slip systems, relative shears, and slip geometries of experimentally observed slip accommodations**

To carry out quantitative analysis on the slip transfer/accommodation at various grain boundaries, it is necessary to identify the active deformation systems, their relative shear, and slip system alignment across a grain boundary.

Active deformation systems were identified using slip trace analysis (detailed in section 2.4). To eliminate ambiguity in cases where the expected traces of more than one potential slip plane had traces close to that of the observed trace, the slip plane with an inclination closest to the slope of the surface slip step was chosen (as shown in Fig. 2.8c). A variety of slip plane types were observed to be associated with both single and double accommodation, including prism, basal, and pyramidal planes. In cases where prism planes were identified as the active slip plane, the Burgers vector is fixed as there is only one slip direction on these planes. In cases where the basal and pyramidal planes were identified as the active slip plane, the active Burgers vector was assumed to be the one with the largest resolved shear stress (under the global uniaxial tensile stress). In the present study, due to the material texture and the low level of strain (~1.5%), the development of deformation twinning was very limited. In no cases was twinning observed to be involved in single accommodation and in only one case was twinning observed in a double accommodation slip transfer. In that unique case the incoming slip band was accommodated by T1 deformation twinning in the outgoing grain in conjunction with dislocation slip on a secondary accommodating slip system.

With the active slip systems determined, the alignment of the deformation systems across a grain boundary can be assessed by quantifying the angles that are related to the geometry of the slip transfer:  $\kappa$  (angle between incoming and outgoing Burgers vectors),  $\phi$  (angle between slip

plane normals of incoming and outgoing systems), and  $\psi$  (the angle between the slip plane traces on the grain boundary).

The relative shear on each identified deformation system was quantified using a quantitative AFM analysis proposed by Y. Yang *et al.* [43] [44]. This analysis was performed on some of the single accommodation and all of the double accommodation cases, where surface elevation maps of the shear accommodation events were collected near the grain boundaries to quantify the step heights associated with the two or three deformation systems involved in the accommodation (shown in Fig. 4.1 bottom row). The step heights along the specimen surface normal  $\mathbf{n}^{\text{surface}}$  were transformed into the number of dislocations associated with the shear of the identified active deformation system (with known Burgers vector  $\mathbf{b}$ ) using:

$$N = h/(\mathbf{b} \cdot \mathbf{n}^{\text{surface}}) \quad \text{Eq. 4.1}$$

The identified slip systems, their alignment across a grain boundary, and for some of them the number of dislocations in each slip system are compiled in table 1. In table 1, columns 2 and 3 show the active Burgers vectors and planes of the incoming and outgoing deformation systems, columns 4 to 6 specify their geometric relationships across the grain boundary, while columns 7 and 8 list the number of dislocations associated with the shear that formed the incoming and outgoing slip/twinning bands and resulted in the surface topography (Eq. 4.1). (It should be noted that  $\psi$  was only determined for seven cases, as it requires FIB sections to be cut (see below), while AFM slip band measurement were only performed on eight cases.). In the vast majority of cases, the incoming deformation system was of prism  $\langle \mathbf{a} \rangle$  type. Only three out of the 16 single accommodation events observed exhibited activity by systems other than prism  $\langle \mathbf{a} \rangle$ . Four out of six of the incoming deformation systems, as well as three out of six primary outgoing systems in double accommodation events, were prism  $\langle \mathbf{a} \rangle$ , while the secondary

outgoing deformation systems involved a variety of deformation systems. The relative shears on the incoming and outgoing deformation systems were determined from the AFM quantified number of dislocations for two of the single and all of the double accommodation cases. From the two evaluated single accommodation cases, it was determined that the shear in the incoming and outgoing slip band were always very close.<sup>9</sup>

---

<sup>9</sup> While the slip systems on both sides of the grain boundary are not perfectly aligned in cases 14 and 15, the number of dislocations in the incoming and the only outgoing slip band are very close. This suggests that in single slip accommodation it is possible, or even likely, to have a one-to-one ratio between the numbers of incoming and outgoing dislocations. Nevertheless, this type of slip transfer will still leave grain boundary residual dislocations. In the cases 14 and 15, the total residual Burgers vectors is 4% and 12% of the total incoming Burgers vectors, respectively.

Table 4.1: Slip systems, geometric parameters of slip transfer, and number of dislocations in the slip bands for all 22 (16 single plus 6 double) slip accommodation observations.<sup>10</sup>

case	incoming system	outgoing system(s)	geometry at grain boundary			dislocation count	
			$\kappa$	$\phi$	$\psi$	incoming	outgoing
1	$[2\bar{1}\bar{1}0](01\bar{1}0)$	$[1\bar{2}10](\bar{1}010)$	17.8°	14.8°			
2	$[\bar{1}\bar{1}20](1\bar{1}00)$	$[\bar{2}110](0001)$	18.5°	21.0°			
3	$[2\bar{1}\bar{1}0](01\bar{1}0)$	$[2\bar{1}\bar{1}0](01\bar{1}0)$	14.7°	13.7°			
4	$[\bar{1}\bar{2}\bar{1}0](\bar{1}010)$	$[11\bar{2}0](1\bar{1}00)$	11.7°	12.5°			
5	$[\bar{1}\bar{2}\bar{1}0](\bar{1}010)$	$[11\bar{2}0](1\bar{1}00)$	8.4°	14.4°			
6	$[11\bar{2}0](1\bar{1}00)$	$[11\bar{2}0](1\bar{1}00)$	9.8°	9.6°			
7	$[1\bar{2}10](\bar{1}010)$	$[\bar{2}110](0001)$	5.0°	10.7°			
8	$[\bar{1}\bar{1}20](1\bar{1}00)$	$[11\bar{2}0](1\bar{1}00)$	1.8°	11.8°			
9	$[1\bar{2}10](\bar{1}010)$	$[\bar{1}\bar{2}\bar{1}0](10\bar{1}1)$	22.5°	36.7°			
10	$[11\bar{2}0](1\bar{1}00)$	$[11\bar{2}0](1\bar{1}00)$	15.0°	10.5°			
11	$[2\bar{1}\bar{1}0](01\bar{1}0)$	$[\bar{1}\bar{1}20](1\bar{1}00)$	4.7°	4.0°			
12	$[\bar{1}\bar{1}20](1\bar{1}00)$	$[\bar{1}\bar{1}20](1\bar{1}00)$	18.9°	38.4°			
13	$[\bar{2}110](01\bar{1}0)$	$[\bar{1}\bar{1}20](1\bar{1}00)$	2.9°	7.8°			
14	$[\bar{1}\bar{1}20](1\bar{1}00)$	$[2\bar{1}\bar{1}0](01\bar{1}0)$	9.1°	7.2°	18.3°	479	486
15	$[\bar{1}\bar{1}20](1\bar{1}00)$	$[1\bar{2}10](\bar{1}010)$	12.5°	20.3°	54.1°	628	611
16	$[11\bar{2}0](1\bar{1}00)$	$[1\bar{2}10](\bar{1}010)$	14.3°	7.9°			
17	$[1\bar{2}10](\bar{1}010)$	$[11\bar{2}0](0001)$	34.0°	30.8°	37.9°	457	319
		$[2\bar{1}\bar{1}0](01\bar{1}1)$	86.0°	85.0°	7.7°		212
18	$[\bar{1}\bar{2}\bar{1}0](\bar{1}010)$	$[\bar{1}\bar{1}20](\bar{1}101)$	27.2°	54.6°	45.6°	164	114
		$[11\bar{2}0](1\bar{1}01)$	81.2°	86.1°	8.8°		93
19	$[1\bar{2}10](\bar{1}010)$	$[2\bar{1}\bar{1}0](01\bar{1}0)$	21.7°	15.5°	11.3°	20	13
		$[\bar{2}113](10\bar{1}1)$	76.2°	75.2°	10.3°		8
20	$[\bar{1}\bar{1}20](0001)$	$[\bar{1}\bar{1}20](1\bar{1}00)$	6.5°	12.6°	13.6°	659	708
		$[1\bar{2}10](\bar{1}010)$	66.0°	46.7°	8.3°		90
21	$[\bar{2}110](0\bar{1}11)$	$[1\bar{2}10](\bar{1}010)$	27.7°	22.1°	29.1°	250	172
		$[1\bar{2}13](01\bar{1}1)$	73.7°	65.0°	20.7°		115
22	$[\bar{1}\bar{2}\bar{1}0](\bar{1}010)$	$[1\bar{1}01](1\bar{1}02)$	26.7°	7.4°		289	198
		$[2\bar{1}\bar{1}3](1\bar{1}01)$	65.9°	70.2°			87

<sup>10</sup> Columns 2-3: Burgers vector and slip plane normal of incoming and outgoing deformation systems for all shear accommodation observations (cases 1–16 are single accommodation and cases 17–22 are double accommodation). Columns 4–6:  $\kappa$  (angle between incoming and outgoing Burgers vectors),  $\phi$  (angle between slip plane normals of incoming and outgoing systems), and  $\psi$  (the angle between the slip plane traces on the grain boundary).  $\psi$  was calculated based on Eq. 2.1 and requires a FIB cross section, which was done for seven cases. Columns 7 and 8: Number of Burgers vectors in each slip band was calculated based on Eq. 4.1 and requires surface topography measurements, which was done for eight cases.

## 4.3 Assessment of the tangential continuity theory based on slip transfer observations

### 4.3.1 Tangential continuity theory

As discussed in section 1.2.2, the concept of the tangential continuity was first brought forward by Livingston and Chalmers [5]. They claimed that “The continuity of material at the grain boundary must be maintained”. The continuity of the displacement at the grain boundary requires that the plastic distortion tensor  $\mathbf{U}_{pl}$  to satisfy:

$$\int_C \mathbf{U}_{pl} d\mathbf{x} = 0 \quad \text{Eq. 4.2}$$

meaning that the integration of the distortion tensor  $\mathbf{U}_{pl}$  along a closed circuit  $C$  across the grain boundary nets to zero sum. By collapsing the closed circuit  $C$  into a point, Eq 4.2 can be rewritten as a more compactly form:

$$\begin{aligned} \|\mathbf{U}_{p,t}\| \times \mathbf{n}_{gb} &= 0, \text{ or} \\ \|\mathbf{U}_{p,t}\| &= \|\mathbf{U}_p(\mathbf{I} - \mathbf{n}_{gb} \otimes \mathbf{n}_{gb})\| = 0 \end{aligned} \quad \text{Eq. 4.3}$$

where  $\mathbf{U}_{p,t}$  is the tangential part of the plastic distortion tensor  $\mathbf{U}_p$ .

By differentiating Eq. 4.2, one can obtain formula similar to Eq. 4.3:

$$\|\dot{\mathbf{U}}_p(\mathbf{I} - \mathbf{n}_{gb} \otimes \mathbf{n}_{gb})\| = 0 \quad \text{Eq. 4.4}$$

where the  $\dot{\mathbf{U}}_p$  is the plastic distortion rate tensor.

Assuming that the plastic deformation is result of the shear on each individual slip system, the  $\dot{\mathbf{U}}_p$  can be related to the shear and geometry of each slip system:

$$\dot{\mathbf{U}}_p = \sum \dot{\gamma}_i \mathbf{d}_i \otimes \mathbf{n}_i \quad \text{Eq. 4.5}$$

where the  $\dot{\gamma}_i$  is the shear rate on slip system  $i$ , and  $\mathbf{d}_i$  and  $\mathbf{n}_i$  are slip direction and slip plane normal of slip system  $i$ .

If an incoming slip system triggered the activation of slip systems in both grain A and grain B, then the tangential continuity requires that net effect of all slip systems on the grain boundary to be zero. This requirement can be quantified by combining Eq. 4.4 and 4.5:

$$(\sum \dot{\gamma}^{in} \mathbf{d}^{in} \otimes \mathbf{n}^{in} + \sum \dot{\gamma}_i^A \mathbf{d}_i^A \otimes \mathbf{n}_i^A - \sum \dot{\gamma}_j^B \mathbf{d}_j^B \otimes \mathbf{n}_j^B)(\mathbf{I} - \mathbf{n}_{gb} \otimes \mathbf{n}_{gb}) = 0 \quad \text{Eq. 4.6}$$

Nonetheless, Eq. 4.6 will not hold in experiments, due to the disruption at the interface, such as residual Burgers vector, grain boundary sliding, formation of micro-cracks, etc. As a result, in this study the tangential continuity criterion used for predicting the accommodating slip systems at grain boundary is adapted by minimizing the left part of the Eq. 4.6. More specifically:

$$\min (\sum \dot{\gamma}^{in} \mathbf{d}^{in} \otimes \mathbf{n}^{in} + \sum \dot{\gamma}_i^A \mathbf{d}_i^A \otimes \mathbf{n}_i^A - \sum \dot{\gamma}_j^B \mathbf{d}_j^B \otimes \mathbf{n}_j^B)(\mathbf{I} - \mathbf{n}_{gb} \otimes \mathbf{n}_{gb}) \quad \text{Eq. 4.7}$$

### 4.3.2 Predicting accommodating slip systems using tangential continuity theory

Based on Eq. 4.7, the measured crystal orientations, the identified incoming deformation systems, and the grain boundary plane normal were used as input for a Broyden-Fletcher-Goldfarb-Shanno (BFGS) minimization routine to determine the optimum combination of accommodating deformation systems (chosen among basal  $\langle \mathbf{a} \rangle$ , prism  $\langle \mathbf{a} \rangle$ , pyramidal  $\langle \mathbf{a} \rangle$ , pyramidal  $\langle \mathbf{c} + \mathbf{a} \rangle$ , and T1 twin as listed in Table 4.2).

Table 4.2: Indices, shear direction  $\mathbf{d}$ , and plane normal  $\mathbf{n}$  of deformation systems considered for shear accommodation in the study.

type	$i$	$\mathbf{d}_i$ and $\mathbf{n}_i$
basal $\langle a \rangle$	1	$[2\bar{1}\bar{1}0] (0001)$
	2	$[\bar{1}2\bar{1}0] (0001)$
	3	$[\bar{1}\bar{1}20] (0001)$
prism $\langle a \rangle$	4	$[2\bar{1}\bar{1}0] (01\bar{1}0)$
	5	$[\bar{1}2\bar{1}0] (\bar{1}010)$
	6	$[\bar{1}\bar{1}20] (1\bar{1}00)$
	7	$[\bar{1}2\bar{1}0] (10\bar{1}1)$
	8	$[\bar{2}110] (01\bar{1}1)$
	9	$[\bar{1}\bar{1}20] (\bar{1}101)$
pyramidal $\langle a \rangle$	10	$[1\bar{2}10] (\bar{1}011)$
	11	$[2\bar{1}\bar{1}0] (0\bar{1}11)$
	12	$[11\bar{2}0] (1\bar{1}01)$
	13	$[\bar{2}113] (10\bar{1}1)$
	14	$[\bar{1}\bar{1}23] (10\bar{1}1)$
	15	$[\bar{1}\bar{1}23] (01\bar{1}1)$
pyramidal $\langle c + a \rangle$	16	$[1\bar{2}13] (01\bar{1}1)$
	17	$[1\bar{2}13] (\bar{1}101)$
	18	$[2\bar{1}\bar{1}3] (\bar{1}101)$
	19	$[2\bar{1}\bar{1}3] (\bar{1}011)$
	20	$[11\bar{2}3] (\bar{1}011)$
	21	$[11\bar{2}3] (0\bar{1}11)$
	22	$[\bar{1}2\bar{1}3] (0\bar{1}11)$
	23	$[\bar{1}2\bar{1}3] (1\bar{1}01)$
T1 twin	24	$[\bar{2}113] (1\bar{1}01)$
	25	$[\bar{1}011] (10\bar{1}2)$
	26	$[0\bar{1}11] (01\bar{1}2)$
	27	$[1\bar{1}01] (\bar{1}102)$
	28	$[10\bar{1}1] (\bar{1}012)$
	29	$[01\bar{1}1] (0\bar{1}12)$
	30	$[\bar{1}101] (1\bar{1}02)$

As the tangential continuity theory indicates that the total number of accommodating systems can be a maximum of five, there are six different accommodation scenarios that can be considered: 1) All five accommodating slip systems are in the outgoing grain. 2) Four accommodating slip systems are in the outgoing grain, while the other one is in the incoming grain (self-accommodation). 3) Three accommodating slip systems are in the outgoing grain, and the other two are in the incoming grain. 4) Two accommodating slip systems are in the outgoing grain, and the other three are in the incoming grain. 5) Only one accommodating slip system is in the outgoing grain, and the other four are in the incoming grain. 6) All five accommodating slip systems are in the incoming grain, meaning the incoming shear is relieved completely through self-accommodation. For later reference of each accommodating scenario, a short notation was used  $N^{\text{in}} + N^{\text{out}} (= 5)$ , where  $N^{\text{in}}$  and  $N^{\text{out}}$  are the number of potential accommodating systems in the incoming and outgoing grain, respectively. For example, “4+1” represents four accommodating systems in the incoming grain and one in the outgoing grain.

To quantify and highlight the differences between each slip transfer event observed or predicted, polar bar plots are used to illustrate the deformation system activity, with an example/key shown in Fig. 4.2. Each deformation system family is categorized by the specific color of the underlying sector. The six active deformation systems are represented by six polar bars, which are colored to distinguish their roles played in the shear transfer. The incoming slip system is represented in white, any self-accommodating deformation systems in the incoming grain are represented in red, and deformation systems active in the outgoing grain are represented in black. The amount of shear on each system is proportional to the length of the bar. In the example in Fig. 3, the white radar bar that represents the impinging [2-1-10](01-10) slip system (ID number 4 in table. 4.2) lies in the red prism  $\langle \mathbf{a} \rangle$  region, the red bar represents the

self-accommodating slip in the incoming grain by the pyramidal  $\langle\mathbf{a}\rangle$  system (ID number 8), and the four black bars represent accommodating slip activity in the outgoing grain, with one basal  $\langle\mathbf{a}\rangle$  system (blue background, ID 2), one pyramidal  $\langle\mathbf{a}\rangle$  system (green background, ID 11) and the other two pyramidal  $\langle\mathbf{c}+\mathbf{a}\rangle$  systems (tan background, ID number 18 and 21).

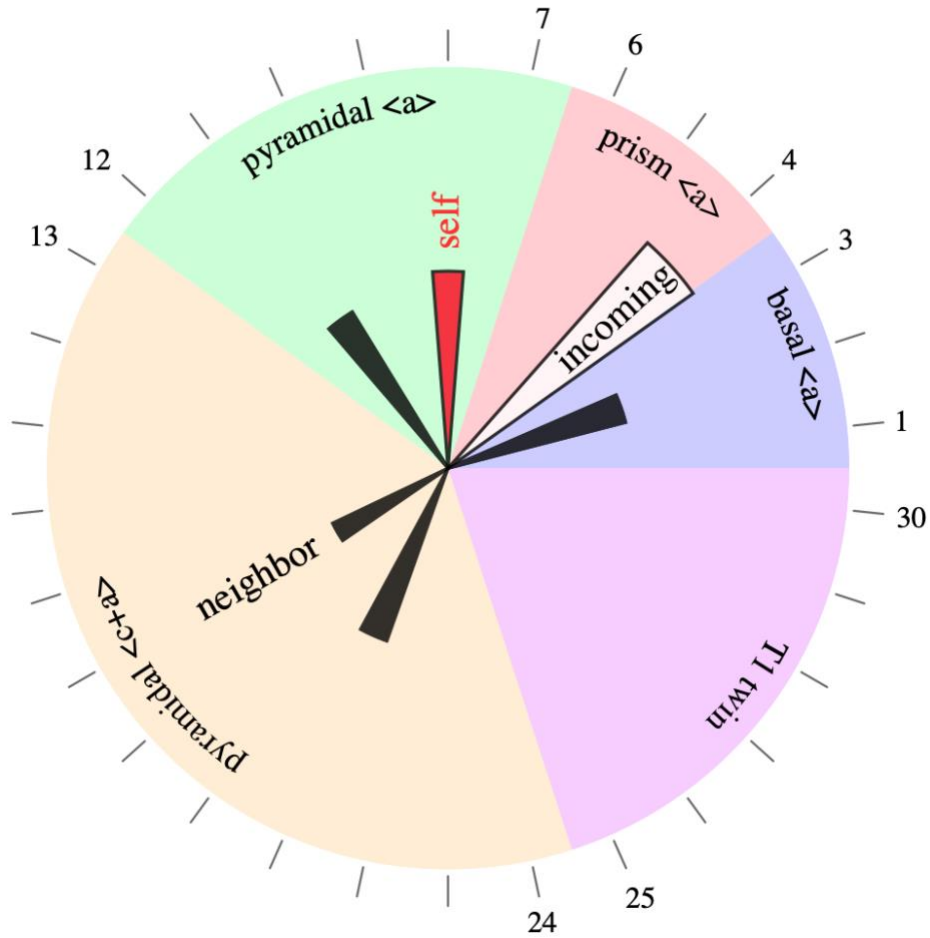


Figure 4.2: An example/key of a polar bar plot that presents all of the details of a shear transfer event and serves as key for Fig. 4.3, Fig. 4.4 and Fig. 4.5. A total of 30 ( $=3+3+6+12+6$ ) potential deformation systems, color coded by type, are represented on the outside of the figure, with the numbers indicating the specific deformation system, as listed in Table 4.2. Each bar represents an incoming or outgoing slip system, with white indicating the incoming system, black indicating outgoing systems, and red denoting accommodating systems in the incoming grain. The direction each bar points to reflects its slip system type. The length of each bar represents its relative shear<sup>11</sup>.

<sup>11</sup> The relative shear of incoming slip system is assigned to be unity. As a result the length of the white bar is constant in the radar bar plot. The relative shear of any accommodating slip system (length of the black or red bar) is then a ratio based on the relative shear on the incoming slip system.

Using Fig. 4.2 as the standard way of plotting a slip transfer event (either observation or simulation), Figures 4.3 and 4.4 illustrate the various deformation system activities predicted by the tangential continuity model for the 16 experimentally characterized single shear and 6 double shear transfer cases. In cases where at least two self-accommodating deformation systems are allowed (*i.e.*, “5+0”, “4+1”, “3+2”, and “2+3”), tangential continuity can be fulfilled by those two systems alone. This trend can be observed in the second column of Fig. 4.3 and 4.4, as each inset has two red bars with the same length, indicating complete self-accommodation maximizes tangential continuity at the grain boundary. In fact, the tangential continuity optimization predicts identical accommodation for all those categories (*i.e.*, “5+0”, “4+1”, “3+2”, and “2+3”), hence, they all are collected in the second column in Fig. 4.3 and 4.4. In the present study no instances of self-accommodation were observed. (We note that limited self-accommodation has been observed in a recent study in the same  $\alpha$ -Ti material used in this study, but not without major outgoing grain accommodation [141]).

A closer analysis reveals that exclusive self-accommodation can happen under two scenarios in the tangential continuity model. If the incoming slip is on the basal plane, then slip by the remaining two basal Burgers vectors is able to compensate for the incoming shape change (not observed in Figs. 4.3 and 4.4). Similarly, any other (than basal) incoming shear can be accommodated by two additional slip systems that share the same Burgers vector with the incoming slip system but operate on different (here pyramidal) slip planes. This geometric peculiarity that slip on three (specific) systems can (locally) result in zero net shape change will exist for the hexagonal lattices examined here, as well as for fcc and bcc, but might not be generalizable to other (lower symmetry) crystal structures. Nonetheless, the stress driving the incoming slip system will resolve to an opposing stress on at least one of the two required self-

accommodating systems. Therefore, it is concluded that the tangential continuity solution, which does not account for externally imposed stress, is correct from a purely kinematic stand-point, but unlikely to be physically realized.

Among the physically more sensible predictions of “1+4” and “0+5”, the latter predictions agree<sup>12</sup> much more often with the observed accommodating deformation system(s). Specifically, for the 16 single shear accommodation cases, the 1+4 condition only predicted the correct outgoing system in 3 cases, while using the 0+5 condition led to a correct prediction in 7 out of the 16 cases. For the double shear accommodation cases, while the 0+5 condition had slightly more success than the 1+2 condition, which was unable to correctly predict any accommodating systems, the model still incorrectly predicted both accommodating slip systems in five of the six double accommodation cases, and in the two cases 17 and 18, only correctly predicted one of the two accommodating deformation systems. This lack of agreement results from the tangential continuity theory lacking a unique solution in its pure kinematic form. To overcome the non-uniqueness, other biases such as imposed stress and total number of dislocations are necessary to be added as constraints to the solution.

---

<sup>12</sup> Here a prediction is considered correct if the most active predicted deformation systems agree with the observation and any other systems fall below half of the primary shear magnitude.

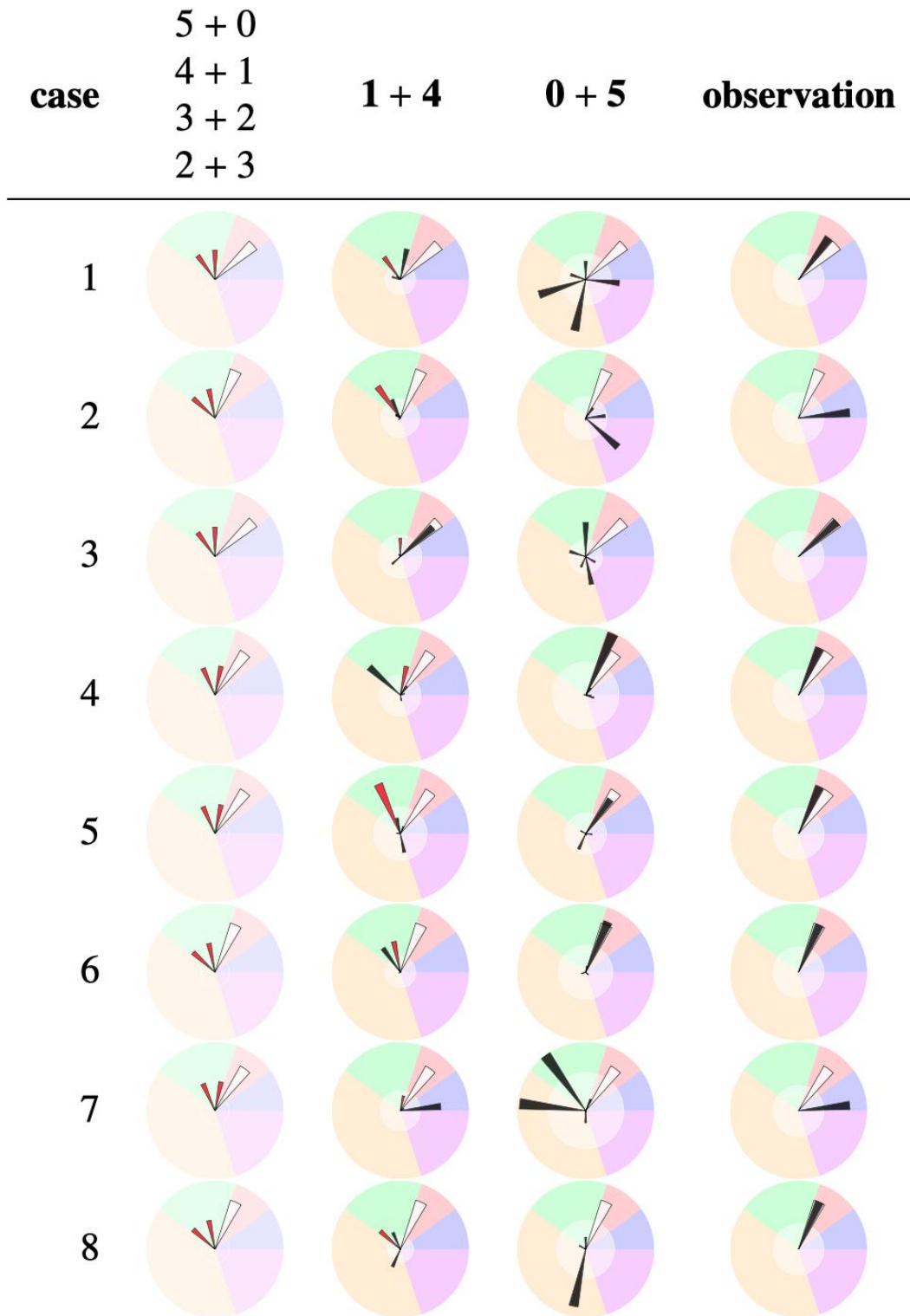


Figure 4.3: Radar bar plots showing tangential continuity predictions compared to observations of 16 single slip accommodation cases.

Figure 4.3 (cont'd)

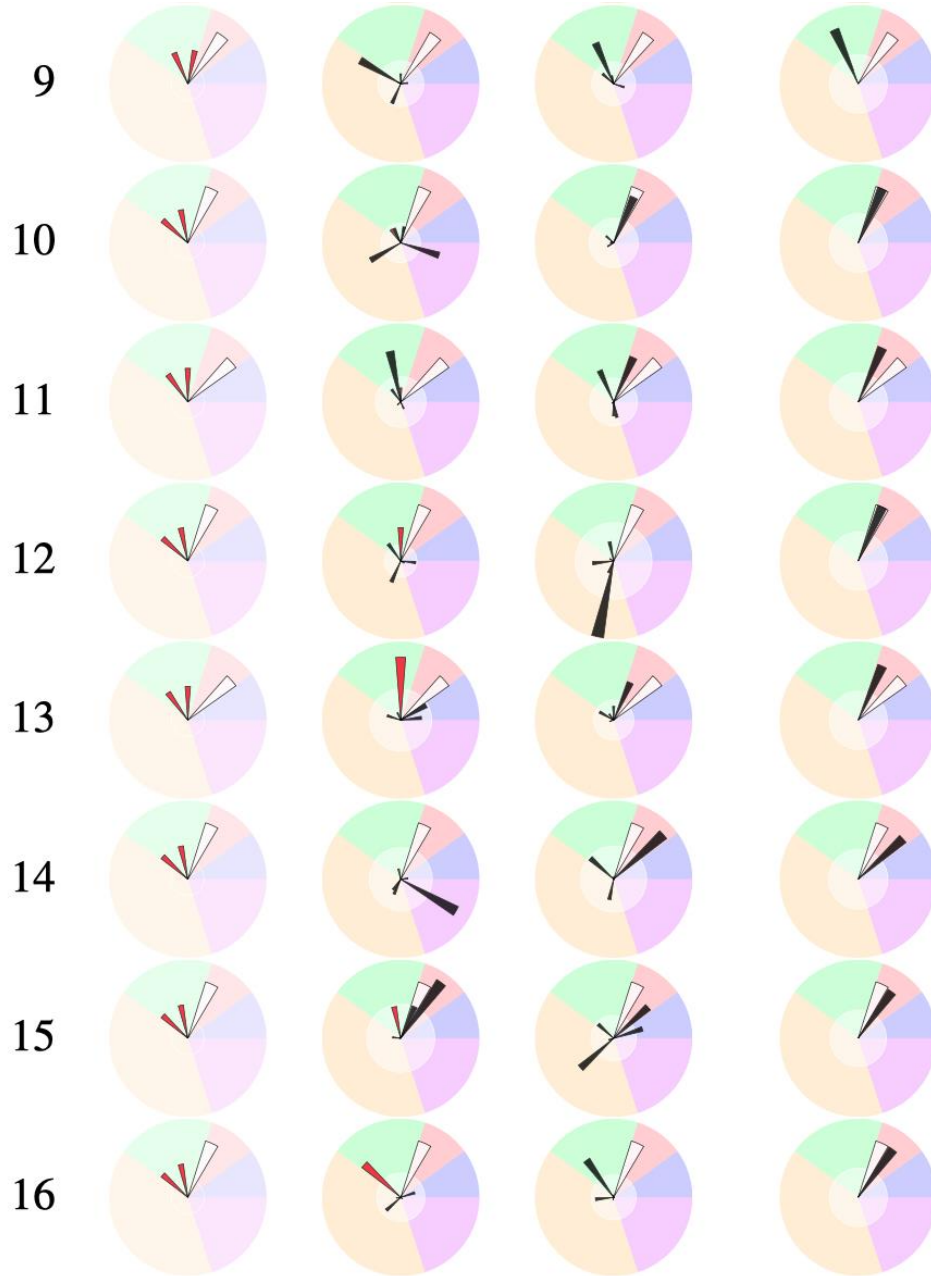


Figure 4.3: The left column indicates that the predictions are identical (and never match the observations) when at least two self-accommodating systems are allowed. The center two columns show the response changing for less than two self-accommodating systems. “0+5” predictions are most accurate, with about half agreeing with observations.

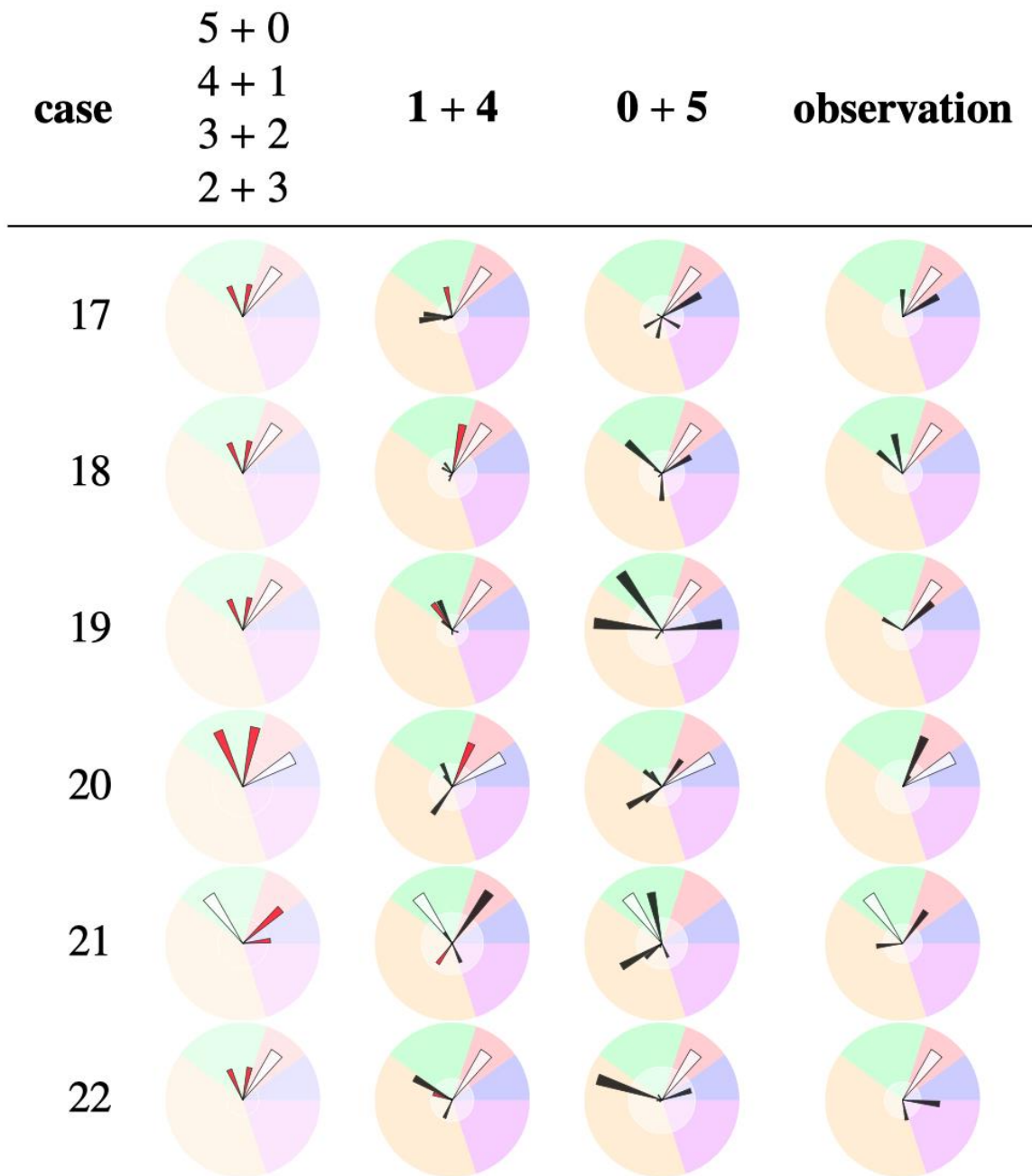


Figure 4.4: Similar plot as Fig. 4.3 but for double shear accommodation cases. Tangential continuity model predictions are shown in columns 2-4 and observations are presented in column 5. Across all six cases, none of the three distinct self-accommodation conditions result in predictions that agree with the observed accommodating shear systems.

## 4.4. A new iterative stress relief (ISR) model based on slip accommodation observations

### 4.4.1 Algorithm of the iterative stress relief model

Due to the lack of consideration of an applied external stress in the tangential continuity model, a new approach is proposed that takes into account the combination of external stress and the stress that results from the local deformation band development. This new model, which is termed the “iterative stress relief model”, uses an iterative approach that can be used to predict (at most three) accommodating deformation systems based on a known impinging system and the global stress state. Contrary to the tangential continuity model, the reduction of the residual Burgers vector in the grain boundary (in other words the continuity of Burgers vector) serves as a decisive criterion in the proposed enhanced model.

It is hypothesized that the accommodation of the impinging shear on a deformation system with normal  $\mathbf{n}^{\text{in}}$  and direction  $\mathbf{d}^{\text{in}}$  is afforded by multiple accommodating deformation systems in both the incoming and the outgoing grains. These three outgoing deformation systems are indexed by  $i = 1, 2, 3$  and termed “primary”, “secondary”, “tertiary” in the following. Their activity is determined by the respective local stress state, which is approximated as a weighted superposition of the normalized externally applied stress  $\sigma_0 = \sigma_{\text{global}}/|\sigma_{\text{global}}|$  and the sum of impinging,  $\mathbf{d}^{\text{in}} \otimes \mathbf{n}^{\text{in}}$ , and accommodating kinematics,  $\mathbf{d}_i \otimes \mathbf{n}_i$ , multiplied by a normalized stiffness tensor  $\mathbb{C}_0 = \mathbb{C}/\|(\mathbb{C}_{\text{in}} + \mathbb{C}_{\text{out}})\mathbf{d}^{\text{in}} \otimes \mathbf{n}^{\text{in}}\|$  with an appropriate<sup>13</sup> choice for the stiffness  $\mathbb{C}$  to keep the local and global kinematic influence at the same magnitude. The  $\mathbb{C}_{\text{in}}$  and  $\mathbb{C}_{\text{out}}$  are acquired by rotating  $\mathbb{C}$  using the incoming and outgoing crystal orientation, respectively.

---

<sup>13</sup> To reflect hexagonal titanium, values of  $\mathbb{C}$  are  $C_{11} = 162.4$ ,  $C_{12} = 92.0$ ,  $C_{13} = 69.0$ ,  $C_{33} = 180$ ,  $C_{44} = 49.7$ ,  $C_{66} = 35.2$ , all in the units of GPa, were chosen based on [132].

The stress state assumed to drive the activity of the primary outgoing deformation system,  $\sigma_1$ , is treated as a binary mixture:

$$\sigma_1 = \alpha \mathbb{C}_0(\mathbf{d}^{\text{in}} \otimes \mathbf{n}^{\text{in}}) + (1 - \alpha)\sigma_0 \quad \text{Eq. 4.8}$$

of the global stress  $\sigma_0$  and only the impinging activity, where the weighting factor  $\alpha$  varies between zero and one and specifies the relative importance of the global applied stress and the local pile-up stresses. The primary outgoing deformation system is selected as that with the maximum resolved shear stress normalized by the respective critical resolved shear stress (CRSS):

$$\text{RSS}_1 = \arg \max_i |\sigma_1 : (\mathbf{d}_i \otimes \mathbf{n}_i)| / \text{CRSS}_i \quad \text{Eq. 4.9}$$

where  $\mathbf{d}_i$  and  $\mathbf{n}_i$  characterize possible outgoing deformation systems. The secondary deformation system is identified using the same approach, but includes the modification to the stress resulting from the primary accommodating system:

$$\sigma_2(c_1) = \alpha \mathbb{C}_0(\mathbf{d}^{\text{in}} \otimes \mathbf{n}^{\text{in}} - c_1 \mathbf{d}_1 \otimes \mathbf{n}_1) + (1 - \alpha)\sigma_0,$$

$$\text{or } \sigma_2(c_1) = \sigma_1 - \alpha \mathbb{C}_0 c_1 (\mathbf{d}_1 \otimes \mathbf{n}_1) \quad \text{Eq. 4.10}$$

$$\text{RSS}_2 = \arg \max_i |\sigma_2(c_1) : (\mathbf{d}_i \otimes \mathbf{n}_i)| / \text{CRSS}_i \quad \text{Eq. 4.11}$$

The activity  $c_1$  of the primary accommodating system is found by expressing the incoming Burgers vector  $\mathbf{b}^{\text{in}}$  in a basis spanned by the (known) primary accommodating Burgers vector direction  $\mathbf{b}_1$ , the (to be determined) secondary Burgers vector direction  $\mathbf{b}_2$ , and their cross product:

$$\mathbf{b}^{\text{in}} = c_1 \mathbf{b}_1 + c_2 \mathbf{b}_2 + c_3 \mathbf{b}_1 \times \mathbf{b}_2 \quad \text{Eq. 4.12}$$

which is motivated by the assumption that the accommodating shear minimizes the residual Burgers vector in grain boundary. The same procedure is repeated for the tertiary accommodating system, *i.e.*, the driving stress is given by:

$$\sigma_3(c_1, c_2) = \sigma_2(c_1) - \alpha C_0 c_2 (\mathbf{d}_2 \otimes \mathbf{n}_2) \quad \text{Eq. 4.13}$$

the activities  $c_1$  and  $c_2$  depend on the choice of the tertiary system:

$$\mathbf{b}^{\text{in}} = c_1 \mathbf{b}_1 + c_2 \mathbf{b}_2 + c_3 \mathbf{b}_3 \quad \text{Eq. 4.14}$$

and the tertiary outgoing deformation system again maximizes the normalized resolved shear stress:

$$\text{RSS}_2 = \arg \max_i |\sigma_2(c_1) : (\mathbf{d}_i \otimes \mathbf{n}_i)| / \text{CRSS}_i \quad \text{Eq. 4.15}$$

Any impinging Burgers vector can be fully accommodated with the three identified outgoing deformation systems (*i.e.*, any vector can be expressed by the combination of any three non-coplanar vectors, provided that the number of dislocations involved in the transmission event is large enough to properly approximate arbitrary fractions). Nevertheless, the activity on some of these systems may be very small, and in order to facilitate comparison with experimental results, it is reasonable to include a threshold  $\beta$  of relative activity such that only secondary and tertiary systems for which

$$c_i \geq \beta c_1 \quad \text{Eq. 4.16}$$

are considered to be observable, with  $\beta$  ranging from 0 to 1.

#### 4.4.2 Predicting accommodating deformation systems using the iterative stress relief model

To assess its robustness, the iterative stress relief model was used to predict the accommodating deformation systems and their relative activity for the investigated 22 grain boundaries. Predications were considered “correct” if the set of observed deformation system(s) fully agrees with the predicted ones irrespective of potential deviations of relative activity. In the new model proposed in section 4.4.1, there are multiple parameters (the weighting factor  $\alpha$ , the activity threshold  $\beta$ , and the ratios of prism  $\langle\mathbf{a}\rangle$ , pyramidal  $\langle\mathbf{a}\rangle$ , pyramidal  $\langle\mathbf{c}+\mathbf{a}\rangle$ , and T1 twin relative to basal slip) that could influence the predicted slip systems and/or the relative shear on each slip systems. The determination of the optimized parameters will be outlined in the discussion (section 4.6). In this section, the optimized parameters that generate the largest number of correct predictions in all the 22 cases, were used in the new model.

The iterative stress relief model was evaluated on its ability to predict the type of outgoing deformation systems and the amount of accommodating shear on the predicted deformation systems. In the same manner as the tangential continuity results were presented in Figs. 4.3 and 4.4 using polar bar plots, the predicted deformation systems and relative shear of all 22 cases are presented in Fig. 4.5 for single and double accommodation. On these figures, the white discs represent the threshold  $\beta$  for secondary or tertiary activity. Thus, any bar extending beyond the white disc represents what will be considered an active deformation system. Fig. 4.5 shows that in all 16 single accommodation shear transfer cases, only the most active predicted deformation system exceeds the activity threshold  $\beta$ ; these most active systems are always identical to those experimentally observed and their activity generally falls within 10% of the observed amount of shear, with a worst case deviation of 25%.

The iterative stress relief model is somewhat less accurate in predicting the double shear accommodation events, as shown in Fig. 4.5, where both outgoing deformation systems were correctly predicted in only four out of the six cases (with the secondary system in case 4 falling below the activity threshold in both the prediction and the experimental observation). The predicted magnitude of shear in the four correct cases deviates from the experimental observations by between about 10% to 25%. In general, the predictions projected by the iterative stress relief model agree very well with the observations in both single and double accommodation scenarios.

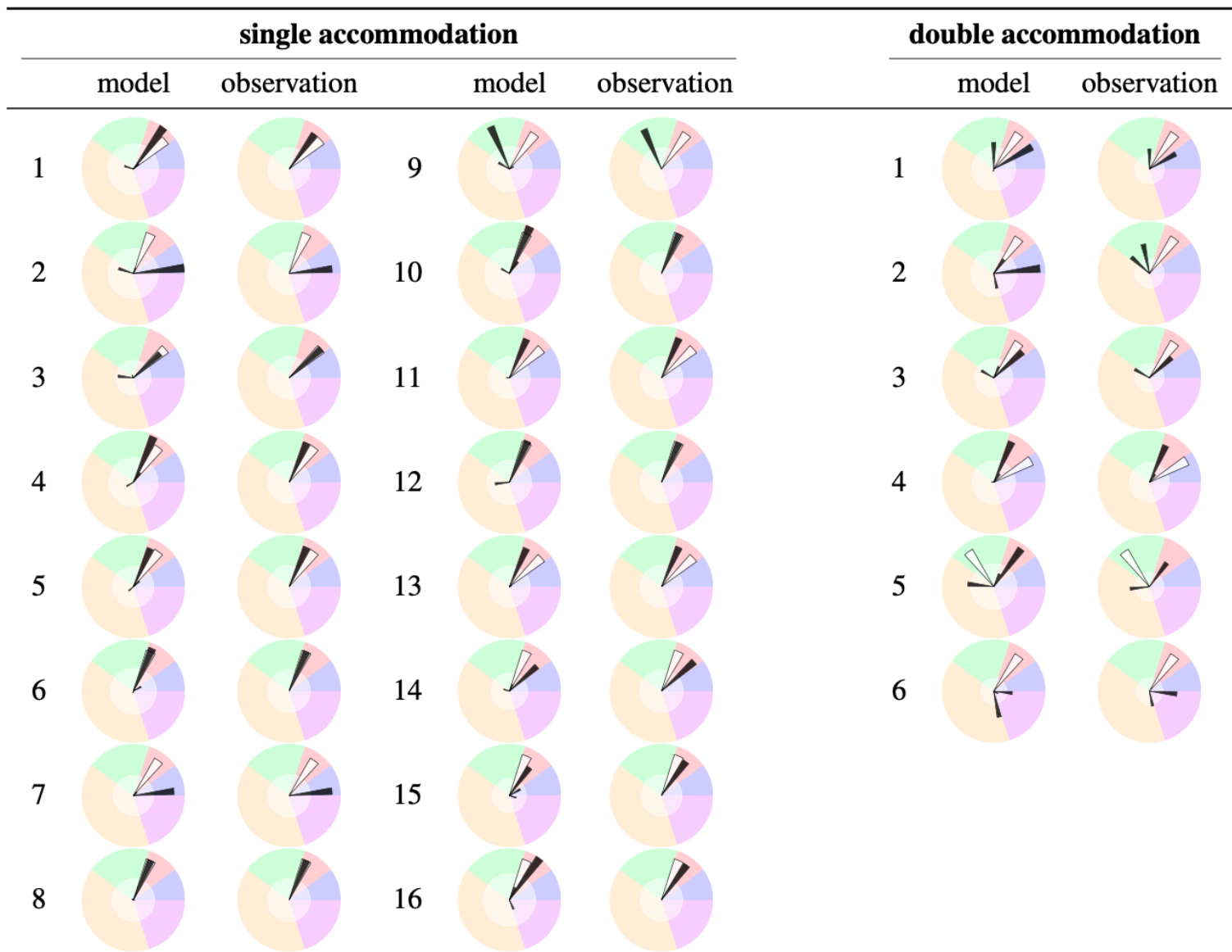


Figure 4.5: The new (ISR) model predictions compared to observations for 16 single and 6 double accommodation cases.

## 4.5 Discussion

### 4.5.1 Optimizing the variables in the iterative stress relief model

In this stress-driven shear accommodation model, the weighting factor  $\alpha$ , the activity threshold  $\beta$ , and the CRSS ratios of prism  $\langle\mathbf{a}\rangle$ , pyramidal  $\langle\mathbf{a}\rangle$ , pyramidal  $\langle\mathbf{c}+\mathbf{a}\rangle$ , and T1 twin relative to basal slip are essential to the model. Varying each of the five parameters may change the predicted slip systems and/or the relative shear on each slip systems. The resulting six-dimensional parameter space was evaluated on a grid that is centered at the points given in Table 4.3 and is spaced linearly along  $\alpha$  and logarithmically along the other five dimensions.  $\alpha$  varies between 0 and 1, while the five other values each span an order of magnitude. Each grid dimension is discretized into ten equidistant intervals, resulting in 116 grid points being evaluated.

Figure 4.6 presents the fraction of correctly identified cases (shades of gray) on the  $\alpha$ - $\beta$  plane of the parameter space at one set of specific CRSS ratios based on the literature [136-140] and constitutes the center point within the four-dimensional subspace spanned by the CRSS ratios (Table 4.3). The highest fraction of correct predictions (20 out of 22) occurs at  $\alpha \approx 0.5$  and  $\beta \approx 0.5$ . The fact that  $\alpha = 0.5$  produces the most accurate predictions of the model implies that the importance of both global stress state and the local kinematics and kinetics. Moreover, in the cases studied in this chapter, the influences of both global and local stress are well balanced as each is accounted for half of the overall stress tensor. Nonetheless, the optimal  $\alpha$  may vary (deviate from 0.5) if the imposed global stress state changed or the crystal structure/texture of the material is different.

Table 4.3: The center point of the search range used in the parameter optimization of the iterative stress relief model. The six parameters correspond to the six dimensions of the optimization.

	$\alpha$	$\beta$	CRSS ratio relative to basal $\langle a \rangle$ slip			
			prism $\langle a \rangle$	pyramidal $\langle a \rangle$	pyramidal $\langle c + a \rangle$	T1 twin
center point	0.5	1/3	1	1.3	3	3

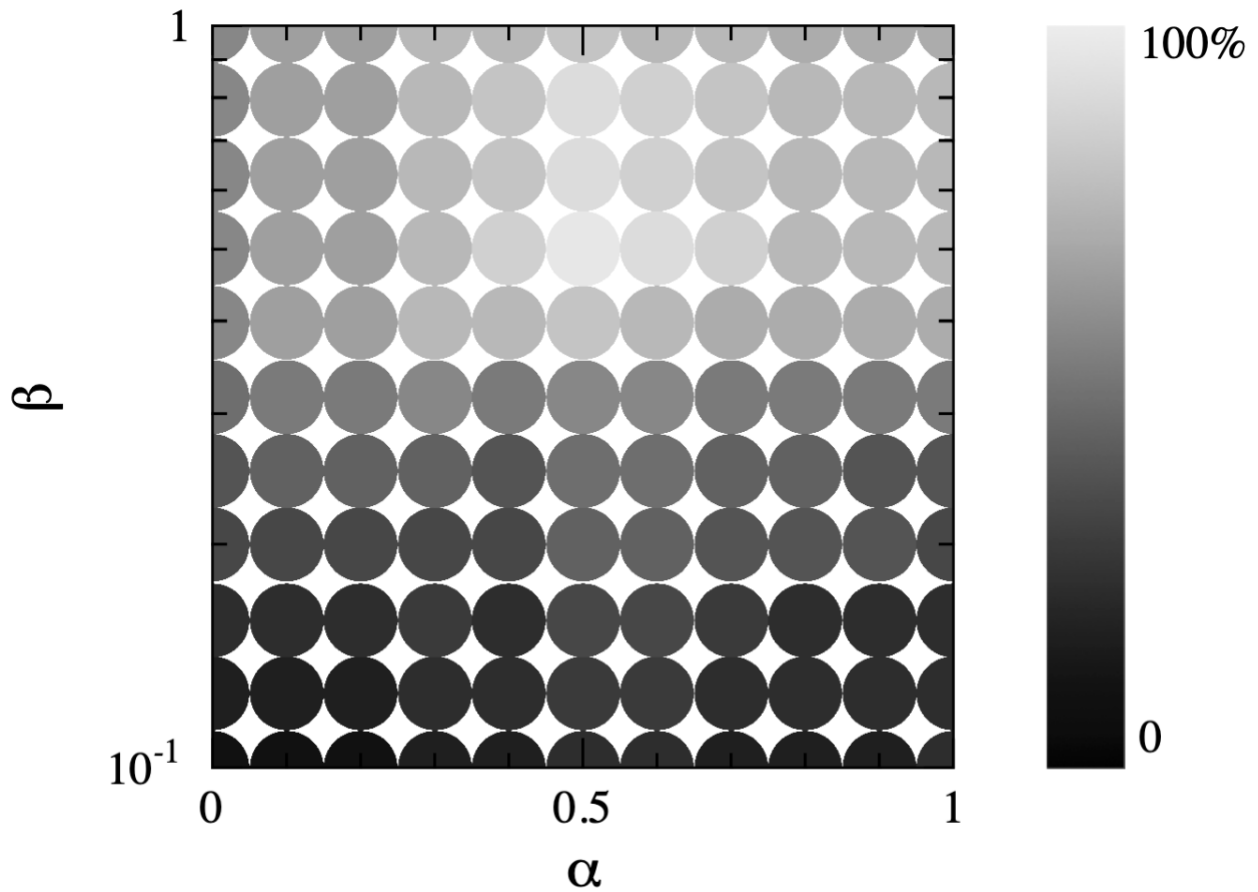


Figure 4.6: Heat map showing the variation in the accuracy of the iterative stress relief model as a function of both  $\alpha$  and  $\beta$ . The accuracy of the model, shown in grey scale, is quantified using the fraction of correct predictions compared to observations. Lighter gray indicates higher accuracy of the model.

With the two coordinates of the six parameter space fixed at their optima ( $\alpha = 0.5$  and  $\beta = 0.5$ ), the influence of CRSS ratios was evaluated within the range specified in Table 4.3. This evaluation demonstrated that within the CRSS ratio ranges of basal  $\langle \mathbf{a} \rangle$  : prism  $\langle \mathbf{a} \rangle$  : pyramidal  $\langle \mathbf{a} \rangle$  : pyramidal  $\langle \mathbf{c} + \mathbf{a} \rangle$  : T1 twin = 1.0 : (0.8–1.0) : (1.0–1.3) : (1.6 – 9.5) : (3.0 – 9.5) the fraction of correctly predicted outcomes remains at 20 out of 22. While the ranges of optimal CRSS ratios for prism  $\langle \mathbf{a} \rangle$  and pyramidal  $\langle \mathbf{a} \rangle$  are fairly narrow, the CRSS ratios of pyramidal  $\langle \mathbf{c} + \mathbf{a} \rangle$  and T1 twin only need to exceed 1.6 and 3.0, respectively, to maintain the highest prediction accuracy. Figure 4.7 illustrates the sensitivity of the correctly predicted fraction with respect to the CRSS ratios of prism  $\langle \mathbf{a} \rangle$  and pyramidal  $\langle \mathbf{a} \rangle$  as a heat map, which is a two-dimensional cut at  $\alpha = 0.5$ ,  $\beta = 0.5$ , and CRSS ratios of pyramidal  $\langle \mathbf{c} + \mathbf{a} \rangle = 1.6$  and T1 twin = 3.0.

After determining the optimal values of all the six parameters, the sensitivity of  $\alpha$  and the CRSS ratios of prism  $\langle \mathbf{a} \rangle$ , pyramidal  $\langle \mathbf{a} \rangle$ , and pyramidal  $\langle \mathbf{c} + \mathbf{a} \rangle$  can be visualized and understood separately, in Fig. 4.8, by varying one parameter at a time while keeping other parameters at their optimal values. The upper left plot of Fig. 4.8 shows that  $\alpha$  influences the accuracy of the model. At left and right end of the plot, where  $\alpha = 0$  and 1, the model predicts with the worst accuracy. The active slip systems predicted by considering only global or local stress state is incorrect in about 40% of the cases. In the upper right plot of Fig. 4.8, the optimal value of CRSS ratio of prismatic  $\langle \mathbf{a} \rangle$  is found at 1.0, as expected. The accuracy of the model drops significantly as the CRSS ratio of prismatic  $\langle \mathbf{a} \rangle$  increases beyond 1.0, but only drops slightly as CRSS ratio of prismatic  $\langle \mathbf{a} \rangle$  decreases below 1.0. A reverse trend can be observed for the CRSS pyramidal  $\langle \mathbf{a} \rangle$  value in lower left plot of Fig. 4.8. The influence of CRSS ratio of

pyramidal  $\langle c+a \rangle$  on the model is shown in lower right plot of Fig. 4.8, where the model remains accurate when CRSS ratio of pyramidal  $\langle c+a \rangle$  is greater than 1.3.

In general, the optimized CRSS ratios of all of the deformation systems agrees well with the literature. By visualizing how the CRSS ratio of individual slip systems influence the model, the sensitivity of the model to each CRSS ratio was quantified.

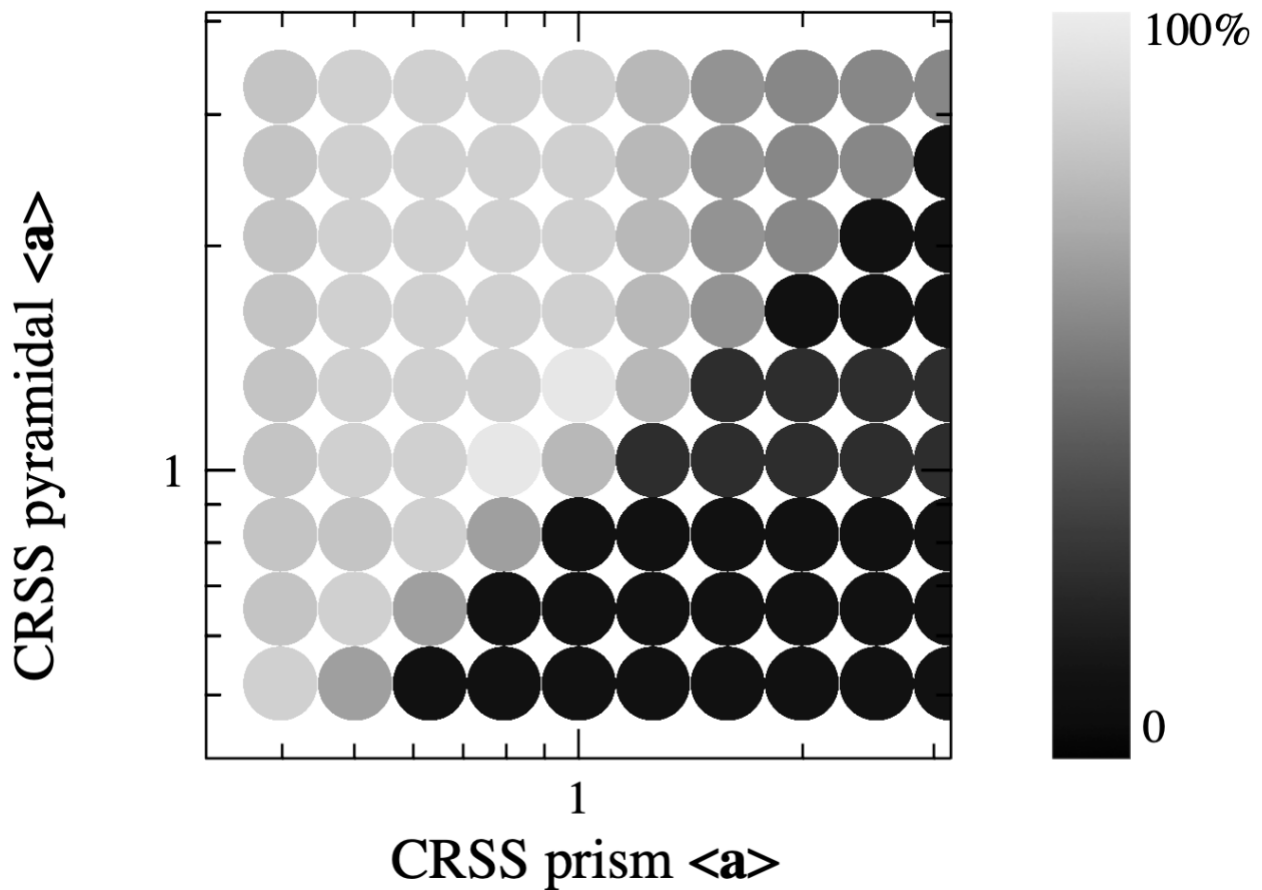


Figure 4.7: Heat map showing the accuracy variation of the iterative stress relief model as a function of CRSS ratios prism  $\langle a \rangle$  and pyramidal  $\langle a \rangle$ . The accuracy of the model is quantified using the fraction of correct predictions compared to observations. Lighter gray suggests higher accuracy of the model at that point.

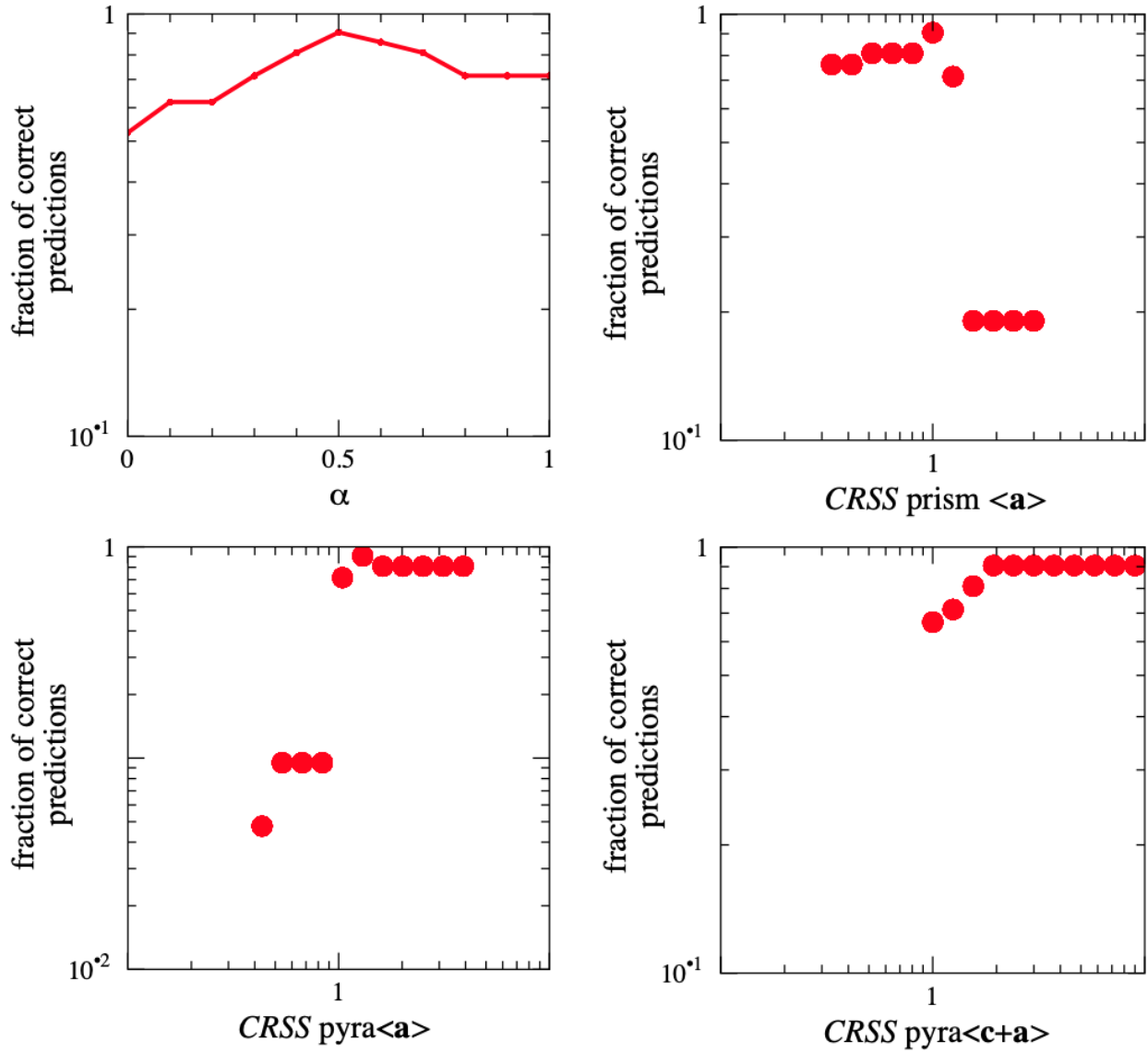


Figure 4.8: Plots of the model accuracy as a function of four parameters,  $\alpha$  and CRSS ratios of prism  $\langle \mathbf{a} \rangle$ , pyramidal  $\langle \mathbf{a} \rangle$ , and pyramidal  $\langle \mathbf{c} + \mathbf{a} \rangle$  in the model. The model accuracy is quantified using the fraction of correct predictions.

## 4.5.2 Limitations of the iterative stress relief model

### 4.5.2.1 Slip band blocking and threshold stress

In addition to the correlated single and double shear accommodation events, three other types of interactions were observed: (1) apparent slip band blocking, (2) non-correlated slip activity, and (3) activation of localized plume-like/non-planar shear accommodation in the neighboring grain. In this latter case, electron channeling contrast imaging (ECCI) has shown very limited shear accommodation, often in the form of a non-descript cloud of dislocations S. Han and M. A. Crimp [142], which was not a focus of the present study.<sup>14</sup> Since the iterative stress relief model does not consider a stress threshold for excluding (any) accommodating deformation activity, none of these three additionally observed scenarios are presently predictable. A critical stress must be developed by the incoming dislocation slip band impinging on the boundary in order to nucleate and propagate accommodating dislocation or twinning shear in the neighboring grain. Clearly, reaching such a critical stress will be a function of the relative orientations of the two grains in the context of the applied global stress. Furthermore, the stress developed by an incoming slip band will also be a function of the number of dislocations in that particular slip band (i.e., the size of the pile-up). It is also likely that the stress necessary to nucleate a grain boundary dislocation source will be controlled in some manner by the atomic level structure of the particular grain boundary. At this point, however, such factors are not incorporated into the model.

---

<sup>14</sup> In such scenario, those cloud of dislocations in the vicinity of grain boundary are usually scattered and do not form a clear slip trace on the sample surface, as a result the current AFM based slip trace analysis has very limited capability of studying this type of slip accommodation at grain boundary.

#### 4.5.2.2 Shear accommodation by lattice rotation

Recent observations by F. Di Gioacchino *et al.* [142] on  $L1_0$  TiAl indicate that slip accommodation across grain boundaries depends on the continuity of the overall resulting kinematics. Specifically, they showed that, in cases where well-aligned deformation systems (in the sense of Livingston and Chalmers [5] or Luster and Morris [11]) are not easily available in the outgoing grain, the imposed kinematics can still be realized through spatially coordinated slip within the ‘plume’ of stress, such that a volume of rotated lattice orientation (formation of a sub-grain) accommodates the imposed shear. Due to the fact that the final kinematics are a combination of shearing and lattice rotation, any slip prediction based solely on shear kinematics, such as those strictly based on the Luster and Morris approach, will disfavor such accommodation. In contrast, the approach by Livingston and Chalmers, as well as classical crystal plasticity, will likely correctly predict such an accommodation, provided that the affected volume contains a sufficient density of suitable dislocations and the resolved stress favors their activity over that of others. This latter provision might be one reason why this particular accommodation mechanism appears to be rarely reported compared to activity of well-aligned deformation systems. The iterative stress relief model presented here selects accommodating deformation systems based on a combination of resolved stress (similar to the approach of Livingston and Chalmers) and a balancing of the incoming Burgers vector with multiple outgoing Burgers vector contributions. What effect the latter aspect of the iterative stress relief model will have on correctly predicting lattice rotation-dominated accommodation events is presently unclear and could not be rigorously evaluated to date since, in the present study of hexagonal  $\alpha$ -Ti, no such events were observed.

### 4.5.2.3 Influence of grain boundary trace angle $\psi$ on shear transfer

Another factor that the iterative stress relief model does not consider is the angle  $\psi$  between slip plane traces on the grain boundary. It is quite natural to rationalize that a smaller  $\psi$  would facilitate the shear transfer process, since it would be easier for a dislocation to climb or cross-slip from the impinging slip plane to the accommodating plane at the grain boundary. The role of  $\psi$  has often been ignored in slip transfer studies, due to the difficulty in measuring this angle from surface information alone. In the present study, FIB cross-sections were used in a number of cases to determine the grain boundary inclination and estimate  $\psi$  (Fig. 2.4). Based on the measured grain boundary inclination,  $\psi$  can be determined from:

$$\cos\psi = \frac{(\mathbf{n}^{\text{in}} \times \mathbf{n}^{\text{GB}}) \cdot (\mathbf{n}^{\text{out}} \times \mathbf{n}^{\text{GB}})}{\|(\mathbf{n}^{\text{in}} \times \mathbf{n}^{\text{GB}})\| \|(\mathbf{n}^{\text{out}} \times \mathbf{n}^{\text{GB}})\|} \quad \text{Eq. 4.17}$$

where  $\mathbf{n}^{\text{in}}$  and  $\mathbf{n}^{\text{out}}$  are the slip plane normal of the impinging and responding slip systems, and  $\mathbf{n}^{\text{GB}}$  is the normal of the grain boundary plane which can be obtained from the grain boundary inclination  $\psi$ .

The angle  $\psi$  was determined for two of the single accommodation cases and for five of the six double accommodation cases (excluding the twinning case). The results in Table 4.1 range from  $8^\circ$  to  $54^\circ$ , indicating that shear transfer will occur between slip planes with large angles. This is in agreement with the  $\psi$  range measured by Lee et al. [10], which spans from  $7^\circ$  to  $60^\circ$ , and slightly larger than that observed for the primary slip systems Han and Crimp [141], who observed  $\psi$  ranging from  $5^\circ$  to  $42^\circ$ . Given this wide range of  $\psi$  in all slip transfer cases, it is difficult or even impossible to determine a threshold above which the slip transfer will not occur and use such a threshold in a model. Consequently, at present the angle  $\psi$  has not been incorporated in the model, as only including  $\varphi$  and  $\kappa$  is sufficient to accurately describe and quantify the slip transfer geometry and activity.

### 4.5.3 Application of the ISR model to other materials and loading conditions

The iterative stress relief model has been applied successfully in predicting shear accommodation in commercially pure hexagonal titanium, with the adjustable model parameters of CRSS ratios,  $\alpha$ , and  $\beta$  optimized solely on the experimental observations.

The optimized values of the CRSS ratios are expected to be different if the model were applied to a different material, but should be insensitive to variations in the material microstructure, e.g., changes in grain size or texture. Nevertheless, as the material work hardens, the CRSS ratios have the potential to evolve, as the slip system-specific work hardening can be variable (and dependent on grain orientation). In the present study, we have only considered small strains, but one could envision extending the approach to evolving CRSS ratios. Likewise, one would expect changes in alloy chemistry, in particular in non-cubic systems such as the hexagonal Ti considered here, to change the CRSS ratios (as is well known in Ti [140, 143-145]). Regardless, we would anticipate the model to still be effective following optimization of the CRSS ratios. It is worth noting that the CRSS ratio optimization carried out in the present study resulted in ratios that fell well within the variations reported in the literature for commercial purity titanium. In some non-cubic materials, such as titanium, it is difficult to accurately measure the CRSS ratios. The approach outlined here has the potential to be used as an indirect approach to determining these ratios. Overall, it is reasonable to expect strong predictions from the model if accurate CRSS ratios are available.

The model predictions were found to be optimal for intermediate values of  $\alpha$  and  $\beta$  and were found to be minimally sensitive around these optima. It is difficult to imagine that material changes, such as lattice structure or alloy chemistry, as well as loading conditions, will substantially alter this optimal range, as it is reasonable to expect that both global and local stress

will play a role in dictating the shear accommodation process. Nonetheless, this should be explored experimentally in future study.

At present, the iterative stress relief model was applied to a single phase materials, i.e., only to grain boundaries. It can be envisioned that the same underlying mechanisms control shear across phase boundaries. While beyond the scope of this present study, it would be relatively simple to apply the iterative stress relief model to inter-phase shear transfer, with the definitions of slip systems, their orientations, and their CRSS ratios simply defined for the phases on either side of a boundary. With such a generalization, the model could be applied to a wide range of microstructures.

While the present study has examined a simple tensile external loading condition, the superposition principle would apply under any global stress condition. Nevertheless, it is not clear at the present time how different loading conditions will affect the  $\alpha$  and  $\beta$  parameters, if at all. Overall, it would be reasonable to expect that the iterative stress relief model should be flexible over a broad range of materials, boundary types, and loading conditions.

#### **4.6 Conclusions**

In light of previous studies of grain boundary slip transfer and in order to develop a model that is capable of resolving shear accommodation from multiple deformation systems, a unified model that incorporates the continuity of Burgers vector in the grain boundary and the modification of the impinging stress tensor iteratively is proposed to solve the shear accommodation via multiple deformation systems. This iterative stress relief model is able to predict outgoing deformation systems and their relative shear, based on grain orientations, the incoming deformation system, and the critical resolved shear stress ratios as input. The accuracy

of this model was tested by comparing predictions with observations of slip transfers in  $\alpha$ -titanium quantified using orientation informed slip trace analysis and quantitative AFM. The comparison shows that the iterative stress relief model is accurate when used in the prediction of correlated shear transfer, e.g., in single and double accommodation cases, and even in one slip-to-twinning event. Optimization of this model was accomplished by blending the local and global stress state using a factor  $\alpha$  and balancing the critical resolved shear stress ratios to best match the experimental observations. The optimized value of the blending factor  $\alpha$  was found to be around 0.5, suggesting comparable influences from the global stress tensor and the local shear stress developed from the incoming slip band. The optimized critical resolved shear stress ratios were determined as basal  $\langle \mathbf{a} \rangle$  : prism  $\langle \mathbf{a} \rangle$  : pyramidal  $\langle \mathbf{a} \rangle$  : pyramidal  $\langle \mathbf{c} + \mathbf{a} \rangle$  : T1 twin = 1.0 : (0.8–1.0) : (1.0–1.3) : (1.6 – 9.5) : (3.0 – 9.5). The sensitivity of the model to each CRSS ratio was studied. Nonetheless, this model is limited in that it does not effectively deal with cases where direct shear transfer is not observed, as it assumes there is always sufficient stress in the incoming slip band to initiate outgoing accommodation. Consequently, it is not possible to judge the likelihood of whether the outgoing grain will nucleate an outgoing slip band or not.

## CHAPTER 5 CONCLUSIONS

In the present work, improvements in the understanding of heterogeneous deformation in hexagonal  $\alpha$ -Ti were achieved in three ways. Experimentally, the crystal orientation informed bi-crystal nanoindentation and the quantitative slip trace analysis have been improved and adapted to quantitatively study the influence of a grain boundary on the development of heterogeneous deformation. Coupled to the experimental work, CPFÉ simulations of both single and bi-crystal nanoindentations were carried out, the results of which were analyzed for insights into the individual slip systems. Based on the knowledge obtained experimentally and from simulations, a new model (iterative stress relief model) was proposed to resolve the shear accommodation of multiple deformation systems.

By studying how nanoindentation surface topography was affected by the presence of a grain boundary, a novel methodology for quantifying the resistance of the grain boundary to slip transfer was developed. Both single and bi-crystal models were built using a carefully crafted procedure based on experimentally gathered data. As a result, the comparisons between CPFÉ simulations of nanoindentations and experiments are meaningful, which makes the evaluation of the current CPFÉ model possible.

The slip trace analysis approach for identifying active slip systems was improved by adding the surface profile of each slip band quantified using AFM. This improvement allows a more accurate determination of slip systems with the additional slip plane inclination information acquired in AFM. Furthermore, with quantitative AFM analysis, the shear on each slip band can be obtained. This information is critical in the analysis of shear accommodation/transfer at grain boundary.

The new iterative stress relief model was developed by integrating the influence of global and local stress state change, continuity of Burgers vector at grain boundary, and the CRSS ratios. This model is highly accurate when applied to predict experimentally observed slip transfer events. The significance of the new model resides in its capability of predicting shear accommodation involving multiple deformation systems, as well as the relative shear on each of these slip systems.

Critical conclusions of the current study are summarized in the following, more detailed conclusions are given at the end of each chapter:

- Single crystal indents in the grain with same orientation and bi-crystal indents near the same grain boundary were highly reproducible. Therefore, quantitative study of individual grain and/or grain boundary can be achieved by comparing indentations under different conditions.
- A procedure for assessing grain boundary resistance to slip transfer was established. The procedure includes measuring surface topographies of single and bi-crystal indentations and comparing the two topographies to quantify the difference.
- A CPFÉ model was built to simulate both single and bi-crystal indentations. The parameters in the model were based on experimental measurements, such as crystal orientation, maximum depth of the indent, the grain boundary inclination, and the distance between indent and grain boundary. Such a carefully calibrated model allows direct comparison between simulated indent topographies and experimental measurements.
- The grain boundary resistance to slip transfer in the CPFÉ simulations is lower than that found experimentally, as indicated by the fact that the simulations display larger amount

of indent topographies across the grain boundary, indicating a weaker grain boundary in the model.

- The slip trace analysis identification of slip system was improved by adding the inclination of the slip band and quantifying the shear in each slip band using AFM measurement. This enhancement is critical as it ensures the identification of slip system unambiguously and enables more detailed analysis of shear accommodation/transfer at grain boundary.
- An iterative stress relief model was proposed to predict the shear accommodation of multiple slip systems at grain boundary. The new model was tested along with the tangential continuity theory using same experimental data set. The iterative stress relief model predicts the accommodating slip systems at grain boundary with high accuracy, making it much more robust than the tangential continuity model.
- Optimization of the model parameters showed that in order to correctly quantify the heterogenous deformation near a grain boundary it is necessary to account for both global stress and local kinematics. The optimized CRSS ratios of the model was determined to be basal  $\langle \mathbf{a} \rangle$  : prism  $\langle \mathbf{a} \rangle$  : pyramidal  $\langle \mathbf{a} \rangle$  : pyramidal  $\langle \mathbf{c} + \mathbf{a} \rangle$  : T1 twin = 1.0 : (0.8–1.0) : (1.0–1.3) : (1.6 – 9.5) : (3.0 – 9.5).

## CHAPTER 6 OUTLOOK

The ultimate goal of characterizing the evolution of the full stress and strain field in the grain boundary vicinity remains to be fulfilled. Nonetheless, the work in this dissertation provides a significant step forward in the understanding and quantification of plastic deformation in the grain boundary vicinity via both novel experimental methods and simulations.

The establishment of the reproducibility of both single and bi-crystal indentation topographies allows further assessment of individual grain and grain boundary mechanical/microstructural properties. It will hopefully help to decrease the time for characterizing mechanical properties of material as indentation is a relatively fast testing methods compared to others.

The comparison of slip system activities between experiment and CPFÉ simulations in bi-crystal nanoindentation were not completed in this work. More accurate comparison requires characterization of individual dislocations using ECCI or TEM. Future efforts can be devoted to study the activity of individual dislocations and compare the results with CPFÉ or dislocations dynamics (DD) simulations. This comparison will help develop an understanding of the link between the development of macro heterogenous strain fields and the movement of individual dislocation.

The newly developed iterative stress relief model is very successful in predicting active slip systems in the grain boundary vicinity. By implementing this grain boundary sensitive model into the CPFÉ method, the prediction of activities of slip systems in the grain boundary vicinity may be improved.

It will also be interesting to test the newly developed iterative stress relief model with material of different texture and/or crystal structure. It is not unlikely that the optimized parameters used in  $\alpha$ -Ti do not make accurate predictions in a new material system. Nonetheless, the success of the iterative stress relief model suggests that the consideration of only kinematic and partial kinetic in an iterative algorithm is sufficient to resolve the shear accommodation at grain boundary.

The present study of slip band development in polycrystals excluded those slip band that were blocked by the grain boundary. With the improved slip trace analysis, AFM measurement and high resolution EBSD, it may be possible to evaluate the small lattice rotation in the outgoing grain where no obvious slip band is present. Cross slip which is more common at larger strain is another potential topic for future investigation. The quantitative slip trace analysis with high resolution map for AFM might be the solution to identify the role of cross slip in grain boundary shear accommodation.

## **APPENDICES**

## APPENDIX A: AFM DATA OF INDENT TOPOGRAPHIES IN 3D

The AFM data of indent topographies  $a$  and  $b$  in 3D are shown below.

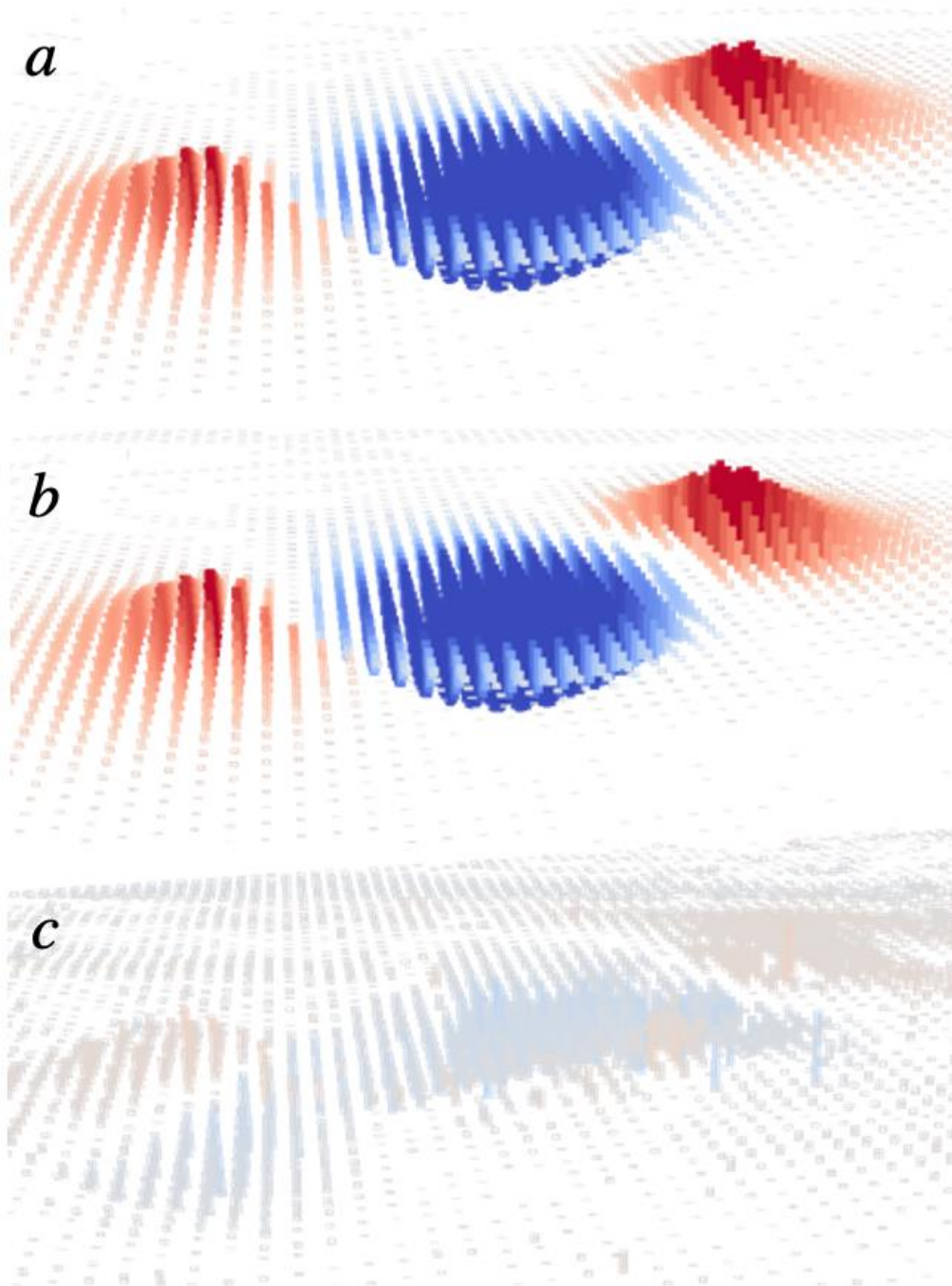


Figure A1: The AFM data of indent topographies  $a$  and  $b$  in 3D. a) Topography of indent  $a$ . b) Topography of indent  $b$ . c) The differences in topographies of  $a$  and  $b$ .

## APPENDIX B: SEM AND AFM MEASUREMENTS OF ALL SLIP ACCOMMODATION CASES

### CASES

Secondary electron images of the 16 single slip accommodation cases and 6 double slip accommodation cases studied in the Chapter 4 followed by the AFM measurements of the 6 double slip accommodation cases.

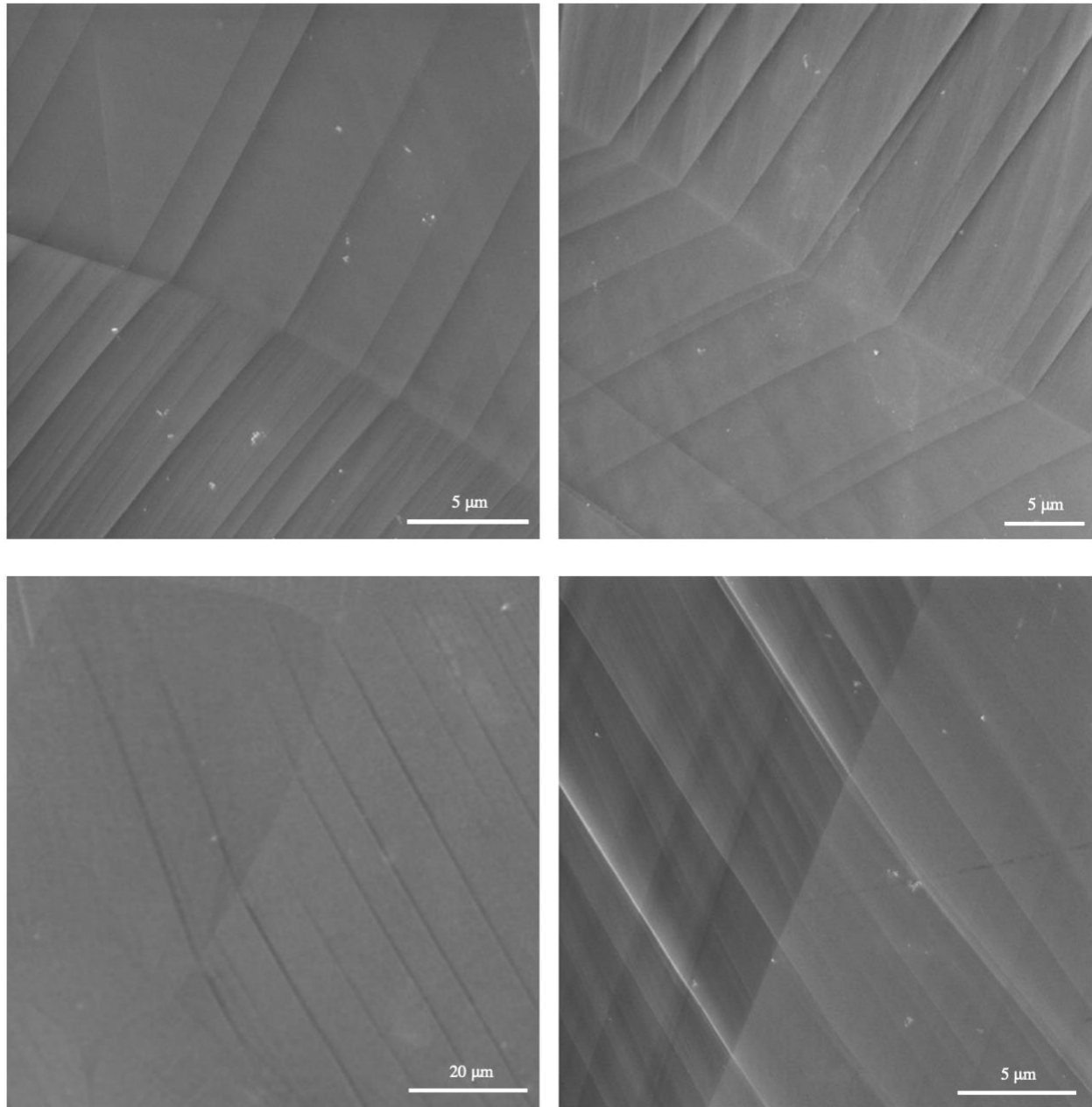


Figure B1: SEM images of single slip accommodation cases 1-4.

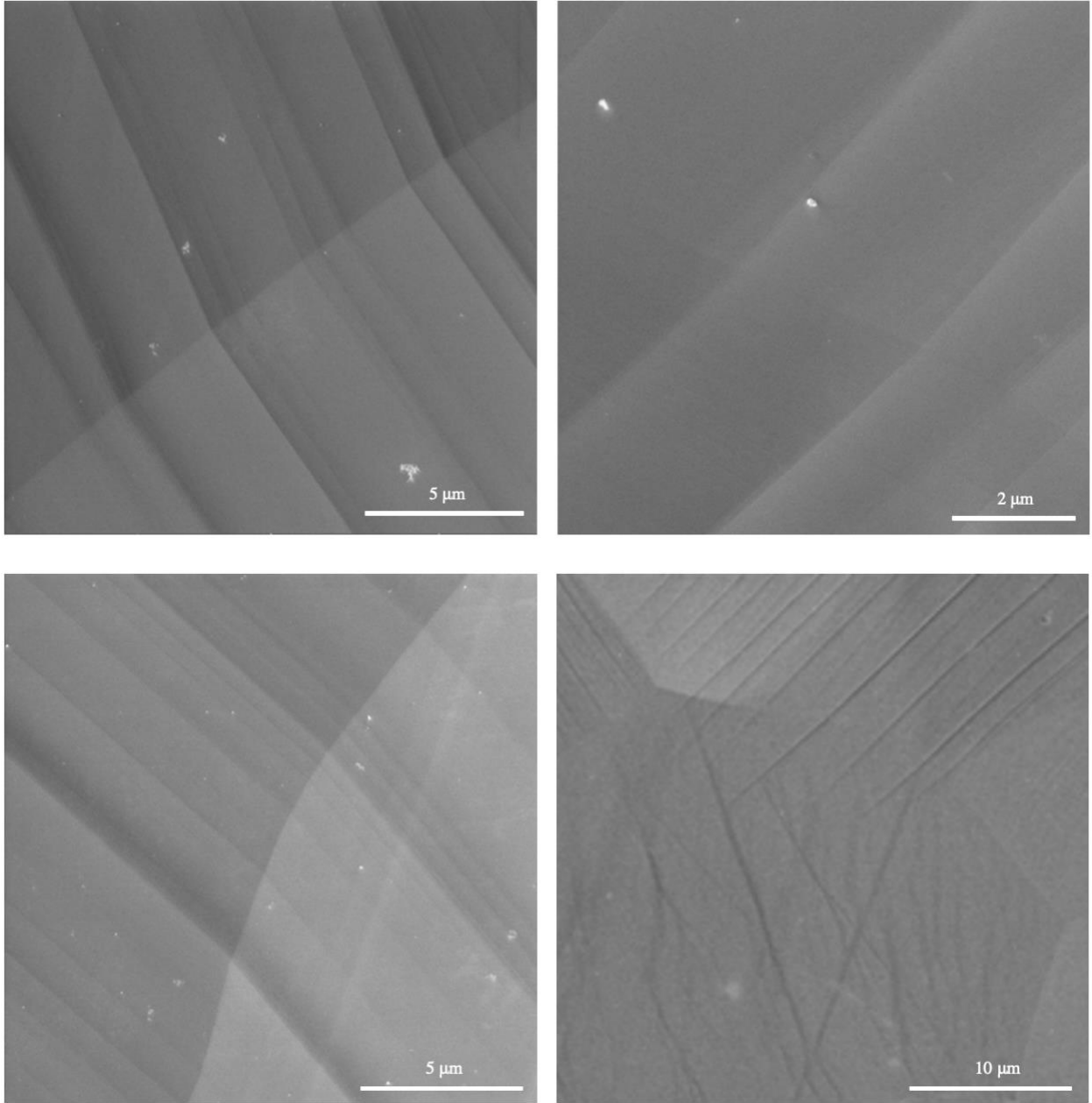


Figure B2: SEM images of single slip accommodation cases 5-8.

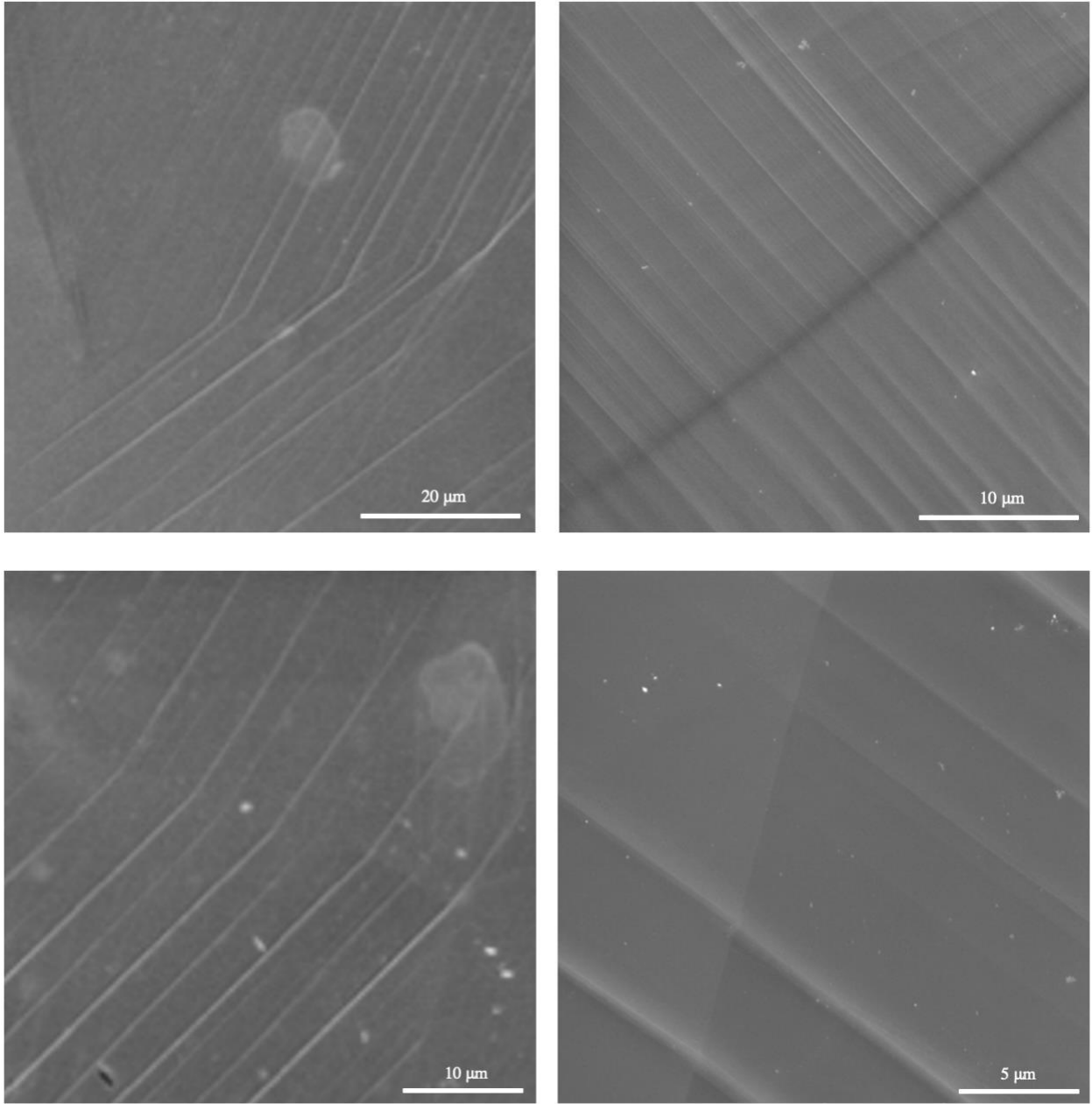


Figure B3: SEM images of single slip accommodation cases 9-12.

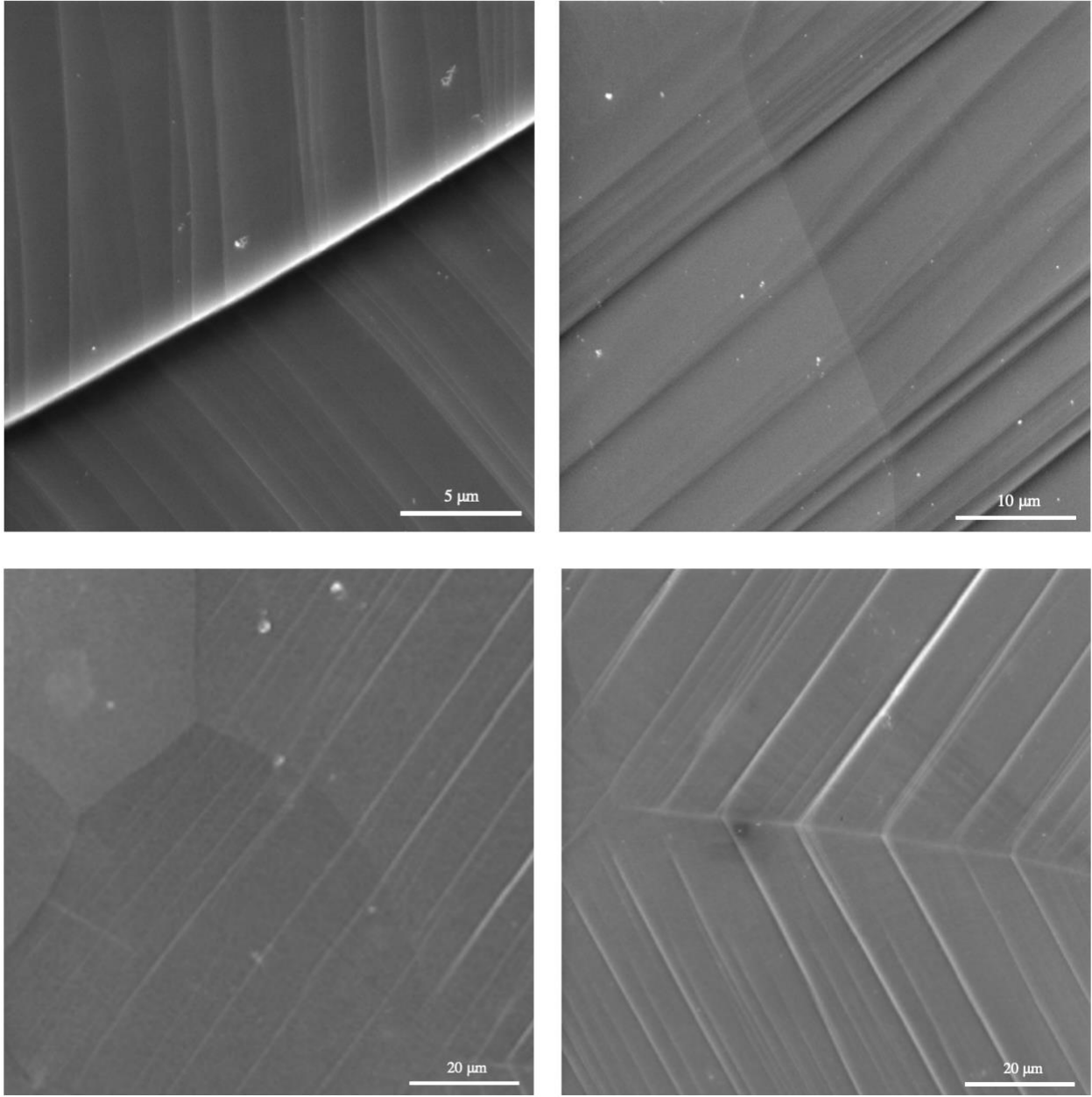


Figure B4: SEM images of single slip accommodation cases 13-16

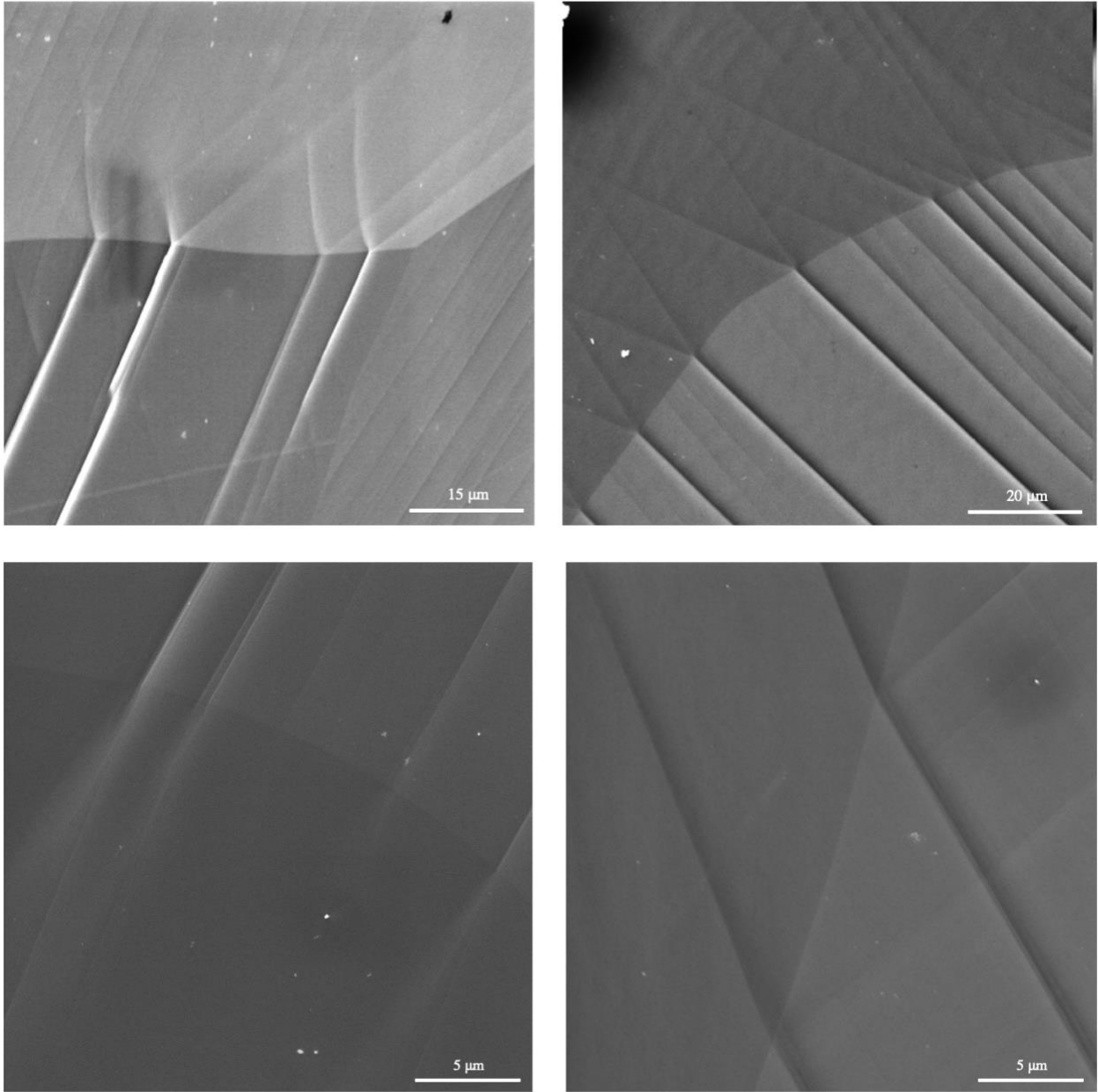


Figure B5: SEM images of double slip accommodation cases 1-4

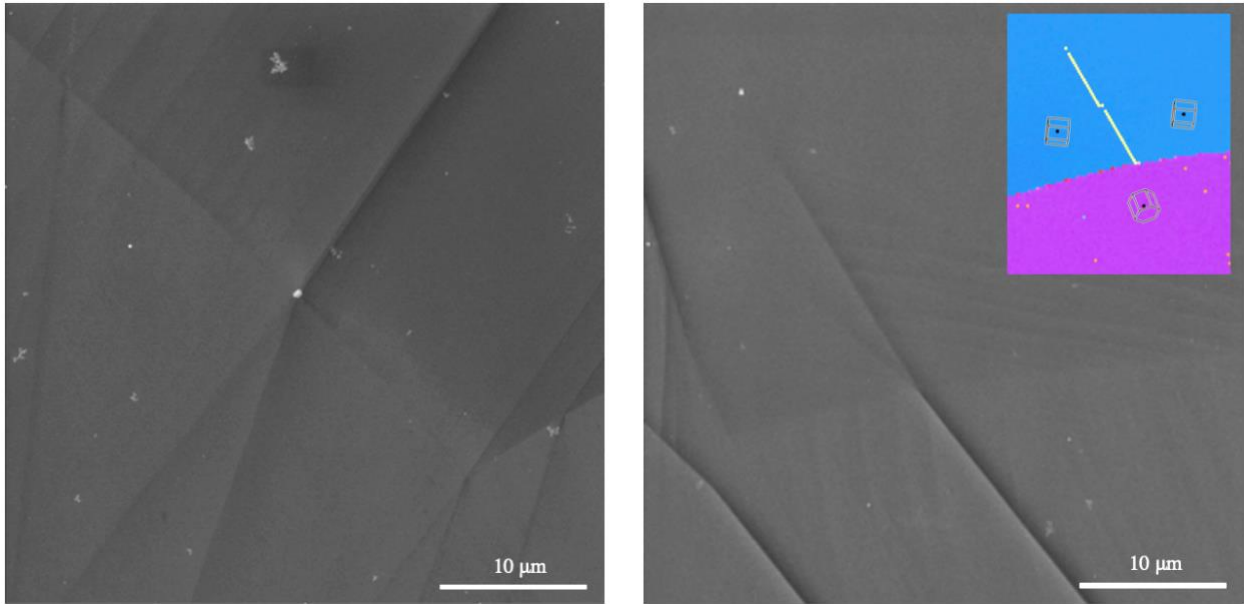


Figure B6: SEM images of double slip accommodation cases 5 and 6 (Note that there is a twinning involved shown as yellow dotted line in the EBSD map inset, in the accommodating deformation system in case 6).

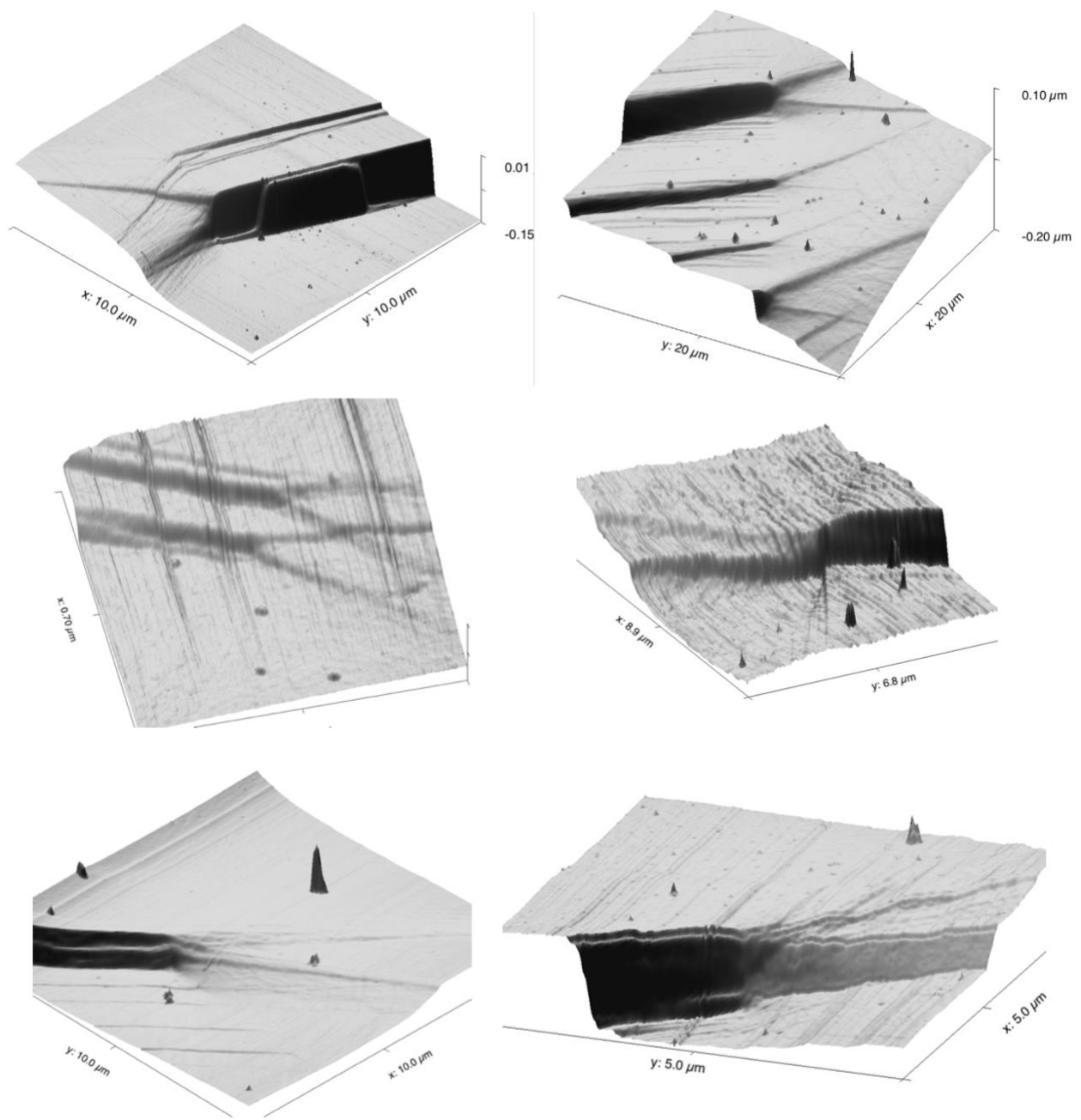


Figure B7: AFM measurements of double slip accommodation cases 1-6.

## **BIBLIOGRAPHY**

## BIBLIOGRAPHY

- [1] G.I. Taylor, Plastic strain in metals, *Journal of the Institute of Metals* 62 (1938) 307-324.
- [2] U.F. Kocks, Polyslip in polycrystals, *Acta Metallurgica* 6 (1958) 85-94. doi:10.1016/0001-6160(58)90117-2.
- [3] J.P. Hirth and J. Lothe, *Theory of Dislocations*. NY, USA: John Wiley & Sons, 1981.
- [4] T. R. Bieler, P. Eisenlohr, F. Roters, D. Kumar, D. E. Mason, M. A. Crimp, D. Raabe, The role of heterogeneous deformation on damage nucleation at grain boundaries in single phase metals, *International Journal of Plasticity* 25 (2009) 1655–1683. doi:10.1016/j.ijplas.2008.09.002.
- [5] J. D. Livingston, B. Chalmers, Multiple slip in bicrystal deformation, *Acta Metallurgica* 5 (1957) 322–327. doi:10.1016/0001-6160(57) 90044- 5.
- [6] Z. Shen, R. H. Wagoner, W. A. T. Clark, Dislocation Pile-up and Grain Boundary Interactions in 304 Stainless Steel, *Scripta Metallurgica* 20 (1986) 921–926. doi:10.1016/0036-9748(86)90467-9.
- [7] Z. Shen, R. H. Wagoner, W. A. T. Clark, Dislocation and grain boundary interactions in metals, *Acta Metallurgica* 36 (1988), 3231-3242. doi:10.1016/0001-6160(88)90058-2.
- [8] W. A. T. Clark, R. H. Wagoner, Z. Y. Shen, T. C. Lee, I. M. Robertson, H. K. Birnbaum, On the criteria for slip transmission across interfaces in polycrystals, *Scripta Metallurgica et Materialia* 26 (1992) 203–206. doi:10.1016/0956- 716X(92)90173- C.
- [9] T. C. Lee, I. M. Robertson, H. K. Birnbaum, Prediction of slip transfer mechanisms across grain boundaries, *Scripta Metallurgica* 23 (1989) 799–803. doi:10.1016/0036-9748(89)90534- 6.
- [10] T. C. Lee, I. M. Robertson, H. K. Birnbaum, An in situ transmission electron microscope deformation study of the slip transfer mechanisms in metals, *Metallurgical Transactions A* 21A (1990) 2437-2447. doi: 10.1007/BF02646988.
- [11] J. Luster, J. M. Morris, Compatibility of deformation in two-phase Ti-Al alloys: Dependence on microstructure and orientation relation- ships, *Metallurgical and Materials Transactions A26* (1995) 1745–1756. doi:10.1007/BF02670762.
- [12] C. Fressengeas, M. V. Upadhyay, A continuum model for slip transfer at grain boundaries, *Advanced Modeling and Simulation in Engineering Sciences* 7 (2020). doi:10.1186/s40323-020-00145-6.

- [13] C. Fressengeas, V. Taupin, M. Upadhyay, L. Capolungo, Tangential continuity of elastic/plastic curvature and strain at interfaces, *International Journal of Solids and Structures* 49 (2012) 2660–2667. doi:10.1016/j.ijsolstr.2012.05.020.
- [14] C. Fressengeas, B. Beausir, Tangential continuity of the curvature tensor at grain boundaries underpins disclination density determination from spatially mapped orientation data, *International Journal of Solids and Structures* 156-157 (2019) 210-215. doi:10.1016/j.ijsolstr.2018.08.015.
- [15] C. Fressengeas, V. Taupin, L. Capolungo, Continuous modeling of the structure of symmetric tilt boundaries, *International Journal of Solids and Structures* 51 (2014) 1434-1441. doi: 10.1016/j.ijsolstr.2013.12.031.
- [16] T. Richeton, G. F. Wang, C. Fressengeas, Continuity constraints at interfaces and their consequences on the work hardening of metal-matrix composites, *Journal of Mechanics and Physics of Solids* 59 (2011) 2023-2043. doi: 10.1016/j.jmps.2011.07.006.
- [17] V. Taupin, L. Capolungo, C. Fressengeas, M. Upadhyay, B. Beausir, A mesoscopic theory of dislocation and disclination fields for grain boundary-mediated crystal plasticity, *International Journal of Solids and Structures* 71 (2015) 277-290. doi:10.1016/j.ijsolstr.2015.06.031.
- [18] V. Taupin, J. Chevy, C. Fressengeas, Effects of grain-to-grain interactions on shear strain localization in Al-Cu-Li rolled sheets, *International Journal of Solids and Structures* 99 (2016) 71-81. doi:10.1016/j.ijsolstr.2016.07.023.
- [19] A. Acharya, Jump condition for GND evolution as a constraint on slip transmission at grain boundaries, *Philosophical Magazine* 87 (2007) 1349–1359. doi:10.1080/14786430600951537.
- [20] W. C. Oliver, G. M. Pharr, An improved technique for determining hardness and elastic modulus using load and displacement sensing indentation experiments, *Journal of Materials Research* 7 (1992) 1564-1583. doi:10.1557/JMR.1992.1564.
- [21] W. C. Oliver, G. M. Pharr, Measurement of hardness and elastic modulus by instrumented indentation: advances in understanding and refinements to methodology, *Journal of Materials Research* 19 (2004) 3-20. doi:10.1557/jmr.2004.19.1.3.
- [22] Ya. M. Soifer, A. Verdyan, M. Kazakevich, E. Rabkin, Nanohardness of copper in the vicinity of grain boundaries, *Scripta Materialia* 47 (2002) 799-804. doi:10.1016/S1359-6462(02)00284-1.
- [23] P. C. Wo and A. H. W. Ngan, Investigation of slip transmission behavior across grain boundaries in polycrystalline Ni<sub>3</sub>Al using nanoindentation, *Journal of Materials Research* 19 (2004) 189-201. doi:10.1557/jmr.2004.19.1.189.

- [24] M. G. Wang, A. H. W. Ngan, Indentation strain burst phenomenon induced by grain boundaries in niobium, *Journal of Materials Research* 19 (2004) 2478-2486. doi:10.1557/JMR.2004.0316.
- [25] W. A. Soer, K. E. Aifantis, J. Th. M. De Hosson, Incipient plasticity during nanoindentation at grain boundaries in body-centered cubic metals, *Acta Materialia* 53 (2005) 4665-4676. doi:10.1016/j.actamat.2005.07.001.
- [26] T. B. Britton, D. Randman, A. J. Wilkinson, Nanoindentation study of slip transfer phenomenon at grain boundaries, *Journal of Materials Research* 24 (2009) 607-615. doi:10.1557/JMR.2009.0088.
- [27] S. R. Kalidindi, S. J. Vachhani, Mechanical characterization of grain boundaries using nanoindentation, *Current Opinion in Solid State and Materials Science* 18 (2014) 196-204. doi:10.1016/j.cossms.2014.05.002.
- [28] S. J. Vachhani, R. D. Doherty, S. R. Kalidindi, Studies of grain boundaries regions in deformed polycrystalline aluminum using spherical nanoindentation, *International Journal of Plasticity* 81 (2016) 87-101. doi:10.1016/j.ijplas.2016.01.001.
- [29] S. J. Vachhani, R. D. Doherty, S. R. Kalidindi, Effect of the continuous stiffness measurement on the mechanical properties extracted using spherical nanoindentation, *Acta Materialia* 61 (2013) 3744-3751. doi:10.1016/j.actamat.2013.03.005.
- [30] S. R. Kalidindi, S. Pathak, Determination of the effective zero-point and the extraction of spherical nanoindentation stress-strain curves, *Acta Materialia* 56 (2008) 3523-3532. doi:10.1016/j.actamat.2008.03.036.
- [31] S. Pathak, J. Shaffer, S. R. Kalidindi, Determination of an effective zero-point and extraction of indentation stress-strain curves without the continuous stiffness measurement signal, *Scripta Materialia* 60 (2009) 439-442. doi:10.1016/j.scriptamat.2008.11.028.
- [32] S. Pathak, D. Stojakovic, S. R. Kalidindi, Measurement of the local mechanical properties in polycrystalline samples using spherical nanoindentation and orientation imaging microscopy, *Acta Materialia*, 57 (2009) 3020-3028. doi:10.1016/j.actamat.2009.03.008.
- [33] B.R. Donohue, A. Ambrus, S. R. Kalidindi, Critical evaluation of the indentation data analysis methods for the extraction of isotropic uniaxial mechanical properties using finite element models, *Acta Materialia* 60 (2012) 3943-3952. doi:10.1016/j.actamat.2012.03.034.
- [34] R. E. Hook, J. P. Hirth, The deformation behavior of isoaxial bicrystals of Fe-3%Si, *Acta Metallurgica* 15 (1967) 535-551. doi:10.1016/0001-6160(67)90087-9.
- [35] R. E. Hook, J. P. Hirth, The deformation behavior of non-isoaxial bicrystals of Fe-3%Si, *Acta Metallurgica* 15 (1967) 1099-1110. doi:10.1016/0001-6160(67)90383-5.

- [36] C. Rey, A. Zaoui, Slip heterogeneities in deformed aluminum bicrystals, *Acta Metallurgica* 28 (1980) 687-697. doi:10.1016/0001-6160(80)90147-9.
- [37] T. R. Bieler, R. Alizadeh, M. Peña-Ortega, J. Llorca, An analysis of (the lack of) slip transfer between near-cube oriented grains in pure Al, *International Journal of Plasticity* 118 (2019) 269-290. doi:10.1016/j.ijplas.2019.02.014.
- [38] R. Alizadeh, M. Peña-Ortega, T. R. Bieler, J. Llorca, A criterion for slip transfer at grain boundaries in Al, *Scripta Materialia* 178 (2020) 408–412. doi:10.1016/j.scriptamat.2019.12.010.
- [39] Y. Guo, T. B. Britton, A. J. Wilkinson, Slip band-grain boundary interactions in commercial-purity titanium, *Acta Materialia* 76 (2014) 1–12. doi:10.1016/j.actamat.2014.05.015.
- [40] L. Wang, Y. Yang, P. Eisenlohr, T. R. Bieler, M. A. Crimp, D. E. Mason, Twin nucleation by slip transfer across grain boundaries in commercial purity titanium, *Metallurgica and Materials Transactions A* 41 (2010) 421-430. doi:10.1007/s11661-009-0097-6.
- [41] J. R. Seal, M. A. Crimp, T. R. Bieler, C. J. Boehlert, Analysis of slip transfer and deformation behavior across the  $\alpha/\beta$  interface in Ti-5Al-2.5Sn (wt.%) with an equiaxed microstructure, *Material Science and Engineering A* 552 (2012) 61-68. doi:10.1016/j.msea.2012.04.114.
- [42] T. R. Bieler, S. C. Sutton, B. E. Dunlap, Z. A. Keith, P. Eisenlohr, M. A. Crimp, B. L. Boyce, *The Journal of The Minerals, Metals & Materials Society* 66 (2014) 121-128. doi:10.1007/s11837-013-0821-y.
- [43] Y. Yang, L. Wang, C. Zambaldi, P. Eisenlohr, R. Barabash, W. Liu, M. R. Stoudt, M. A. Crimp, T. R. Bieler, Characterization and modeling of heterogeneous deformation in commercial purity titanium, *JOM* 63 (2011) 66–73. doi:10.1007/s11837-011-0161-8.
- [44] Y. Yang, L. Wang, T. R. Bieler, P. Eisenlohr, M. A. Crimp, Quantitative atomic force microscopy characterization and crystal plasticity finite element modeling of heterogenous deformation in commercial purity titanium, *Metallurgica and Materials Transactions A* 42A (2011) 636-644. doi:10.1007/s11661-010-0475-0.
- [45] B. A. Simkin, M. A. Crimp, T. R. Bieler, A factor to predict microcrack nucleation at  $\gamma$ - $\gamma$  grain boundaries in TiAl, *Scripta Materialia* 49 (2003) 149–154. doi:10.1016/S1359-6462(03)00216-1.
- [46] B. A. Simkin, B. C. Ng, T. R. Bieler, M. A. Crimp, D. E. Mason, Orientation determination and defect analysis in the near-cubic intermetallic  $\gamma$ -TiAl using SACP, ECCI, and EBSD, *11* (2003) 215-223. doi:10.1016/S0966-9795(02)00236-4.

- [47] B. C. Ng, B. A. Simkin, M. A. Crimp, T. R. Bieler, The role of mechanical twinning on microcrack nucleation and crack propagation in a near- $\gamma$  TiAl alloy, *Intermetallics* 12 (2004) 1317-1323. doi:10.1016/j.intermet.2004.03.015.
- [48] T. R. Bieler, A. Fallahi, B. C. Ng, D. Kumar, M. A. Crimp, B. A. Simkin, Fracture initiation/propagation parameters for duplex TiAl grain boundaries based on twinning, slip, crystal orientation, and boundary misorientation, *Intermetallics* 13 (2005) 979-984. doi:10.1016/j.intermet.2004.12.013.
- [49] D. Kumar, T. R. Bieler, P. Eisenlohr, D. E. Mason, M. A. Crimp, F. Roters, D. Raabe, On predicting nucleation of microcracks due to slip-twin interactions at grain boundaries in duplex near  $\gamma$ -TiAl, *Journal of Engineering Materials and Technology* 130 (2008) 021012-1-021012-12. doi:10.1115/1.2841620.
- [50] L. Wang, P. Eisenlohr, Y. Yang, T. R. Bieler, M. A. Crimp, Nucleation of paired twins at grain boundaries in titanium, *Scripta Materialia* 63 (2010) 827-830. doi:10.1016/j.scriptamat.2010.06.027.
- [51] J. Kacher, I. M. Robertson, Quasi-four-dimensional analysis of dislocation interactions with grain boundaries in 304 stainless steel, *Acta Materialia* 60 (2012) 6657–6672. doi:10.1016/j.actamat.2012.08.036.
- [52] J. Kacher, G. S. Liu, I. M. Robertson, Visualization of grain boundary/dislocation interactions using tomographic reconstructions, *Scripta Materialia* 64 (2011) 677-680. doi:10.1016/j.scriptamat.2010.12.020.
- [53] J. Kacher, G. S. Liu, I. M. Robertson, In situ and tomographic observation of defect free channel formation in ion irradiated stainless steels, *Miron* 43 (2012) 1099-1107, doi:10.1016/j.micron.2012.01.017.
- [54] G. S. Liu, S. D. House, J. Kacher, M. Tanaka, K. Higashida, I. M. Robertson, Electron tomography of dislocation structures, *Materials Characterization* 87 (2014) 1-11, doi:10.1016/j.matchar.2013.09.016.
- [55] J. Kacher, B. Cui, I. M. Robertson, In situ and tomographic characterization of damage and dislocation processes in irradiated metallic alloys by transmission electron microscopy, 30 (2015) 1202-1213. doi:10.1557/jmr.2015.14.
- [56] J. Kacher, I. M. Robertson, In situ and tomographic analysis of dislocation/grain boundary interactions in  $\alpha$ -titanium, *Philosophical Magazine* (2014) 1–16. doi:10.1080/14786435.2013.868942.
- [57] J. Kacher, I. M. Robertson, In situ TEM characterization of dislocation interactions in  $\alpha$ -titanium, *Philosophical Magazine* 96 (2016) 1437-1447. doi:10.1080/14786435.2016.1170222.

- [58] S. Kondo, T. Mitsuma, N. Shibata, Y. Ikuhara, Direction observation of individual dislocation interaction processes with grain boundaries, *Science Advances* 2 (2016) 1-7. doi:10.1126/sciadv.1501926.
- [59] D. Kiener, P. Hosemann, S. A. Maloy, A. M. Minor, In situ nanocompression testing of irradiated copper, *Nature Materials* 10 (2011) 608-613. doi:10.1038/nmat3055.
- [60] J. T. M. De Hosson, W. A. Soer, A. M. Minor, Z. Shan, E. A. Stach, S. A. S. Asif, O. L. Warren, In situ TEM nanoindentation and dislocation-grain boundary interactions: A tribute to David Brandon. *Journal of Materials Science*, 41 (2006) 7704–7719. doi:10.1007/s10853-006-0472-2.
- [61] S. Kondo, N. Shibata, T. Mitsuma, E. Tochigi, Y. Ikuhara, Dynamic observations of dislocation behavior in SrTiO<sub>3</sub> by in situ nanoindentation in a transmission electron microscope, *Applied Physics Letter* 100, 181906 (2012). doi:10.1063/1.4710558.
- [62] Q. Zhu, S. C. Zhao, C. Deng, X. H. An, K. X. Song, S. X. Mao, J. W. Wang, In situ atomistic observation of grain boundary migration subjected to defect interaction, *Acta Materialia* 199 (2020) 42-52. doi:10.1016/j.actamat.2020.08.021.
- [63] M. Legros, D. S. Gianola, K. J. Hemker, In situ TEM observation of fast grain-boundary motion in stressed nanocrystalline aluminum films, *Acta Materialia* 56 (2008) 3380-3393. doi:10.1016/j.actamat.2008.03.032.
- [64] F. Momprou, M. Legros, T. Radetic, U. Dahmen, D. S. Gianola, K. J. Hemker, In situ TEM observation of grain annihilation in tricrystalline aluminum films, *Acta Materialia*. 60 (2012) 2209–2218. doi:10.1016/j.actamat.2011.12.013.
- [65] D. Bufford, Y. Liu, J. Wang, H. Wang, X. Wang, In situ nanoindentation study on plasticity and work hardening in aluminium with incoherent twin boundaries, 5:4964. doi:10.1038/ncomms5864.
- [66] P. J. Imrich, C. Kirchlechner, G. Dehm, Influence of inclined twin boundaries on the deformation behavior of Cu micropillars, *Materials Science & Engineering A* 642 (2015) 65-70. doi:10.1016/j.msea.2015.06.064.
- [67] P. J. Imrich, C. Kirchlechner, C. Motz, G. Dehm, Differences in deformation behavior of bicrystalline Cu micropillars containing a twin boundary or a large-angle grain boundary, *Acta Materialia* 73 (2014) 240-250. doi:10.1016/j.actamat.2014.04.022.
- [68] N. Kheradmand, H. Vehoff, A. Barnoush, An insight into the role of the grain boundary in plastic deformation by means of a bicrystalline pillar compression test and atomistic simulation, *Acta Materialia*, 61 (2013) 7454-7465. doi:10.1016/j.actamat.2013.08.056.

- [69] S-W. Lee, S. M. Han, W. D. Nix, Uniaxial compression of fcc Au nanopillars on an MgO substrate: The effects of prestraining and annealing. *Acta Materialia*. 57 (2009) 4404–15. doi:10.1016/j.actamat.2009.06.002.
- [70] D. Kiener, C. Motz, G. Dehm, Micro-compression testing: a critical discussion of experimental constraints. *Material Science & Engineering A* 505 (2009) 79–87. doi:10.1016/j.msea.2009.01.005.
- [71] I. Tiba, T. Richeton, C. Motz, H. Vehoff, S. Berbenni, Incompatibility stresses at grain boundaries in Ni bicrystalline micropillars analyzed by an anisotropic model and slip activity, 83 (2015) 227-238. doi:10.1016/j.actamat.2014.09.033.
- [72] J. S. Weaver, N. Li, N. A. Mara, D. R. Jones, H. Cho, C. A. Bronkhorst, S. J. Fensin, G. T. Gray III, Slip transmission of high angle grain boundaries in body-centered cubic metals: Micropillar compression of pure Ta single and bi-crystals, 156 (2018) 356-368. doi:10.1016/j.actamat.2018.06.046.
- [73] A. Kunz, S. Pathak, J. R. Greer, Size effects in Al nanopillars: single crystalline vs. Bicrystalline, *Acta Materialia* 59 (2011) 4416-4424. doi:10.1016/j.actamat.2011.03.065.
- [74] N. V. Malyar, J. S. Micha, G. Dehm, C. Kirchlechner, Size effect in bi-crystalline micropillars with a penetrable high angle grain boundary, *Acta Materialia* 129 (2017) 312-320. doi:10.1016/j.actamat.2017.03.003.
- [75] N. V. Malyar, J. S. Micha, G. Dehm, C. Kirchlechner, Dislocation-twin boundary interaction in small scale Cu bi-crystals loaded in different crystallographic directions, *Acta Materialia* 129 (2017) 91-97. doi:10.1016/j.actamat.2017.02.067.
- [76] A. Schneider, C. Frick, B. Clark, P. Gruber, E. Arzt, Influence of orientation on the size effect in bcc pillars with different critical temperatures, *Material Science & Engineering* 528 (2011) 1540-1547.
- [77] R. Ding, J. Gong, A. J. Wilkinson, I. P. Jones, A study of dislocation transmission through a grain boundary in hcp Ti-6Al using micro-cantilevers, *Acta Materialia* 103 (2016) 416-423. doi:10.1016/j.actamat.2015.10.023.
- [78] T. Ohmura, A. M. Minor, E. A. Stach, J. W. Morris Jr., Dislocation-grain boundary interactions in martensitic steel observed through in situ nanoindentation in a TEM, *Journal of Materials Research* 19 (2004) 3626–3632. doi:10.1557/JMR.2004.0474.
- [79] X. Chen, T. Richeton, C. Motz, S. Berbenni, Atomic force microscopy study of discrete dislocation pile-ups at grain boundaries in bi-crystalline micro-pillars, *Crystals* 2020 10 411. doi:10.3390/cryst10050411.

- [80] J. Gong, A. J. Wilkinson, A microcantilever investigation of size effect, solid solution strengthening and second-phase strengthening for  $\langle a \rangle$  prism slip in  $\alpha$ -Ti, *Acta Materialia* 59 (2011) 5970–5981. doi:10.1016/j.actamat.2011.06.005.
- [81] J. Kwon, M. C. Brandes, P. S. Phani, A. P. Pilchak, Y. F. Gao, E. P. George, G. M. Pharr, M. J. Mills, Characterization of deformation anisotropies in an  $\alpha$ -Ti alloy by nanoindentation and electron microscopy, 61 (2013) 4743–4756. doi:10.1016/j.actamat.2013.05.005.
- [82] Y. Guo, D. M. Collins, E. Tarleton, F. Hofmann, J. Tischler, W. Liu, R. Xu, A. J. Wilkinson, T. B. Britton, Measurement of stress fields near a grain boundary: exploring blocked arrays of dislocations in 3D, *Acta Materialia* 96 (2015) 229–236. doi:10.1016/j.actamat.2015.05.041.
- [83] T. B. Britton, A. J. Wilkinson, Stress fields and geometrically necessary dislocation density distributions near the head of blocked slip band, *Acta Materialia* 60 (2012) 5773–5782. doi:10.1016/j.actamat.2012.07.004.
- [84] Y. Guo, T. B. Britton, A. J. Wilkinson, Slip band-grain boundary interactions in commercial purity titanium, *Acta Materialia* 76 (2014) 1–12. doi:10.1016/j.actamat.2014.05.015.
- [85] W. Z. Abuzaid, M. D. Sangid, J. D. Carroll, H. Sehitoglu, J. Lambros, Slip transfer and plastic strain accumulation across grain boundaries in Hastelloy X, *Journal of Mechanics and Physics of Solids* 60 (2012) 1201–1220. doi:10.1016/j.jmps.2012.02.001.
- [86] L. Patriarca, W. Abuzaid, H. Sehitoglu, H. J. Maier, Slip transmission in bcc FeCr polycrystal, *Materials Science & Engineering A* 588 (2013) 308–317. doi:10.1016/j.msea.2013.08.050.
- [87] M. D. McMurtrey, G. S. Was, B. Cui, I. Robertson, L. Smith, D. Farkas, Strain localization at dislocation channel-grain boundary interactions in irradiated stainless steel, *International Journal of Plasticity* 56 (2014) 219–231. doi:10.1016/j.ijplas.2014.01.001.
- [88] Z. Kou, Y. Yang, L. Yang, W. Zhang, B. Huang, X. Luo, Deformation twinning in response to cracking in Al: an in situ TEM and molecular dynamics study, *Scripta Materialia* 145 (2018) 28–32. doi:10.1016/j.scriptamat.2017.10.013.
- [89] D. E. Spearot, K. I. Jacob, D. L. McDowell, Dislocation nucleation from bicrystal interfaces with dissociated structure, *International Journal of Plasticity* 23 (2007) 143–160. doi:10.1016/j.ijplas.2006.03.008.
- [90] D. E. Spearot, K. I. Jacob, D. L. McDowell, Nucleation of dislocations from [001] bicrystal interfaces in aluminum, *Acta Materialia* 53 (2005) 3579–3589. doi:10.1016/j.actamat.2005.04.012.

- [91] D. E. Spearot, M. A. Tschopp, K. I. Jacob, D. L. McDowell, Tensile strength of <100> and <110> tilt bicrystal copper interfaces, *Acta Materialia* 55 (2007) 705–714. doi:10.1016/j.actamat.2006.08.060.
- [92] D. E. Spearot, M. D. Sangid, Insights on slip transmission at grain boundaries from atomistic simulations, *Current Opinion in Solid State and Materials Science*, 18 (2014) 188-195. doi:10.1016/j.cossms.2014.04.001.
- [93] S. P. Coleman, D. E. Spearot, Atomistic simulation and virtual diffraction characterization of homophase and heterophase alumina interfaces, *Acta Materialia* 82 (2015) 403–413. doi:10.1016/j.actamat.2014.09.019.
- [94] V. Van, K. Li, J. Zhu, T. Yip, S. Suresh, Quantifying the early stages of plasticity through nanoscale experiments and simulations. *Physical Review B* 104105. doi:10.1103/PhysRevB.67.104105.
- [95] R. Agrawal, B. Peng, H. D. Espinosa, Experimental-computational investigation of ZnO nanowires strength and fracture, *Nano Letters* 9 (2009) 4177–4183. doi:10.1021/nl9023885.
- [96] T. Tsuru, Y. Shibutani, T. Hirouchi, A predictive model for transferability of plastic deformation through grain boundaries, *AIP advances* 6, 015004 (2016). doi:10.1063/1.4939819.
- [97] S. Chandra, N. Kumar, M. Samal, V. Chavan, R. Patel, Interaction of run-in edge dislocations with twist grain boundaries in Al-a molecular dynamics study, *Philosophical Magazine* 96 (2016) 1809-1831. doi:10.1080/14786435.2016.1178860.
- [98] B. Liu, D. Raabe, P. Eisenlohr, F. Roters, A. Arsenlis, G. Hommes, Dislocation interactions and low-angle grain boundary strengthening, *Acta Materialia* 59 (2011) 7125-7134. doi:10.1016/j.actamat.2011.07.067.
- [99] B. Liu, P. Eisenlohr, F. Roters, D. Raabe, Simulation of dislocation penetration through a general low-angle grain boundary, *Acta Materialia* 60 (2012) 5380-5390. doi:10.1016/j.actamat.2012.05.002.
- [100] W. A. Soer, J. Th. M. De Hosson, A. M. Minor, J. W. Morris Jr., E. A. Stach, Effects of solute Mg on grain boundary and dislocation dynamics during nanoindentation of Al-Mg thin films, *Acta Materialia* 52 (2004) 5783-5790. doi:10.1016/j.actamat.2004.08.032.
- [101] A. Hasnaoui, P. M. Derlet, H. V. Swygenhoven, Interaction between dislocations and grain boundaries under an indenter – a molecular dynamics simulation, *Acta Materialia* 52 (2004) 2251-2258. doi:10.1016/j.actamat.2004.01.018.
- [102] K. J. Kim, J. H. Yoon, M. H. Cho, H. Jang, Molecular dynamics simulation of dislocation behavior during nanoindentation on a bicrystal with a  $\Sigma=5$  (210) grain boundary, *Acta Materialia* 60 (2006) 3367-3372. doi: 10.1016/j.matlet.2006.03.020.

- [103] Z. Li, C. Hou, M. Huang, C. Ouyang, Strengthening mechanism in micro-polycrystals with penetrable grain boundaries by discrete dislocation dynamics simulation and Hall-Petch effect, *Computational Materials Science* 46 (2009) 1124-1134. doi:10.1016/j.commatsci.2009.05.021.
- [104] S. Lu, B. Zhang, X. Li, J. Zhao, M. Zaiser, H. Fan, X. Zhang, Grain boundary effect on nanoindentation: A multiscale discrete dislocation dynamics model, *Journal of the Mechanics and Physics of Solids* 126 (2019) 117-135. doi:10.1016/j.jmps.2019.02.003.
- [105] X. Zhang, S. Lu, B. Zhang, X. Tian, Q. Kan, G. Kang, Dislocation-grain boundary interaction-based discrete dynamics modeling and its application to bicrystals with different misorientations, 202 (2021) 88-98. doi:10.1016/j.actamat.2020.10.052.
- [106] A. Yonezu, Y. Kuwahara, K. Yoneda, H. Hirakata, K. Minoshima, Estimation of the anisotropic plastic property using single spherical indentation – An FEM study, *Computational Materials Science* 47 (2009) 611-619. doi:10.1016/j.commatsci.2009.10.003.
- [107] N. Zaafarani, D. Raabe, R. N. Singh, F. Roters, S. Zaefferer, Three dimensional investigation of the texture and microstructure below a nanoindent in a Cu single crystal using 3D EBSD and crystal plasticity finite element simulations, *Acta Materialia* 54 (2006) 1863-1876. doi:10.1016/j.actamat.2005.12.014.
- [108] E. Bayerschen, A. T. McBride, B. D. Reddy, T. Böhlke, Review on slip transmission criteria in experiments and crystal plasticity models, *Journal of Materials Science* 51 (2016) 2243-2258. doi:10.1007/s10853-015-9553-4.
- [109] C. Zambaldi, F. Roters, D. Raabe, U. Glatzel, Modeling and experiments on the indentation deformation and recrystallization of a single crystal nickel-base superalloy, *Materials Science and Engineering: A* 454-455 (2007) 433-440. doi:10.1016/j.msea.2006.11.068.
- [110] J. R. Mayeur, I. J. Beyerlein, C. A. Bronkhorst, H. M. Mourad, Incorporating interface affected zones into crystal plasticity, *International Journal of Plasticity* 65 (2015) 206-225. doi:10.1016/j.ijplas.2014.08.013.
- [111] I. Özdemir, T. Yalçinkaya, Modeling of dislocation-grain boundary interactions in a strain gradient crystal plasticity framework, *Computational Mechanics* 54 (2014) 255-268. doi:10.1007/s00466-014-0982-8.
- [112] D. M. Bond, M. A. Zikry, A predictive framework for dislocation density pile-ups in crystalline systems with coincident site lattice and random grain boundaries, *Journal of Engineering Materials and Technology* 2017, 139(2):021023. doi:10.1115/1.4035494.

- [113] E. P. Busso, F. T. Meisssonier, N. P. O'Dowd, Gradient-dependent deformation of two-phase single crystals, *Journal of the Mechanics and Physics of Solids* 48 (2000) 2333-2361. doi:10.1016/S0022-5096(00)00006-5.
- [114] A. Ma, F. Roters, D. Raabe, On the consideration of interactions between dislocations and grain boundaries in crystal plasticity finite element modeling – Theory, experiments, and simulations, *Acta Materialia* 54 (2006) 2181-2194. doi:10.1016/j.actamat.2006.01.004.
- [115] F. Roters, P. Eisenlohr, L. Hantcherli, D. D. Tjahjanto, T. R. Bieler, D. Raabe, Overview of constitutive laws, kinematics, homogenization and multiscale methods in crystal plasticity finite – element modeling: Theory, experiments, applications, *Acta Materialia* 58 (2010) 1152-1211. doi:10.1016/j.actamat.2009.10.058.
- [116] H. Lim, M. G. Lee, J. H. Kim, B. L. Adams, R. H. Wagoner, Simulation of polycrystal deformation with grain and grain boundary effects, *International Journal of Plasticity* 27 (2011) 1328-1354. doi:10.1016/j.ijplas.2011.03.001.
- [117] G. Dehm, B. N. Jaya, R. Raghavan, C. Kirchlechner, Overview on the micro- and nanomechanical testing: New insights in interface plasticity and fracture at small length scales, *Acta Materialia* 142 (2018) 248-282. doi:10.1016/j.actamat.2017.06.019.
- [118] M. D. Sangid, Coupling in situ experiments and modeling – opportunities for data fusion, machine learning, and discovery of emergent behavior, *Current Opinion in Solid State & Materials Science* 24 (2020) 100797. doi:10.1016/j.cossms.2019.100797.
- [119] J. Kacher, T. Zhu, O. Pierron, D. E. Spearot, Integrating in situ TEM experiments and atomistic simulations for defect mechanics, *Current Opinion in Solid State & Materials Science* 23 (2019) 117-128. doi:10.1016/j.cossms.2019.03.003.
- [120] C. Zhang, H. Li, P. Eisenlohr, W. Liu, C. J. Boehlert, M. A. Crimp, T. R. Bieler, Effect of realistic 3D microstructure in crystal plasticity finite element analysis of polycrystalline Ti-5Al-2.5Sn, *International Journal of Plasticity* 69 (2015) 21-35. doi:10.1016/j.ijplas.2015.01.003.
- [121] Y. Guan, B. Chen, J. Zou, T. B. Britton, J. Jiang, F. P. E. Dunne, Crystal plasticity modeling and HR-DIC measurement of slip activation and strain localization in single and oligo-crystal Ni alloys under fatigue, *International Journal of Plasticity* 88 (2017) 70-88. doi:10.1016/j.ijplas.2016.10.001.
- [122] C. C. Tasan, J. P. M. Hoefnagels, M. Diehl, D. Yan, F. Roters, D. Raabe, Strain localization and damage in dual phase steels investigated by coupled in-situ deformation experiments and crystal plasticity simulations, *Acta Materialia* 63 (2014) 198-210. doi:10.1016/j.ijplas.2014.06.004.
- [123] J. Seal, Characterization of deformation near grain boundary in polycrystalline metals, Michigan State University, PHD dissertation 2014.

- [124] S. R. Kalidindi, C. A. Bronkhorst, L. Anand, Crystallographic texture evolution in bulk deformation processing of fcc metals, *Journal of the Mechanics and Physics of Solids* 40 (1992) 537-569. doi:10.1016/0022-5096(92)80003-9.
- [125] D. Mercier, C. Zambaldi, T. R. Bieler, A matlab toolbox to analyze slip transfer through grain boundaries, *IOP Conference Series: Materials Science and Engineering* 82 012090 (2015). doi:10.1088/1757-899X/82/1/012090.
- [126] Y. Su, C. Zambaldi, D. Mercier, P. Eisenlohr, T. R. Bieler, M. A. Crimp, Quantifying deformation processes near grain boundaries in alpha-titanium using nanoindentation and crystal plasticity modeling, *International Journal of Plasticity* 86 (2016) 170–186. doi:10.1016/j.ijplas.2016.08.007.
- [127] B. Barkia, V. Doquet, J. P. Couzinie, I. Guillot, Room-temperature creep and stress relaxation in commercial purity titanium influence of the oxygen and hydrogen contents on incubation phenomena and aging-induced rejuvenation of the creep potential. *Materials Science & Engineering: A* 624 (2015) 79-89. doi:10.1016/j.msea.2014.11.073.
- [128] F. V. Ellis, C. Y. Li, Stress relaxation in titanium. *Scripta Metallurgica* 8 (1974) 739-742. doi:10.1016/0036-9748(74)90285-3.
- [129] H. Li, D. E. Mason, Y. Yang, T. R. Bieler, M. A. Crimp, C. J. Boehlert, Comparison of the deformation behaviour of commercially pure titanium and Ti-5Al-2.5Sn (wt.%) at 296 and 728 K. *Philosophical Magazine* 93 (2013) 2875-2895. doi:10.1080/14786435.2013.791752.
- [130] G. Sargent, G. Jones, H. Conrad, Work hardening during stress relaxation in titanium at 300 K. *Scripta Metallurgica*. 3 (1969) 481-484. doi:10.1016/0036-9748(69)90135-5.
- [131] R. Zeyfang, R. Martin, H. Conrad, Low temperature creep of titanium. *Materials Science & Engineering* 8 (1971) 134-140. doi:10.1016/0025-5416(71)90051-6.
- [132] G. Simmons, H. Wang, *Single Crystal Elastic Constants and Calculated Aggregate Properties: a Handbook*. M.I.T. Press 1971.
- [133] C. Zambaldi, Y. Yang, T. R. Bieler, D. Raabe, Orientation informed nanoindentation of  $\alpha$ -titanium: indentation pileup in hexagonal metals deforming by prismatic slip. *Journal of Materials Research* 27 (2012) 356-367. doi:10.1557/jmr.2011.334.
- [134] W. Z. Yao, C. E. Krill, B. Albinski, H. C. Schneider, J. H. You, Plastic material parameters and plastic anisotropy of tungsten single crystal: a spherical micro-indentation study. *Journal of Materials Science* 49 (2014) 3705-3715. doi:10.1007/s10853-014-8080-z.
- [135] C. Zambaldi, D. Raabe, Plastic anisotropy of  $\gamma$ -TiAl revealed by axisymmetric indentation, *Acta Materialia* 58 (2010) 3516-3530. doi:10.1016/j.actamat.2010.02.025.

- [136] J. Gong, A. J. Wilkinson, Anisotropy in the plastic flow properties of single-crystal  $\alpha$  titanium determined from micro-cantilever beams, *Acta Materialia* 57 (2009) 5693–5705. doi:10.1016/j.actamat.2009.07.064.
- [137] N. E. Paton, J. C. Williams, G. P. Rauscher, The deformation of alpha-phase titanium, in: R. I. Jaffee, H. M. Burte (Eds.), *Titanium Science and Technology: Proceedings of the 2nd International Conference*, Plenum, New York, 1973, pp. 1049–1058.
- [138] A. Poty, J. M. Raulot, H. Xu, J. Bai, C. Schuman, J. S. Lecomte, M. J. Philippe, C. Esling, Classification of the critical resolved shear stress in the hexagonal-close-packed materials by atomic simulation: Application to  $\alpha$ -zirconium and  $\alpha$ -titanium, *Journal of Applied Physics* 110 (2011) 014905. doi:10.1063/1.3599870.
- [139] A. A. Salem, S. R. Kalidindi, S. L. Semiatin, Strain hardening due to deformation twinning in  $\alpha$ -titanium: Constitutive relations and crystal- plasticity modeling, *Acta Materialia* 53 (2005) 3495-3502. doi:10.1016/j.actamat.2005.04.014.
- [140] I. P. Jones, W. B. Hutchinson, Stress-state dependence of slip in Titanium-6Al-4V and other H.C.P. metals, *Acta Metallurgica* 29 (1981) 951-968. doi:10.1016/0001-6160(81)90049-3.
- [141] S. Han, M. A. Crimp, ECCI analysis of shear accommodations at grain boundaries in commercially pure alpha titanium, *International Journal of Plasticity* (2020) 102731. doi:10.1016/j.ijplas.2020.102731.
- [142] F. Di Gioacchino, T. E. J. Edwards, G. N. Wells, W. J. Clegg, A new mechanism of strain transfer in polycrystals, *Scientific Reports* 10 (2020) 10082. doi:10.1038/s41598-020-66569-7.
- [143] J. C. Williams, R. G. Baggerly, N. E. Paton, Deformation behavior of HCP Ti-Al alloy single crystals, *Metallurgical and Materials Transactions A* 33 (2002) 837–850. doi:10.1007/s11661-002-0153-y.
- [144] K. S. Chan, A micromechanical analysis of the yielding behavior of individual widmanstätten colonies of an  $\alpha + \beta$  titanium alloy, *Metallurgical and Materials Transactions A* 35 (2004) 3409–3422. doi:10.1007/s11661-004-0177-6.
- [145] H. Li, D. E. Mason, T. R. Bieler, C. J. Boehlert, M. A. Crimp, Methodology for estimating the critical resolved shear stress ratios of  $\alpha$ -phase Ti using EBSD-based trace analysis, *Acta Materialia* 61 (2013) 7555–7567. doi:10.1016/j.actamat.2013.08.042.